



저작자표시-비영리-변경금지 2.0 대한민국

이용자는 아래의 조건을 따르는 경우에 한하여 자유롭게

- 이 저작물을 복제, 배포, 전송, 전시, 공연 및 방송할 수 있습니다.

다음과 같은 조건을 따라야 합니다:



저작자표시. 귀하는 원저작자를 표시하여야 합니다.



비영리. 귀하는 이 저작물을 영리 목적으로 이용할 수 없습니다.



변경금지. 귀하는 이 저작물을 개작, 변형 또는 가공할 수 없습니다.

- 귀하는, 이 저작물의 재이용이나 배포의 경우, 이 저작물에 적용된 이용허락조건을 명확하게 나타내어야 합니다.
- 저작권자로부터 별도의 허가를 받으면 이러한 조건들은 적용되지 않습니다.

저작권법에 따른 이용자의 권리는 위의 내용에 의하여 영향을 받지 않습니다.

이것은 [이용허락규약\(Legal Code\)](#)을 이해하기 쉽게 요약한 것입니다.

[Disclaimer](#)

공학박사 학위논문

**Development of GPU-based SPH Framework
for Hydrodynamic Interactions
With Non-spherical Solid Debris**

비구형 고체 파편물 및 유체간 수력학적 상호작용
해석을 위한 GPU 기반의 SPH 해석체계 개발

2021 년 8 월

서울대학교 대학원
에너지시스템공학부
최 해 운

**Development of GPU-based SPH Framework
for Hydrodynamic Interactions
With Non-spherical Solid Debris**

비구형 고체 파편물 및 유체간 수력학적 상호작용
해석을 위한 GPU 기반의 SPH 해석체계 개발

지도교수 김 응 수

이 논문을 공학박사 학위논문으로 제출함
2021 년 8 월

서울대학교 대학원
에너지시스템공학부
최 해 윤

최해윤의 박사 학위논문을 인준함
2021 년 8 월

위 원 장	<u>조 형 규</u>
부위원장	<u>김 응 수</u>
위 원	<u>김 성 중</u>
위 원	<u>방 인 철</u>
위 원	<u>이 유 호</u>

Abstract

Development of GPU-based SPH Framework for Hydrodynamic Interactions With Non-spherical Solid Debris

Hae Yoon Choi

Department of Energy System Engineering

The Graduate School

Seoul National University

Since the Fukushima accident, the necessity for researches on severe accidents and the importance of securing the ability to cope with the accidents have been increasing. The evaluation of the molten core behavior that may occur during the accident is very important in terms of re-criticality according to the coolability and integrity of the reactor core from the MCCI (Molten Core Concrete Interaction) and steam explosion. In the case of OPR 1000, especially, FCI (Fuel Coolant Interaction) is known to occur unconditionally because the wet cavity condition has been adopted as a basic strategy for ex-vessel cooling. [Jin, 2014] FCI is a highly complicated phenomenon, which includes multi-fluid, multi-phase interaction between the arbitrary shape of solid debris and coolant as well as coolant boiling. In this process, the debris bed is formed at the bottom of the containment, and its

coolability influences the next phase of the accident. For the understanding on the solid debris behavior, a solid system with a rigid body can be a good approach for the non-spherical solid debris analysis. Therefore, in this study, Smoothed Particle Hydrodynamics (SPH) method and Rigid Body Dynamics (RBD) are coupled in a fully Lagrangian manner for the hydrodynamic interactions between fluid and solid.

Smoothed Particle Hydrodynamics (SPH) is one of the Lagrangian-based analysis methods which represents the fluid flow as a finite number of particles. Since the flow is analyzed by the motion of individual particles, there is no need to calculate the nonlinear convective term, and the total mass of the system is automatically conserved as long as particles are not added or removed. Through these Lagrangian nature, it is well known that the SPH method is effective for the free surface flow, multi-fluid and multi-phase flow, and highly deformable flow. In this study, the incompressible multi-phase flow analysis has been performed using the in-house SPH code, SOPHIA code, and V&V simulation results showed good agreement with the benchmark data.

Rigid Body Dynamics (RBD) is a research field that analyses the translation and rotation of a solid body by using the concept that a rigid body doesn't change its shape by external forces. In this study, the collision calculation between rigid bodies is implemented by applying the Hertz-Mindlin contact force model commonly used and verified for a long time in the Discrete Element Method (DEM) field. A rigid body can be expressed as a group of finite particles, and the contact forces between solid bodies are calculated based on the small overlap of the particle pairs. Using the particle-based RBD analysis code implemented in this study, V&V

simulations on single- and multi- rigid body collisions have been performed and showed good agreement with the analytical solution and the benchmark data.

To analyze the hydrodynamic interactions between non-spherical solids and fluids that can occur in the nuclear field, the integrated code has been developed by coupling RBD with SPH code. Since a fully resolved approach adopted in this study as a phase coupling method satisfies the 1st principle and the fluid-solid phase is entirely separated from each other, there is no need for the surface integral and empirical correlations depending on the solid geometry. In addition, the Neumann pressure boundary condition is implemented for accurate pressure estimation at the solid interface using the fluid particle properties. By applying the resolved SPH-RBD coupled code, V&V simulations were carried out on the hydrodynamic interactions of non-spherical solid-fluid and showed good agreement with the experimental data.

In the SPH method, since the numerical expression are highly linear and the calculations are performed explicitly, there is no problem even if the calculations for each particle are performed independently. Therefore, the SPH is well known as an optimized method for parallelization, and it is essential for large scale high-resolution simulations. In addition, an efficient computational algorithm is required for particle-based rigid body calculation. In this study, therefore, the parallelization was performed using a Graphical Processing Unit (GPU) for large-scale calculations and high computational efficiency, and it showed a good performance in analyzing the interactions of a large number of solids and fluids particles.

Through the researches on the development of a GPU-based SPH framework for the hydrodynamic interaction of non-spherical solids and fluids in this study, an efficient analysis system has been developed for not only the hydrodynamic interaction of solid corium debris with coolant but also the mechanical interaction between solid debris which can occur at the severe accidents in the nuclear reactor. By using this, it is expected that the integrated code will contribute to analytical researches on various accident scenarios that may occur in the nuclear field such as solid fuel debris sedimentation in the wet cavity, hydrodynamic interactions with coastal structures caused by the Tsunami, and the behavior of floating objects in the reactor building at the flooding accident, etc.

Keywords

Smoothed Particle Hydrodynamics, Rigid Body Dynamics, Severe Accident, GPU Parallelization, Non-spherical Debris, Sedimentation

Student Number: 2013-23187

List of Contents

Abstract.....	i
Chapter 1 Introduction.....	1
1.1 Background and Motivation	1
1.2 Previous Studies	3
1.2.1 Numerical Studies on FCI Premixing Jet Breakup.....	3
1.2.2 Numerical Studies on Fluid-Solid Coupling with RBD	4
1.3 Objectives and Scope.....	5
Chapter 2 Smoothed Particle Hydrodynamics (SPH)	9
2.1 SPH Overview	9
2.1.1 Basic Concept of SPH	9
2.1.2 SPH Particle Approximation	10
2.1.3 SPH Kernel Function.....	12
2.1.4 SPH Governing Equations.....	13
2.2 SPH Multi-phase Models.....	16
2.2.1 Normalized Density Approach	16
2.2.2 Treatments for Multi-phase Flow	17
2.2.3 Surface Tension Force Model.....	18
2.3 SPH Code Implementation	20
2.3.1 Nearest Neighbor Particle Search (NNPS).....	20
2.3.2 Algorithm of SPH Code	21
2.3.3 Time Integration	21
2.3.4 GPU Parallelization	22
Chapter 3 Rigid Body Dynamics (RBD)	30
3.1 RBD Overview	30
3.2 Collision Models of Rigid Body.....	31
3.2.1 Monaghan Boundary Force (MBF) Model.....	31
3.2.2 Ideal Plastic Collision Model	33
3.2.3 Impulse-based Boundary Force (IBF) Model.....	35
3.2.4 Penalty-based Contact Model.....	37
3.2.5 Determination of Collision Model.....	40
3.3 Algorithm of RBD	41

3.3.1	Calculation of Rigid Body Information.....	41
3.3.2	Contact Detection	42
3.3.3	Contact Normal Calculation	42
3.3.4	Contact Force Calculation	45
3.3.5	Summation of Rigid Body Particles	46
3.3.6	Time Integration	47
3.4	GPU Parallelization	48
3.4.1	Algorithm 1: Atomic Operation.....	49
3.4.2	Algorithm 2: Sorting.....	50
3.5	Code V&V Simulations	51
3.5.1	Conservation of Momentum & Angular Momentum	51
3.5.2	Conservation of Kinetic Energy in Elastic Collision.....	52
3.5.3	Bouncing Block	53
3.5.4	Sliding Block on a Slope	55
3.5.5	Collapse of Stacked Multi-body	57
Chapter 4	Two-way Coupling of SPH-RBD	75
4.1	Resolved Approach.....	75
4.2	Governing Equations	75
4.2.1	Solid Phase	75
4.2.2	Fluid Phase	78
4.3	Algorithm of SPH-RBD Code.....	78
4.4	Code V&V Simulations	81
4.4.1	Karman Vortex Problem	81
4.4.2	Water Entry.....	84
4.4.3	Sinking & Rotating Body	85
4.4.4	Floating & Falling Body.....	85
4.4.5	Collapse of Stacked Multi-body with Fluid	87
4.4.6	Code Application to Non-spherical Debris Sedimentation	89
Chapter 5	Conclusion	110
5.1	Summary.....	110
5.2	Recommendations	112
	Nomenclature	114
	Bibliography	117
	국문 초록	127

List of Figures

Figure 1.1 Progression of FCI and related physical models	7
Figure 1.2 Previous studies on FCI.....	7
Figure 1.3 Previous studies on CFD-RBD coupling.....	8
Figure 1.4 Objectives and scopes of this study.....	8
Figure 2.1 Flow analysis represented by SPH particles.....	24
Figure 2.2 SPH kernel approximation	24
Figure 2.3 SPH results of density & pressure field:	26
Figure 2.4 Grid-based NNPS	26
Figure 2.5 Algorithm of SPH code	27
Figure 2.6 Simplified CUDA architecture	28
Figure 2.7 GPU parallel reduction	28
Figure 2.8 Speedup after GPU parallelization	29
Figure 3.1 Motion of rigid body	59
Figure 3.2 Grid-based contact detection	59
Figure 3.3 Particle-based contact detection	60
Figure 3.4 The concept of spring-dashpot model	60
Figure 3.5 Sticking collision in IBF model.....	61
Figure 3.6 Single particle collision (DEM)	62
Figure 3.7 Incorrect calculation in particle-based rigid body collision	62
Figure 3.8 Rigid particle type in cubic geometry	63
Figure 3.9 Velocity vector at contact point	63
Figure 3.10 Algorithm of rigid body motion	64
Figure 3.11 Memory racing condition	64
Figure 3.12 AtomicAdd operation	65
Figure 3.13 CUDA memory structure.....	65
Figure 3.14 GPU parallelization algorithms	66
Figure 3.15 Reduction process without sorting	66
Figure 3.16 Reduction process with sorting	67
Figure 3.17 Comparison among.....	68
Figure 3.18 Conservation of momentums and energy for several shapes	68
Figure 3.19 2D bouncing simulations for restitution coefficient.....	69
Figure 3.20 Height of bouncing solid with analytic solution	69

Figure 3.21 Vertical velocity of bouncing solid with analytic solution	70
Figure 3.22 Forces acting on the box.....	70
Figure 3.23 Simulation results in normal direction of the box	71
Figure 3.24 Simulation results in tangential direction of the box.....	72
Figure 3.25 Forces applied on the solid body	73
Figure 3.26 Horizontal location according to the friction coefficient	73
Figure 3.27 Horizontal location according to the slope degree	74
Figure 3.28 Snapshots of rigid body motion comparison	74
Figure 4.1 Simplified algorithm of SPH-RBD coupling code.....	94
Figure 4.2 Geometry of Karman vortex simulation.....	95
Figure 4.3 Drag coefficient versus Reynolds number (Cheng, 2013)	95
Figure 4.4 Simulation results of circular cylinder for $Re=100$	96
Figure 4.5 Strouhal number versus Reynolds number for square cylinder	97
Figure 4.6 Drag coefficient of square cylinder in low Reynolds region.....	98
Figure 4.7 Vorticity of circular and square cylinder	98
Figure 4.8 Vorticity for three cases: (a) case 1, (b) case 2, (c) case 3.....	99
Figure 4.9 Drag coefficient for three cases with $Re = 100$	100
Figure 4.10 Lift coefficient for three cases with $Re = 100$	100
Figure 4.11 Schematic of wedge entry simulation.....	101
Figure 4.12 Comparison on the vertical velocity of the wedge	101
Figure 4.13 Geometry and conditions for simulation	102
Figure 4.14 Comparison of the horizontal location of the solid	102
Figure 4.15 Comparison of the vertical location of the solid	103
Figure 4.16 Comparison of the rotation angle of the solid	103
Figure 4.17 Snapshot of floating solid simulation	104
Figure 4.18 Simulation result with experimental data for floating solid	104
Figure 4.19 Snapshot of falling solid simulation	105
Figure 4.20 Simulation result with experimental data for falling solid	105
Figure 4.21 Snapshot of the multi-rigid behaviour: left (6layers), right (12layers)	106
Figure 4.22 Comparison of arriving time with experiments.....	106
Figure 4.23 Comparison between single- and multi-phase simulations	107
Figure 4.24 Schematic of sedimentation experiment apparatus	107
Figure 4.25 Stacked geometry of solid debris	108
Figure 4.26 Comparison of non-spherical debris sedimentation	108
Figure 4.27 Snapshot of debris bed formation at the top view	109

List of Tables

Table 2.1 SPH formulations for the governing equations.....	25
Table 3.1 Comparison of collision results	61
Table 3.2 V&V simulations for solid-solid interactions	67
Table 4.1 V&V simulations for fluid-solid interactions	94
Table 4.2 Comparison of circular cylinder for $Re=100$	96
Table 4.3 Comparison of square cylinder for $Re=100$	97

Chapter 1

Introduction

1.1 Background and Motivation

In the nuclear field, there are several issues of hydrodynamic interactions between not only fluids but also fluids and solids. First, in the tsunami accident which has been mentioned as the cause of the Fukushima accident 10 years ago, the waves interact with the terrain structures near the shore or even nuclear power plants. In nuclear safety respect, evaluating the impact of the hydrodynamic forces on structures and analyzing it can play an important role in preparing for natural disasters that may occur again in the future. Next, if the In-Vessel Retention (IVR) strategy fails and the molten fuel melts through the reactor vessel lower head, the molten core materials (corium) may be released into the wet cavity, which causes a Fuel-Coolant Interaction (FCI). In the FCI process during the severe accident, many complicated phenomena occur such as the jet breakup where the molten fuel and the coolant interact with each other, the solid debris formation caused by heat transfer between the two immiscible fluids, and the sedimentation and the debris bed formation by the deposition of solid debris. At this time, if the debris bed isn't cooled down sufficiently, Molten Core Concrete Interaction (MCCI) may occur. (Figure 1.1) Therefore, the evaluation on the coolability of the debris bed is

important for reactor safety. Since there are many factors that influence the coolability such as the shape and size of the solid debris, configuration of debris bed, internal flow path, and porosity, etc., various studies are needed to evaluate the effect of these factors.

All the phenomena mentioned above involve not only the hydrodynamic interactions between non-spherical solid and fluid but also the mechanical interactions between solids. For the fluid-solid analysis, Discrete Element Method (DEM) has been advancing through a lot of analytical studies on the interaction between fluids and solids by coupling with CFD codes. The application of the DEM could be considered for such solid analysis, however, it is limited in well-known spherical or cylindrical shapes. Also, the absence of empirical correlations for the complex shapes (non-spherical) makes it difficult to apply to general situations. Although many researches on various solid shapes using the bonding models have been actively investigated recently, there is still a limitation due to the absence of correlations depending on the shape of the solid body for fluid-solid interactions.

Therefore, an analysis method that doesn't require empirical correlations is needed to analyze the interactions of general-shape solids, and the application of the Rigid Body Dynamics (RBD) can be a good alternative for this. In the particle-based RBD, the non-spherical solid can be expressed as a group of particles, and if combined with CFD, the analysis system of the fluid-solid hydrodynamic interactions could be established. In this respect, this study was motivated by the idea of coupling the particle-based rigid body dynamics with Lagrangian CFD code. For the analysis of the previously mentioned phenomena including high deformable geometry and multi-phase flow, the in-house SOPHIA code has been developed using the particle-based Smoothed Particle Hydrodynamics (SPH) method. By

coupling SPH with RBD, therefore, the integrated analysis system was developed in this study for the hydrodynamic interactions between fluid and non-spherical solid.

Also, since the phenomena to be analyzed require large scale and high resolution simulations, the integrated code should be able to handle a large amount of solid debris on large scale. Therefore, computational parallelization is needed for more realistic and accurate simulation. For this purpose, a Graphical Processing Unit (GPU) can be a good tool for computational parallelization, and it is expected that computational efficiency will increase more and more as the technologies advance every year. In this motivation, the GPU-based SPH-RBD integrated code has been developed for the improvement of computational performance in this study.

1.2 Previous Studies

1.2.1 Numerical Studies on FCI Premixing Jet Breakup

Since the FCI phenomenon contains highly complex and sharp geometries, phenomenological understanding should be prioritized. For the understanding on the FCI phenomenon and its process, the previous studies on FCI were investigated in analytical manner. (Figure 1.2) Many analytical studies have been conducted in non-boiling conditions to understand the hydraulic mechanism of FCI phenomenon and predicted fragmentation size of solid debris using Rayleigh-Taylor instability, Kelvin-Helmholtz instability, and Critical Weber number Theory (CWT). In the study of Ikeda (2001), the breakup mechanism of the flow was analyzed using the

two-phase Moving Particle Semi-implicit (MPS) method. In the research of Zhou (2017), the jet breakup phenomena were simulated using the Volume of Fluid (VOF), and the expected range of solid debris was proposed by performing solidification modeling through the viscosity change according to heat transfer. And, in the study of Park et al (2020), two-phase flow analysis was performed using the SPH method with fluid and air particles. For the very high-resolution simulation, multi-GPU parallelization was carried out and showed high computational performance. In Choi (2021)'s study, the breakup mechanism was analyzed through the instabilities (R-T, K-H) and CWT, and the simulations were also conducted under the presence of complicated structures using the SPH method. As such, many studies have been performed to understand the phenomenological understanding of FCI, but there is no research on the solid-fluid interactions which occur in the real FCI process. Therefore, an analysis system that can simulate not only fluid-fluid interactions but also fluid-solid interactions is needed to understand the hydrodynamic interaction between solid debris and coolant in a nuclear reactor.

1.2.2 Numerical Studies on Fluid-Solid Coupling with RBD

The interactions between fluids and solids are very frequent in the real world. So, many researches have been actively conducted in many engineering fields such as coastal engineering, soil engineering, and nuclear engineering, etc. For the understanding on the fluid-solid interactions, previous studies that use the rigid body dynamics coupled with CFD code were investigated. (Figure 1.3) In the study of Ren (2014), the simulations on the behavior of waves according to the shape of the breakwater near the shore were performed using OpenMP which enhances the

computational efficiency through CPU parallelization. Meanwhile, Wang (2019) conducted analytical studies on the flooding accident in a nuclear reactor building by combining the MPS method with rigid body dynamics. In the study of Hwang (2019) conducted at POSTECH, debris sedimentation simulations were carried out using the commercial CFD code coupled with DEM. Through the research, quantitative comparison with experiments such as the configuration of the debris bed was performed and showed good agreement. As such, the analytical studies on fluid-solid interactions have been actively conducted in various engineering fields, and the necessity in the nuclear field can be confirmed.

1.3 Objectives and Scope

Based on the previous studies described above, the purpose of this study is to develop the GPU-based SPH framework for the hydrodynamic interactions of non-spherical solids and fluids in the nuclear field. The detailed objectives of this study are as follows.

- (1) Development of a non-spherical solid analysis system
- (2) GPU parallelization for high-resolution calculation and computation efficiency
- (3) Integration of SPH-RBD model

In this study, the behavior of the rigid body is analyzed by representing it with a group of particles, and the solid interactions are modeled using the penalty-based

Hertz-Mindlin contact model. By using the implemented collision model, the mechanical interactions between solids have been verified and validated. Next, in order to establish an analysis system for a large number of solid and fluid particles, computational parallelization based on GPU was performed. Finally, by coupling the parallelized models with the SPH method, the integration of the fluid-solid model is the third goal. Through these detailed objectives, the final objective of this study is to establish an analysis system for the interaction of non-spherical solids with fluids in nuclear reactor accidents. (Figure 1.4)

Chapter 2 introduces the SPH method used in this study for fluid analysis and the GPU parallelization algorithm for high resolution computation. Chapter 3 introduces the rigid body models applied to this study for non-spherical solid-solid interaction, and deals with the GPU parallelization algorithm for solid particles and the V&V simulation results. Chapter 4 treats the SPH-RBD coupling algorithm and results. Chapter 5 summarized and concludes this study.

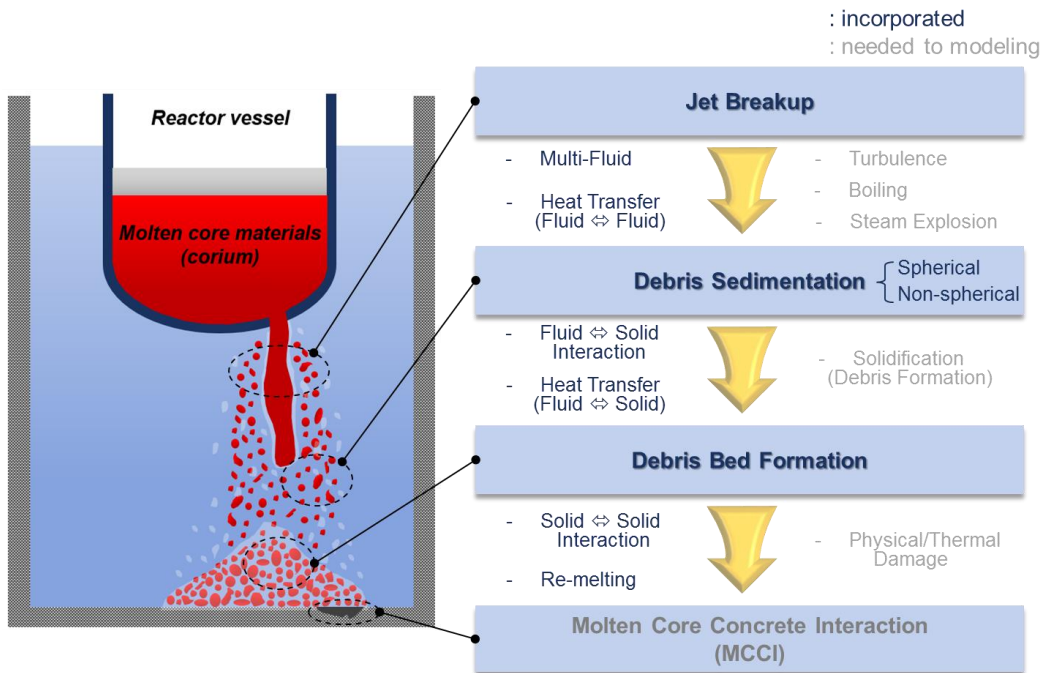


Figure 1.1 Progression of FCI and related physical models

Phenomenon	Method	Phase	Note	
Ikeda (2001)	FCI premixing	MPS (Lagrangian)	2-phase	<ul style="list-style-type: none"> ▪ Studies on breakup mechanism ▪ Using fluid-air particles (2-phase)
Thakre (2015)	FCI premixing	VOF (Eulerian)	1-phase	<ul style="list-style-type: none"> ▪ Studies on breakup mechanism ▪ Droplet size distribution based on theories
Park (2016)	FCI premixing	MPS (Lagrangian)	2-phase	<ul style="list-style-type: none"> ▪ Using fluid-air particles (2-phase) ▪ Penetration depth comparison
Zhou (2017)	FCI premixing	VOF (Eulerian)	1-phase	<ul style="list-style-type: none"> ▪ Solidification modeling using viscosity model ▪ No solid analysis
Li (2019)	Melt drop	MPS (Lagrangian)	1-phase	<ul style="list-style-type: none"> ▪ Fragmentation trend depending on properties
Park (2020)	FCI premixing	SPH (Lagrangian)	2-phase	<ul style="list-style-type: none"> ▪ Using fluid-air particles (2-phase) ▪ Multi-GPU for high-resolution
Choi (2021)	FCI premixing	SPH (Lagrangian)	1-phase	<ul style="list-style-type: none"> ▪ Studies on breakup mechanism ▪ Simulations on complicated geometries in BWR

Figure 1.2 Previous studies on FCI

Author	Field	Analysis Method	Collision Model	Interaction b/w Solids	# of Solids	Parallelization
Monaghan (2003) [26]	Coastal Eng.	SPH (2D)	MBF	X	1	-
Ren (2014) [4]	Coastal Eng.	SPH (2D)	Spring-dashpot	O	~100	OpenMP (CPU-parallelized)
Mao (2020) [5]	Soil Eng.	VOF (2D)	DEM	O	-	-
Zhan(2020) [6]	Soil Eng.	SPH (3D)	IPM	O	<10	Single-GPU
Qiu (2017) [30]	Mathematics	SPH (3D)	Spring-dashpot	O	1	-
Joubert (2020) [7]	Mathematics	SPH (3D)	X	X	<10	Blaze-DEM (Multi-GPU)
Hwang (2019) [8]	Nuclear Eng.	CFD (3D)	DEM	O	Max. 700,000	-
Wang (2019) [9]	Nuclear Eng.	EMPS (3D)	Spring-dashpot	O	<5	-

Figure 1.3 Previous studies on CFD-RBD coupling

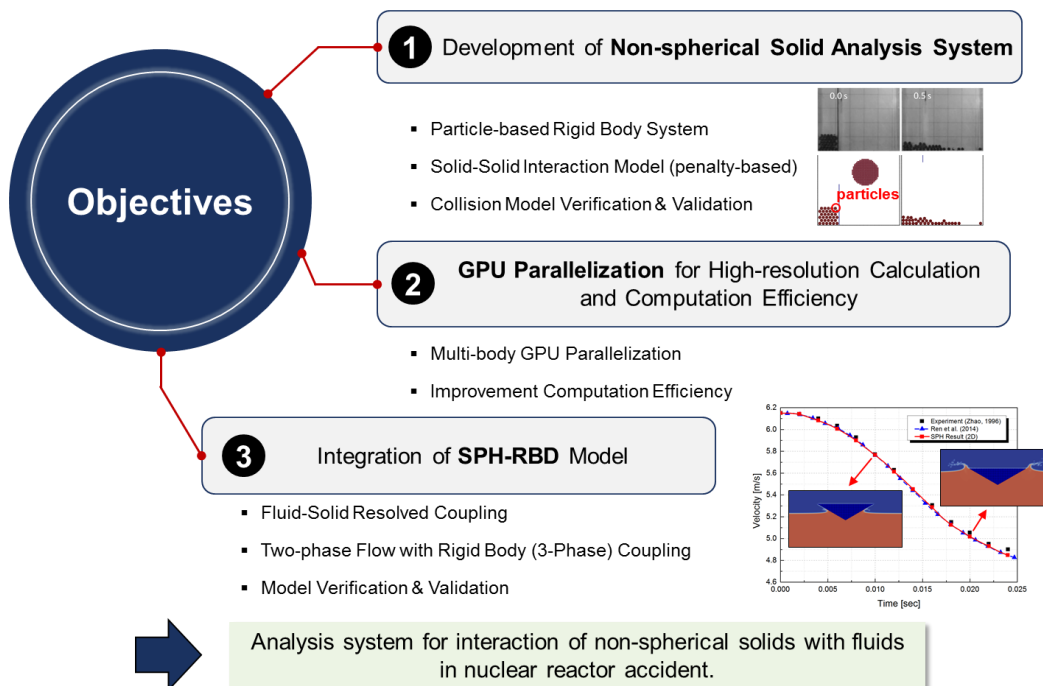


Figure 1.4 Objectives and scopes of this study

Chapter 2

Smoothed Particle Hydrodynamics (SPH)

2.1 SPH Overview

In this study, the fluid system has been analyzed using the smoothed particle hydrodynamics (SPH) method, which is one of the well-known Lagrangian CFD analyses. This section deals with the SPH methodology, the implemented code algorithm, and GPU parallelization.

2.1.1 Basic Concept of SPH

The SPH method is one of the Lagrangian analysis methods originally developed in the astronomy field [Gingold, 1977] and has been widely applied in engineering fields such as mechanical engineering, chemical engineering, ocean engineering, and nuclear engineering. The SPH method performs flow analysis by representing the geometry of flow with finite particles as shown in Figure 2.1. Each particle has individual properties, and the SPH calculation is performed by a weighted average of the surrounding particle properties within a support domain. And there is no need to use a correlation because the SPH method calculated the flow based on the first principle. Due to the nature of the Lagrangian analysis, where

the flow is analyzed by the direct motion of the particles, mass conservation is naturally satisfied, and the convective term is automatically calculated without calculating the non-linear terms. With these characteristics, the SPH method is effective for the analysis of free surface flow, multi-fluid flow, multi-phase flow, and highly deformable geometry flow.

2.1.2 SPH Particle Approximation

For the SPH calculation, it is necessary to calculate each particle's property through the particle approximation, and a kernel function which is a weight function is introduced. The properties of the interesting particle are calculated by a weighted average of the neighboring particles within the kernel radius. Then, individual particles directly move based on the governing equations.

A continuous field function is expressed using the kernel function, which approximated the delta function.

$$f(x) = \int_{\Omega} f(x')W(x - x', h)dx' \quad (2.1)$$

$f(x)$ denotes a field function at position x in the support domain Ω , and $W(x - x', h)$ is a kernel function with a weight value, where h is the kernel radius that participates in the calculation of x . Equation (2.1) can be expressed as the sum of the finite mass points, and it is discretized by the SPH particle approximation as follows.

$$f(r_i) = \sum_j \frac{m_j}{\rho_j} f_j W_{ij} \quad (2.2)$$

$f(r_i)$ is the value of a field function at particle i , and subscript j denotes the neighboring particles within the kernel radius. m and ρ are the mass and density of the particles, respectively. Figure 2.2 shows the kernel function and the calculated domain around the interesting particle i .

The SPH discretization for f is imply expressed using a kernel function as above. Similarly, the first derivative of the filed function can be expressed as a function of kernel derivative for all particles in the support domain of particle i . [Liu, 2003]

$$\nabla f(r_i) = \sum_j \frac{m_j}{\rho_j} f_j \nabla W_{ij} \quad (2.3)$$

The second derivative, which is the Laplacian, can be similarly expressed to the previous one using the Laplacian of kernel function. However, Brookshaw (1985), Schwaigher (2008) suggested the other form for numerical stability.

$$\nabla^2 f(r_i) = \sum_j \frac{2m_j}{\rho_j} [f_j - f_i] \frac{\mathbf{r}_{ij} \cdot \nabla W_{ij}}{r_{ij}^2} \quad (2.4)$$

where ∇W_{ij} is the derivative of the kernel function, and \mathbf{r}_{ij} is the relative position vector between particle i and neighbor particle j .

2.1.3 SPH Kernel Function

The kernel function is an approximated form of the Dirac delta function. Therefore, the following properties of the delta function should be satisfied in the kernel function.

- ◆ Unity condition: $\int_{\Omega} W(r, h) d\Omega = 1$
- ◆ Symmetry condition: $W(r, h) = W(-r, h)$
- ◆ Compact support condition: $W(r, h) = 0$ for $|r| > \kappa h$
- ◆ Positive condition: $W(r, h) \geq 0$ for any r
- ◆ Delta-function approximation: $\lim_{h \rightarrow 0} W(r, h) = \delta(r)$
- ◆ Monotonic decrease condition: $W'(r, h) < 0$
- ◆ Sufficiently smooth condition:

There are many kernel functions, and representative kernel functions applied in this study are as follows.

- ◆ Gaussian kernel function

$$W(R, h) = \begin{cases} \frac{1}{(\pi^{0.5}h)} e^{-R^2} & \text{for } 1D \\ \frac{1}{(\pi^{0.5}h)^2} e^{-R^2} & \text{for } 2D \\ \frac{1}{(\pi^{0.5}h)^3} e^{-R^2} & \text{for } 3D \end{cases}$$

- ◆ Quartic kernel function

$$W(R, h) = \begin{cases} \frac{1}{h} \left(\frac{2}{3} - \frac{9}{8}R^2 + \frac{19}{24}R^3 - \frac{5}{32}R^4 \right) & \text{for 1D} \\ \frac{15}{7\pi h^2} \left(\frac{2}{3} - \frac{9}{8}R^2 + \frac{19}{24}R^3 - \frac{5}{32}R^4 \right) & \text{for 2D} \\ \frac{315}{208\pi h^3} \left(\frac{2}{3} - \frac{9}{8}R^2 + \frac{19}{24}R^3 - \frac{5}{32}R^4 \right) & \text{for 3D} \end{cases}$$

- ◆ Wendland C2 kernel function

$$W(R, h) = \begin{cases} \frac{5}{4(2h)} (1 - R)^3 (1 + 3R) & \text{for 1D} \\ \frac{7}{\pi(2h)^2} (1 - R)^4 (1 + 4R) & \text{for 2D} \\ \frac{21}{2\pi(2h)^3} (1 - R)^4 (1 + 4R) & \text{for 3D} \end{cases}$$

2.1.4 SPH Governing Equations

Similar to Eulerian method, the basic governing equations for Lagrangian scheme in the SPH method are based on the fundamental conservation laws of physics: mass conservation, momentum conservation, and energy conservation.

$$\frac{d\rho}{dt} = -\rho \nabla \cdot \mathbf{u} \quad (2.5)$$

$$\frac{d\mathbf{u}}{dt} = -\frac{1}{\rho} \nabla P + \frac{\mu}{\rho} \nabla^2 \mathbf{u} + \mathbf{g} \quad (2.6)$$

$$\frac{dh}{dt} = -\frac{k}{\rho} \nabla^2 T + \dot{q} \quad (2.7)$$

ρ and \mathbf{u} is the density and velocity of the fluid. $P, \mu,$ and \mathbf{g} is the pressure, dynamic viscosity, and gravitational acceleration, respectively; $h, k, T,$ and \dot{q} denotes specific enthalpy, thermal conductivity, temperature, and heat generation rate, respectively.

In the mass conservation in the SPH method, the total mass of the system is perfectly conserved owing to the nature of the Lagrangian scheme. There are two approaches in mass conservation, which one is the direct mass summation approach and the second one is the continuity equation.

$$(\rho)_i = \sum_j m_j W_{ij} \quad (2.8)$$

$$\left(\frac{d\rho}{dt}\right)_i = -\rho_i \sum_j \frac{m_j}{\rho_j} (\mathbf{u}_i - \mathbf{u}_j) \cdot \nabla_i W_{ij} \quad (2.9)$$

For the momentum conservation, the pressure force term which is the first term of RHS of Equation (2.6) can be discretized as SPH form.

$$\left(-\frac{1}{\rho} \nabla P\right)_i = -\sum_j m_j \left(\frac{p_i}{\rho_i^2} + \frac{p_j}{\rho_j^2}\right) \nabla_i W_{ij} \quad (2.10)$$

where P_i, P_j mean the pressure of particle i and j .

Also, the laminar viscous force of 2nd term of RHS of Equation (2.6) can be expressed using the harmonic average and approximation by Boorkshaw (1985) and Schwaiger (2008).

$$\left(\frac{\mu}{\rho}\nabla^2\mathbf{u}\right)_i = \sum_j \frac{2m_j}{\rho_i\rho_j}\mu_{ij}\frac{\mathbf{r}_{ij}\cdot\nabla W_{ij}}{|\mathbf{r}_{ij}|^2}(\mathbf{u}_i - \mathbf{u}_j) \quad (2.11)$$

where μ denotes the viscosity of the particle, and \mathbf{r}_{ij} means the position vector of particle i and j .

As mentioned earlier, the convective term in the Lagrangian framework is automatically solved by the direct motion of particles. For energy conservation, therefore, the conduction equation is applied based on the enthalpy of particles.

$$\left(\frac{dh}{dt}\right)_i = \sum_j \frac{4m_j}{\rho_i\rho_j}k_{ij}\frac{\mathbf{r}_{ij}\cdot\nabla W_{ij}}{|\mathbf{r}_{ij}|^2}(T_i - T_j) \quad (2.12)$$

where T_i, T_j mean the temperature of particle i and j .

The SPH code used in this study is based on the standard weakly compressible SPH (WCSPH) which allows slight compressibility of the fluid particles and estimates the pressure of the fluid by calculating a slight density change. [Monaghan, 1994] For the pressure calculation, the Tait equation is applied as the equation of state (EOS).

$$P_i = \frac{c_0^2\rho_{ref,i}}{\gamma} \left[\left(\frac{\rho_i}{\rho_{ref,i}}\right)^\gamma - 1 \right] \quad (2.13)$$

c_0 , $\rho_{ref,i}$ and γ denote sound of speed, reference density and EOS stiffness parameter, respectively. γ is recommended as 1 – 7 and set as 7 in this study. Equation (2.13) calculates the pressure based on the density ratio between the particle density(ρ_i) and the reference density($\rho_{ref,i}$), which allows a slight volume compression for liquid fluids. However, a numerical instability (stiff problem) can be caused by the enormous pressure calculation even with very small density changes. In order to resolve this problem, it is needed to adjust the sound speed properly. In general, the value of sound speed is set as $c_0 \sim 0.1u_{max}$ assuming compressibility of 1%. Table 2.1 shows the conventional SPH expression of the governing equations.

2.2 SPH Multi-phase Models

2.2.1 Normalized Density Approach

For a single-phase (fluid) analysis, the total mass of the system is completely conserved. However, when analyzing two different fluids a non-physical density averaging occurs at the interface of the fluids in the conventional SPH method. This non-physical calculation induces the pressure oscillation and instability of the system. To resolve this in the multi-phase (fluid) system, the normalized density approach is applied in the SOPHIA code, the SPH code used in this study using the reference density. [Jo, 2019] As the name suggests, the normalized density approach performs the density estimation by substituting ‘a normalized density’ with continuous value at the interface instead of the basic density term. This approach

can be applied to both cases of mass conservation (direct mass summation, continuity equation), then Equation (2.8) and (2.9) can be converted into the following forms.

$$\left(\frac{\rho}{\rho_{ref}}\right)_i = \sum_j \left(\frac{\rho}{\rho_{ref}}\right)_j \frac{m_j}{\rho_j} W_{ij} \quad (2.14)$$

$$\frac{d}{dt} \left(\frac{\rho}{\rho_{ref}}\right)_i = - \left(\frac{\rho}{\rho_{ref}}\right)_i \sum_j \frac{m_j}{\rho_j} (\mathbf{u}_i - \mathbf{u}_j) \cdot \nabla W_{ij} \quad (2.15)$$

where ρ_{ref} means the constant initial density of the particle. By applying the normalized density approach, the non-physical density estimation and pressure oscillation at the interface can be prevented as shown in Figure 2.3.

2.2.2 Treatments for Multi-phase Flow

In the conventional SPH method, the pressure gradient term and viscous term in momentum conservation are expressed as Equation (2.10) and (2.11). However, these forms can induce inaccurate results in the large density ratio analysis such as the multi-phase or multi-fluid flows. Therefore, the following volume-based expression of the pressure force term is applied for the multi-phase system.

$$\left(-\frac{1}{\rho} \nabla P\right)_i = -\frac{1}{m_i} \sum_j (V_i^2 + V_j^2) \frac{\rho_j P_i + \rho_i P_j}{\rho_i + \rho_j} \nabla W_{ij} \quad (2.16)$$

V_i and V_j mean the volume of particle i and j . In addition, the laminar viscous force term in Equation (2.11) and heat transfer term in Equation (2.12) can accurately perform the calculation at the physical interface by applying the harmonic average of the physical properties as follows.

$$\left(\frac{\mu}{\rho} \nabla^2 \mathbf{u}\right)_i = \sum_j \frac{2m_j}{\rho_i \rho_j} \frac{2\mu_i \mu_j}{\mu_i + \mu_j} \frac{\mathbf{r}_{ij} \cdot \nabla W_{ij}}{|\mathbf{r}_{ij}|^2} (\mathbf{u}_i - \mathbf{u}_j) \quad (2.17)$$

$$\left(\frac{dH}{dt}\right)_i = \sum_j \frac{2m_j}{\rho_i \rho_j} \frac{2k_i k_j}{k_i + k_j} \frac{\mathbf{r}_{ij} \cdot \nabla W_{ij}}{|\mathbf{r}_{ij}|^2} (T_i - T_j) \quad (2.18)$$

2.2.3 Surface Tension Force Model

At small scale simulations of multi-phase (fluid) flow, the effect of surface tension force can be large locally. Especially, the capillary instability can be dominant in small scale (mm-scale), and the Continuum Surface Force (CSF) model is applied to treat multi-phase interface. [Richards, 1995] [Adami, 2010]

$$\left(\frac{d\mathbf{u}}{dt}\right)_i^{CSF} = -\frac{\sigma_i}{\rho_i} \kappa_i \mathbf{n}_i \quad (2.19)$$

$$\mathbf{n}_i = (\nabla c)_i = \frac{1}{V_i} \sum_j (V_i^2 + V_j^2) c_{ij} \nabla W_{ij} \quad (2.20)$$

$$\text{where } c_{ij} = \begin{cases} 0 & \text{for } f_i = f_j \\ \frac{\rho_i}{\rho_i + \rho_j} & \text{for } f_i \neq f_j \end{cases}$$

$$\kappa_i = -\nabla \cdot \hat{\mathbf{n}}_i = -\text{dim} \frac{\sum_j V_j (\hat{\mathbf{n}}_i - \varphi_{ij} \hat{\mathbf{n}}_j) \nabla W_{ij}}{\sum_j V_j |\mathbf{r}_{ij}| |\nabla W_{ij}|} \quad (2.21)$$

$$\text{where } \varphi_{ij} = \begin{cases} 1 & \text{for } f_i = f_j \\ -1 & \text{for } f_i \neq f_j \end{cases}$$

where σ, κ, c , and \mathbf{n}_i are the surface tension coefficient, curvature, color field, and normal vector at the interface; dim and $\hat{\mathbf{n}}_i$ are the analysis dimension and a unit normal vector at the interface.

When the surface tension force is minor compared to other forces, non-physical fragmentation of the particle among different fluids can occur. Therefore, the interface sharpness force which is a type of repulsive force is applied to prevent non-physical fragmentation.

$$\left(\frac{d\mathbf{u}}{dt} \right)_i^{ISF} = -\frac{\varepsilon}{\rho_i V_i} \sum_j (|P_i| V_i^2 + |P_j| V_j^2) \nabla W_{ij} \quad (2.22)$$

where ε is a constant value of $0.01 - 0.1$; In this study, 0.08 is used to minimize the non-physical fragmentation without affecting the analysis results. [Granier, 2009] [Zhang, 2015]

2.3 SPH Code Implementation

2.3.1 Nearest Neighbor Particle Search (NNPS)

In general, neighbor particle searching (NNPS) is the most time-consuming process in the SPH calculation. To estimate the properties of the interesting particle i , it is necessary to search for neighboring particles within the kernel radius which is set as three times of initial particle distance in this study. In this condition, the number of neighboring particles is about 25-30 in 2D simulation, and 100-120 in 3D simulation. In order to search for neighboring particles, the intuitive approach is to search all particles through the whole computational domain based on the particle distance condition. This NNPS algorithm, however, is inefficient and takes tremendous computation time in proportion to the number of particles ($\sim N^2$). Therefore, for high-resolution analysis, an efficient NNPS algorithm is necessary, and a constant grid-based NNPS algorithm is adopted in this study. The grids at regular intervals are allocated for the entire computational domain depending on the users. After that, only the particles belonging to the grid adjacent to the center grid where the interesting particle i belongs are searched, and neighboring particles j within the search range are selected. The efficient searching calculation is possible through this NNPS algorithm, and the computation time is considerably reduced ($\sim N \ln N$). [Xia, 2016] Figure 2.4 shows the NNPS algorithm applied in this study.

2.3.2 Algorithm of SPH Code

The SPH code (SOPHIA code in this study) starts with the initial properties of the particles. Then, the initialization of the cell and particle is performed and sorted based on the index of the cell and particle. After, the nearest neighbor particle searching (NNPS) of the interesting particle i is conducted. And the density of the particle is estimated based on the mass conservation equation (Equation (2.8) and (2.9)). After that, the pressure of the particle is calculated by Equation (2.13) using the estimated density. Then, the interactions among particles such as pressure force, viscous force, and heat transfer, etc. are calculated by Equation (2.10)-(2.12), (2.19)-(2.22). Finally, the properties of particles are updated and previous processes are repeated until the calculation is completed. Figure 2.5 shows the simplified algorithm of the SOPHIA code.

2.3.3 Time Integration

The SOPHIA code is adopted a predictor-corrector scheme for the time integration. This method has two steps which are the predictor step and the corrector step. In the predictor step, the properties such as velocity, position, temperature, etc. are predicted at half of the time-step.

$$\mathbf{u}_{t+\frac{\Delta t}{2}}^p = \mathbf{u}_t + \frac{\Delta t}{2} \left(\frac{d\mathbf{u}}{dt} \right)_{t-\frac{\Delta t}{2}} \quad (2.23)$$

$$\mathbf{r}_{t+\frac{\Delta t}{2}}^p = \mathbf{r}_t + \frac{\Delta t}{2} \left(\frac{d\mathbf{r}}{dt} \right)_{t-\frac{\Delta t}{2}} \quad (2.24)$$

$$T_{t+\frac{\Delta t}{2}}^p = T_t + \frac{\Delta t}{2} \left(\frac{dT}{dt} \right)_{t-\frac{\Delta t}{2}} \quad (2.25)$$

where t and Δt mean time and time-step. The superscript p denotes predictor-step. Using these predicted values the SPH governing equations are calculated. Then, the final estimation of properties are calculated based on the corrector-step which is updated at the whole time-step.

$$\mathbf{u}_{t+\Delta t}^c = \mathbf{u}_t + \Delta t \left(\frac{d\mathbf{u}}{dt} \right)_{t+\frac{\Delta t}{2}} \quad (2.26)$$

$$\mathbf{r}_{t+\Delta t}^c = \mathbf{r}_t + \Delta t \left(\frac{d\mathbf{r}}{dt} \right)_{t+\frac{\Delta t}{2}} \quad (2.27)$$

$$T_{t+\Delta t}^c = T_t + \Delta t \left(\frac{dT}{dt} \right)_{t+\frac{\Delta t}{2}} \quad (2.28)$$

2.3.4 GPU Parallelization

Since the numerical expressions used in the SPH method are highly linear and calculations of particles are performed explicitly, there is no problem even if the calculations of particles are conducted independently. Therefore, the SPH method is optimized for GPU (Graphic Processor Unit) parallelization, and it is essential

for reducing SPH interpolation errors by using many SPH particles and for high-resolution simulations.

GPU is composed of several blocks and several threads in each block as shown in Figure 2.6. All particles participating in the simulation are allocated to each thread, and the same calculation is performed simultaneously in parallel for all thread. The calculation of neighboring particle j is performed through a ‘for statement’ within each thread, and summation operation of the estimated value is carried out through parallel reduction as shown in Figure 2.7. SOPHIA code has been parallelized based on NVIDIA CUDA architecture (GPGPU). The computation of GPU parallelization over CPU calculation shows a very remarkable computational speed, and the efficiency increases as the number of particles increase shown in Figure 2.8

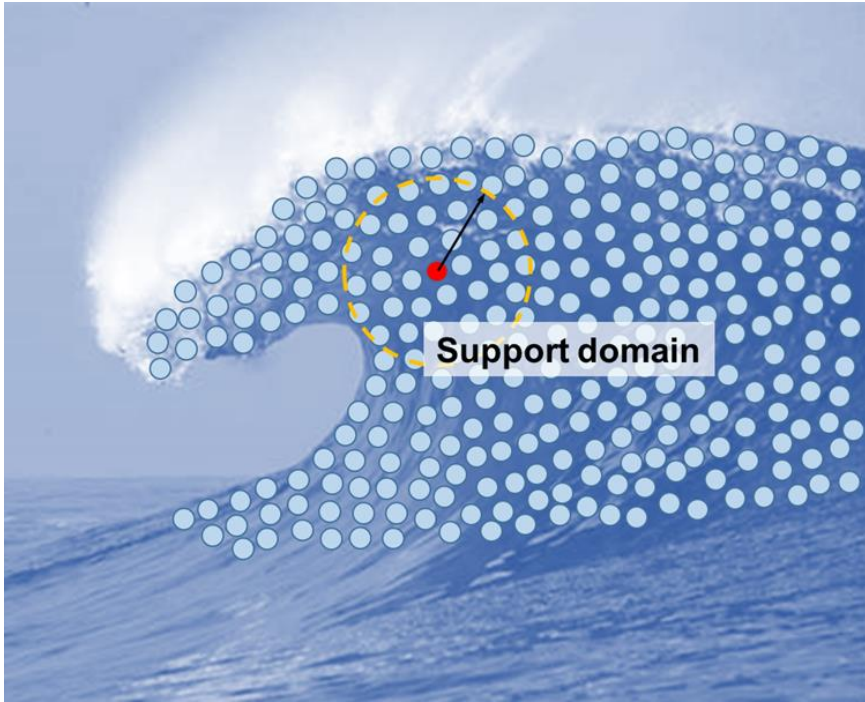


Figure 2.1 Flow analysis represented by SPH particles

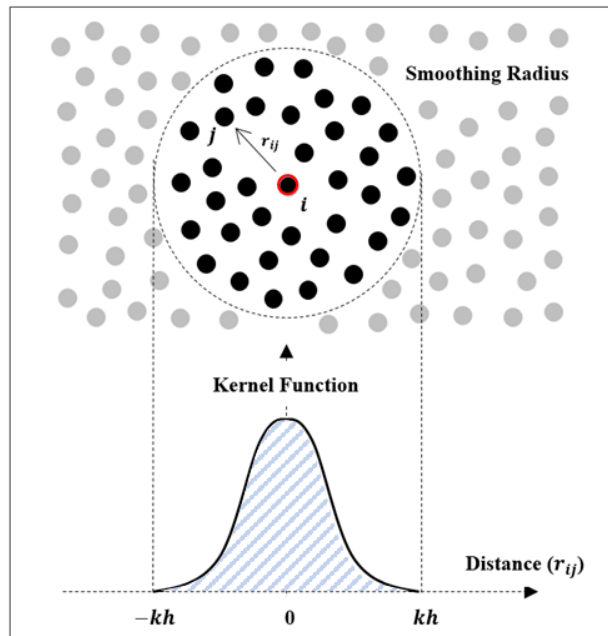


Figure 2.2 SPH kernel approximation

Table 2.1 SPH formulations for the governing equations

Mass conservation
Direct mass summation
$\rho_i = \sum_j m_j W_{ij}$
Continuity equation
$\frac{d\rho_i}{dt} = -\rho_i \sum_j \frac{m_j}{\rho_j} (\mathbf{u}_i - \mathbf{u}_j) \cdot \nabla W_{ij}$
Momentum conservation
Pressure gradient force
$\left(-\frac{1}{\rho} \nabla P\right)_i = -\sum_j m_j \left(\frac{P_i}{\rho_i^2} + \frac{P_j}{\rho_j^2}\right) \nabla W_{ij}$
Laminar viscous force
$\left(\frac{\mu}{\rho} \nabla^2 \mathbf{u}\right)_i = \sum_j \frac{4m_j}{\rho_i \rho_j} \frac{\mu_i \mu_j}{\mu_i + \mu_j} \frac{\mathbf{r}_{ij} \cdot \nabla W_{ij}}{r_{ij}^2 + \varepsilon^2} (\mathbf{u}_i - \mathbf{u}_j)$
Energy conservation
Conduction equation (enthalpy-based)
$\left(\frac{dH}{dt}\right)_i = \sum_j \frac{m_j}{\rho_i \rho_j} \frac{4k_i k_j}{k_i + k_j} \frac{\mathbf{r}_{ij} \cdot \nabla W_{ij}}{r_{ij}^2 + \varepsilon^2} (T_i - T_j)$
Equation of State (EOS)
$P_i = \frac{c_0^2 \rho_{ref,i}}{\gamma} \left[\left(\frac{\rho_i}{\rho_{ref,i}}\right)^\gamma - 1 \right]$

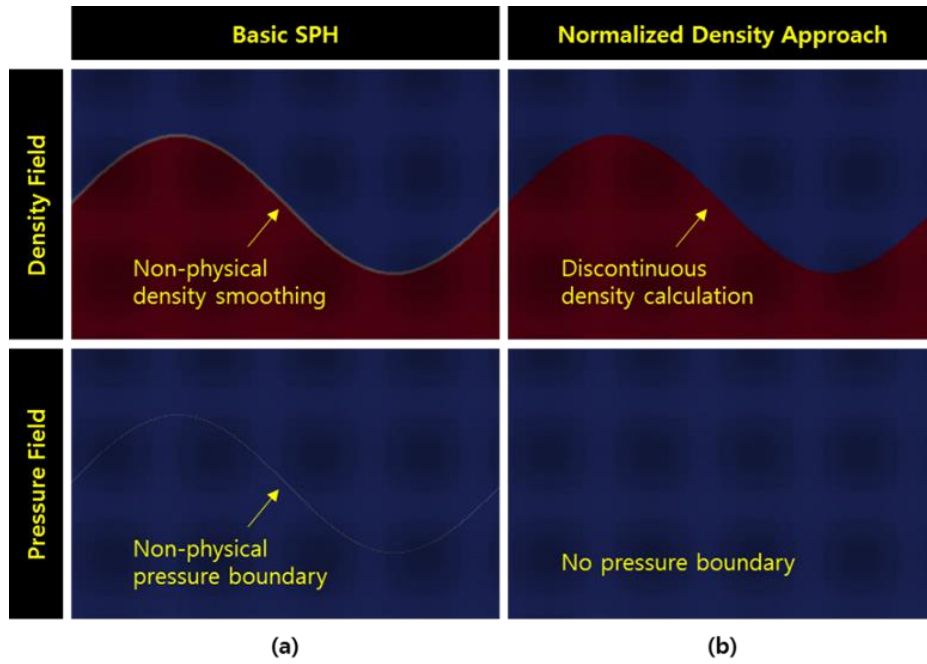


Figure 2.3 SPH results of density & pressure field:
 (a) Basic SPH method, (b) Normalized density approach

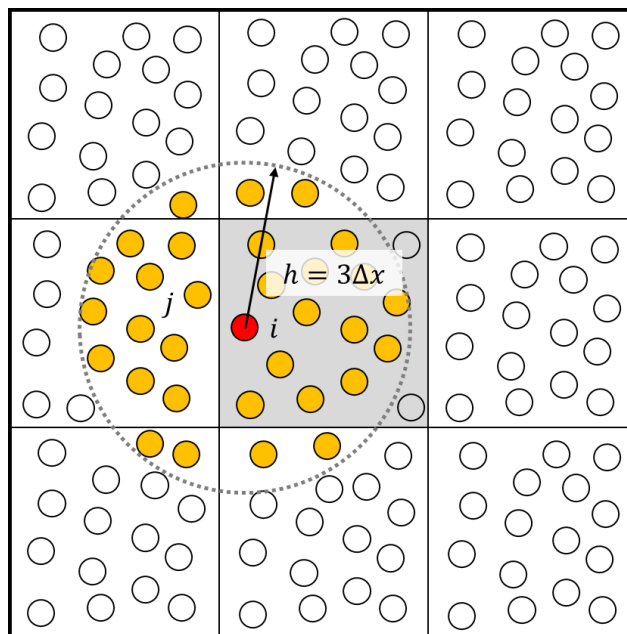


Figure 2.4 Grid-based NNPS

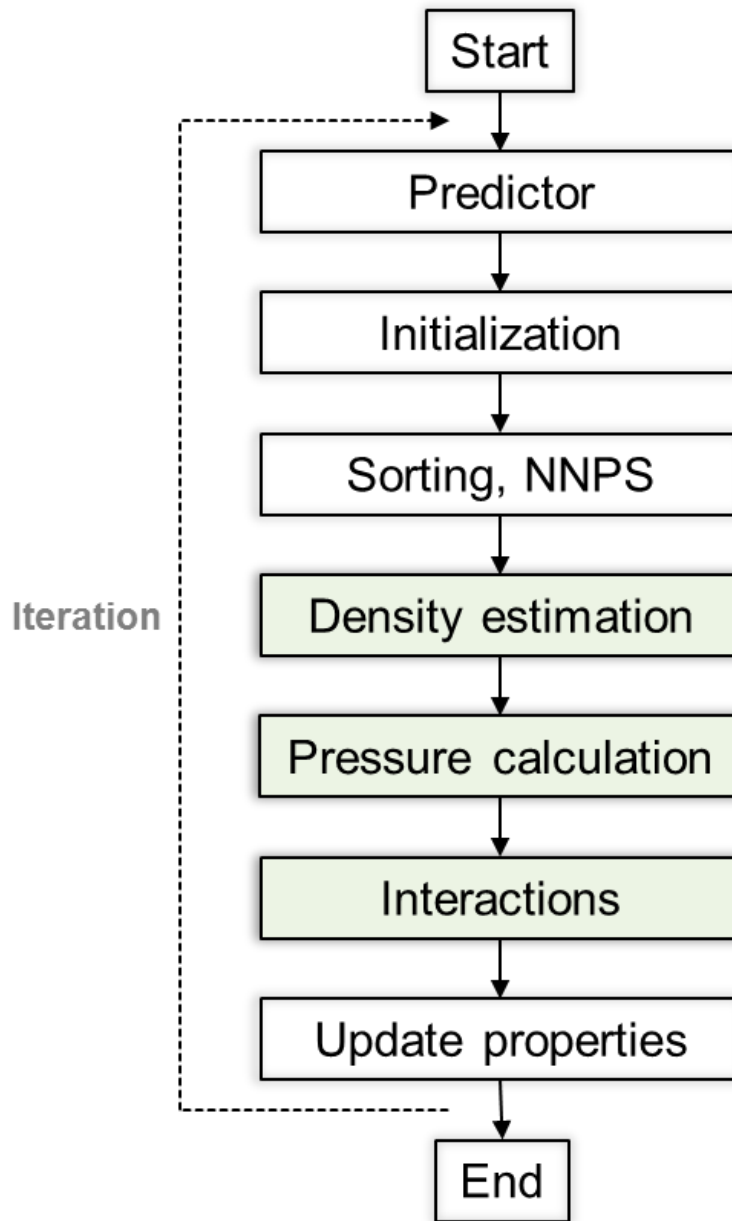


Figure 2.5 Algorithm of SPH code

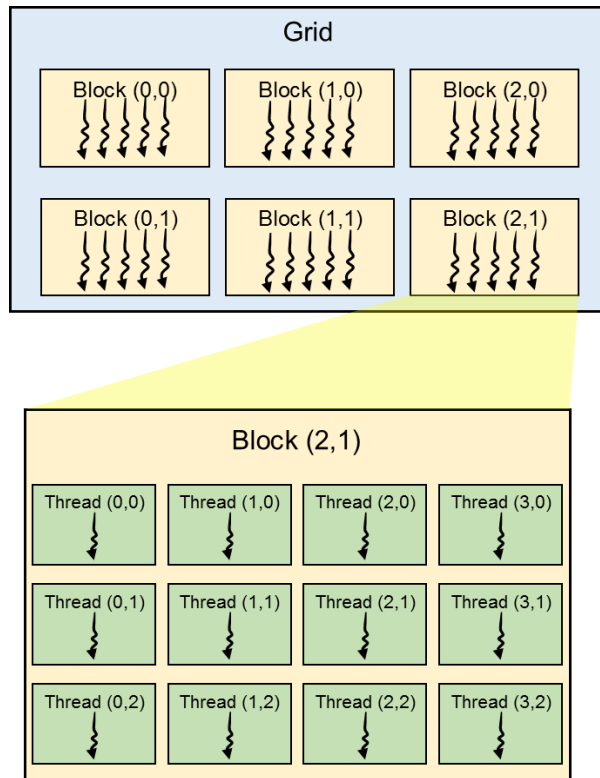


Figure 2.6 Simplified CUDA architecture

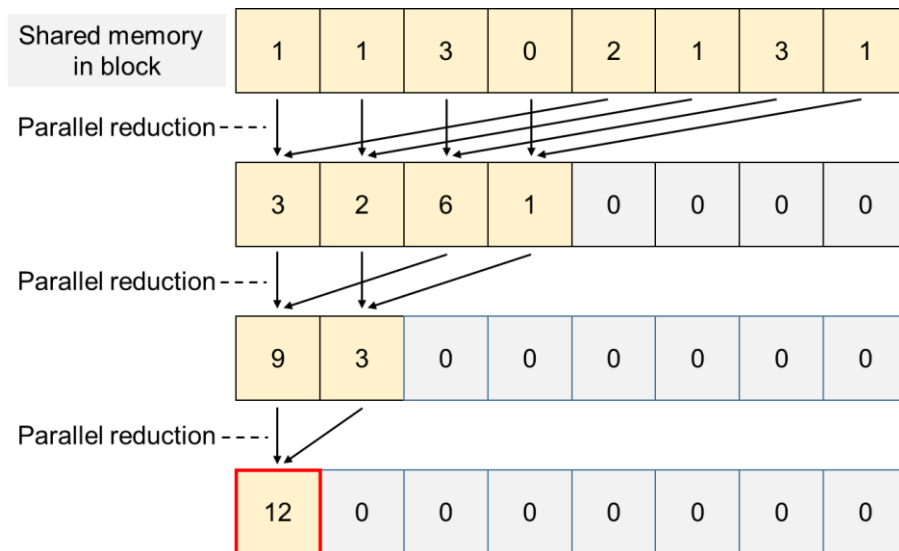


Figure 2.7 GPU parallel reduction

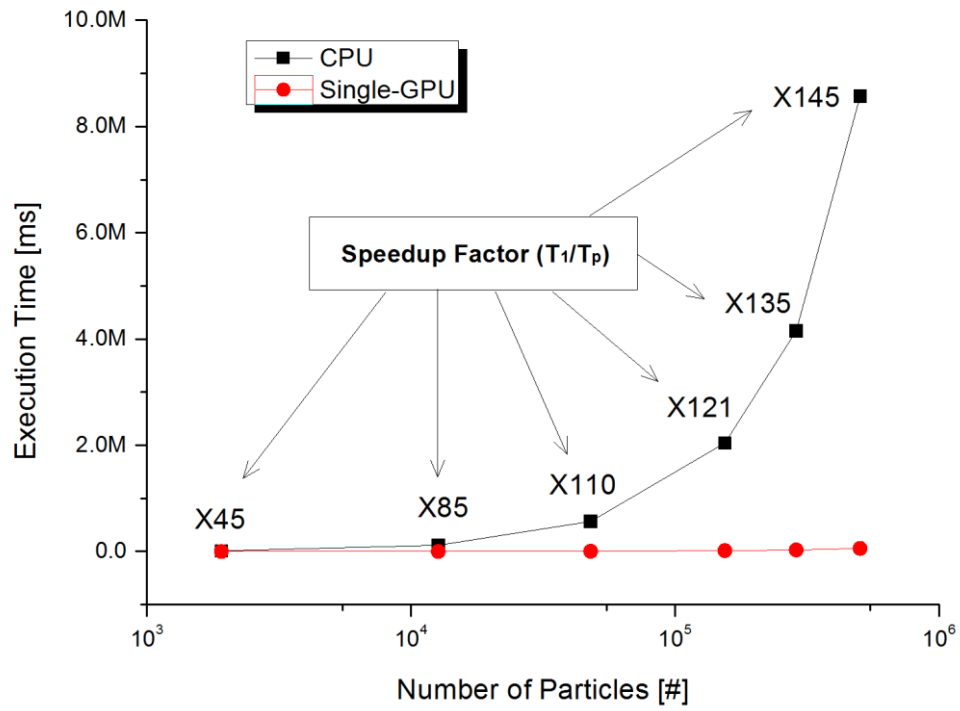


Figure 2.8 Speedup after GPU parallelization

Chapter 3

Rigid Body Dynamics (RBD)

3.1 RBD Overview

For the analysis of non-spherical solids, particle-based rigid body dynamics is applied in this study. Rigid body dynamics (hereafter RBD) is a study that analyzes the translation and rotation of a solid body by using the concept that a rigid body doesn't change its shape from applied external forces. RBD is commonly used in the animation graphic field and many engineering fields such as coastal Eng., soil Eng., etc. There are various methods for rigid body analysis, and basically, the motion of a rigid body is analyzed by calculating the net force and torque based on the center of mass. (Figure 3.1)

In the grid-based Eulerian method, the rigid body is expressed by polygon or mesh, and it is very complex and time-consuming to determine the collision of rigid bodies with complex shapes. As shown in Figure 3.2, the collision of rigid bodies can be detected by carrying a function for each face based on the center of mass or when the orthographic projections of each vertex on the center of mass overlap each other. In the particle-based Lagrangian method, on the other hand, the complex shape of the solid can be easily represented by a particle-discretized rigid body, and the collision detection is simple which can be determined by the contact of particle

pairs. (Figure 3.3) In this study, a rigid body is expressed as a group of particles based on the latter case.

In order to select an appropriate collision analysis method comparisons of several collision methods were performed, which will be addressed in Section 3.2. Then, the adopted rigid body collision model and the algorithm of RBD in this study are described in Section 3.3. For the effective rigid body calculation, GPU-based parallelization was performed (Section 3.4), and the verification and validation for the rigid body model applied in this study are dealt with in Section 3.5.

3.2 Collision Models of Rigid Body

To apply an appropriate rigid-body collision model to this study, several methods suggested in the existing literature were investigated, and the comparisons were performed by applying models.

3.2.1 Monaghan Boundary Force (MBF) Model

The Monaghan Boundary Force (MBF) is a method proposed by Monaghan, a well-known pioneer in the SPH field. [Monaghan, 2003] It is the simplest method to apply and acts as a kind of repulsive force, which calculates the interaction force when the spacing of the particles in the collision candidates is close sufficiently. As seen from Equation (3.1)-(3.3), the collision force is determined by the mass and positions of the collision particles, and the normal vector is set by connecting the center of particles.

$$F_M(x, y) = -\frac{0.02c_s^2}{y} \frac{m_a m_b}{m_a + m_b} \Gamma(y) \chi(x) \hat{\mathbf{n}} \quad (3.1)$$

$$\Gamma(y) = \begin{cases} 0.6667 & 0 < q < 0.6667 \\ 2q - 1.5q^2 & \text{for } 0.6667 < q < 1 \\ 0.5(2 - q)^2 & 1 < q < 2 \\ 0 & \text{otherwise} \end{cases} \quad (3.2)$$

$$\chi(x) = \begin{cases} 1 - x/\Delta x & \text{for } 0 < x < \Delta x \\ 0 & \text{otherwise} \end{cases} \quad (3.3)$$

where c_s , y , m denote the sound of speed, and relative position to y -direction, and mass of the particle respectively. The $\frac{0.02c_s^2}{y}$ term on the RHS is an estimate of the maximum force/mass necessary to stop a particle moving at the estimated maximum speed in the simulation. $\Gamma(y)$, $\chi(x)$ are kind of scaling factors along with the two coordinate directions. $\Gamma(y)$ is derived from the gradient of the kernel function, and $\chi(x)$ can provide proper weight factors so that nearby particles receive a constant force in the tangential direction. q is obtained by dividing the y by the smoothing length h , and Δx means the initial particle spacing.

MBF method has a remarkable simplicity and efficiency to calculate the interactions, but it has the following limitations. First, the calculated force isn't based on the physical collision between particles since this method is to prevent the penetration of particles with maximum speed in the simulation into the inside of a rigid. Also, the force is a function of the particle's position only, other properties such as the velocity are not considered in the collision process. Therefore, it can't estimate the exact collision direction and magnitude of the bodies, which induces a potential instability in simulations. [Oh, 2009]

3.2.2 Ideal Plastic Collision Model

In soil engineering, the soil to be analyzed sometimes contains moisture and tends to move together when it collides with solid structures, so the collision calculation is performed based on the ideal plastic collision model. [Wang, 2014] [Zhan, 2020] Therefore, the collision is calculated based on the impenetration condition and sticking condition. If the distance between the two particles is closer than the initial particle spacing (Δx) and the particles approach each other, the contact force calculation starts.

$$\text{Collision detection} \quad d_s = r_i + r_j < \Delta x \quad (3.4)$$

$$\text{Penetration rate} \quad (\mathbf{u}_j^p - \mathbf{u}_i^p) \cdot \mathbf{n}_i < 0 \quad (3.5)$$

r is the radius of the colliding particle, \mathbf{u}_p is the predicted velocity, and \mathbf{n}_i is the normal vector of particle i . The corrected velocity can be obtained by the collision force \mathbf{F}_{ij} , and the following equation is valid to satisfy the impenetration condition in the normal direction.

$$\mathbf{u}_i^c = \mathbf{u}_i^p + \Delta t \frac{\mathbf{F}_{ij}}{m_i} \quad (3.6)$$

$$\mathbf{u}_j^c = \mathbf{u}_j^p - \Delta t \frac{\mathbf{F}_{ij}}{m_j} \quad (3.7)$$

$$d_n^c = (\mathbf{u}_i^c - \mathbf{u}_j^c) \cdot \mathbf{n}_i = 0 \quad (3.8)$$

Δt denotes the time-step of the simulation. Substituting into Equation (3.8), the normal contact force is represented in the following equation.

$$\mathbf{F}_{ij}^n = \frac{[\mathbf{n}_i \cdot (\mathbf{u}_i^p - \mathbf{u}_j^p)] \mathbf{n}_i}{\frac{\Delta t}{m_i} + \frac{\Delta t}{m_j}} = \mathbf{u}_n \left(\frac{\Delta t}{m_i} + \frac{\Delta t}{m_j} \right)^{-1} \quad (3.9)$$

By the sticking assumption, the relative sliding rate can be expressed as,

$$d_\tau = |(\mathbf{u}_i^p - \mathbf{u}_j^p) - [\mathbf{n}_i \cdot (\mathbf{u}_i^p - \mathbf{u}_j^p)] \mathbf{n}_i| = 0 \quad (3.10)$$

The tangential contact force is derived as follows.

$$\mathbf{F}_{ij}^{t, sticking} = \frac{(\mathbf{u}_i^p - \mathbf{u}_j^p) - [\mathbf{n}_i \cdot (\mathbf{u}_i^p - \mathbf{u}_j^p)] \mathbf{n}_i}{\frac{\Delta t}{m_i} + \frac{\Delta t}{m_j}} = \mathbf{u}_t \left(\frac{\Delta t}{m_i} + \frac{\Delta t}{m_j} \right)^{-1} \quad (3.11)$$

Considering the friction by the Coulomb law of friction, the tangential contact force can be expressed as

$$\mathbf{F}_{ij}^t = \begin{cases} \mathbf{F}_{ij}^{t, sticking} & |\mathbf{F}_{ij}^{t, sticking}| < \mu |\mathbf{F}_{ij}^n| \\ \mu |\mathbf{F}_{ij}^n| \mathbf{t}_i & |\mathbf{F}_{ij}^{t, sticking}| \geq \mu |\mathbf{F}_{ij}^n| \end{cases} \quad (3.12)$$

3.2.3 Impulse-based Boundary Force (IBF) Model

Impulse-based Boundary Force (IBF) calculates the collision force based on the actual physical equations, and the contact force can be obtained from the estimated impulse. [Park, 2011] [Li, 2018] The velocity of the particle considering the angular velocity can be expressed as follows.

$$\mathbf{u}_{cp_a}^- = \mathbf{u}_a^- + \mathbf{w}_a^- \times \mathbf{rc}_a \quad (3.13)$$

$$\mathbf{u}_{cp_b}^- = \mathbf{u}_b^- + \mathbf{w}_b^- \times \mathbf{rc}_b \quad (3.14)$$

$$\mathbf{rc}_{i=a,b} = (\mathbf{r}_{cp_i} - \mathbf{r}_{cm_i}) \quad (3.15)$$

where \mathbf{rc} means the position vector, and subscript cp, cm mean contact point and center of mass; w denotes angular velocity; and $(-), (+)$ denote before and after the collision. From Equation (3.13)-(3.14), the relative velocity at the before and after the collision can be expressed. From Newton's law of impact, Equation (3.18) is valid using the relative velocity relation.

$$\mathbf{u}_{rel}^- = \hat{\mathbf{n}} \cdot (\mathbf{u}_{cp_a}^- - \mathbf{u}_{cp_b}^-) \quad (3.16)$$

$$\mathbf{u}_{rel}^+ = \hat{\mathbf{n}} \cdot (\mathbf{u}_{cp_a}^+ - \mathbf{u}_{cp_b}^+) \quad (3.17)$$

$$\mathbf{u}_{rel}^+ = -e\mathbf{u}_{rel}^- \quad (3.18)$$

where e is a restitution coefficient ($0 < e < 1$). The impulse J produced from time t_1 to t_2 and from Newton's second law, force is represented using linear momentum.

$$J = \int_{t_1}^{t_2} F dt = \int_{t_1}^{t_2} \frac{d\mathbf{p}}{dt} dt = \int_{t_1}^{t_2} d\mathbf{p} = \Delta\mathbf{p} \quad (3.19)$$

Substituting equation (3.16)-(3.19), the magnitude of impulse j can be derived as follows.

$$\mathbf{u}_{cp_a}^+ = \mathbf{u}_a^+ + \mathbf{w}_a^+ \times \mathbf{r}c_a = \mathbf{u}_{cp_a}^- + j \left[\frac{j\hat{\mathbf{n}}}{M_a} + I_a^{-1}(\mathbf{r}c_a \times \hat{\mathbf{n}}) \times \mathbf{r}c_a \right] \quad (3.20)$$

$$\mathbf{u}_{cp_b}^+ = \mathbf{u}_b^+ + \mathbf{w}_b^+ \times \mathbf{r}c_b = \mathbf{u}_{cp_b}^- + j \left[\frac{j\hat{\mathbf{n}}}{M_b} + I_b^{-1}(\mathbf{r}c_b \times \hat{\mathbf{n}}) \times \mathbf{r}c_b \right] \quad (3.21)$$

Using the velocity and angular velocity after collision $\mathbf{u}_{i=a,b}^+ = \mathbf{u}_i^- + \frac{j\hat{\mathbf{n}}}{M_i}$ and $\mathbf{w}_i^+ = \mathbf{w}_i^- + I_i^{-1}[(\mathbf{r}_{cp_i} - \mathbf{r}_{cm_i}) \times \mathbf{J}]$, the final expression of the impulse is derived as Equation (3.22).

$$j = \frac{-(1+e)\mathbf{u}_{rel}^- \cdot \hat{\mathbf{n}}}{\sum_{i=\{a,b\}} \left(M_i^{-1} + \left(I_i^{-1}(\mathbf{r}c_i \times \hat{\mathbf{n}}) \times \mathbf{r}c_i \right) \cdot \hat{\mathbf{n}} \right)} \quad (3.22)$$

From Equation (3.22), the normal contact force based on IBF is expressed as

$$\mathbf{F}_{ij}^n = -\frac{j_n \hat{\mathbf{n}}}{\Delta t} \quad (3.23)$$

$$j_n = \frac{-(1+e)\mathbf{u}_{ab} \cdot \hat{\mathbf{n}}}{\sum_{i=\{a,b\}} \left(M_i^{-1} + \left(\left(I_i^{-1}(\mathbf{r}c_i \times \hat{\mathbf{n}}) \right) \times \mathbf{r}c_i \right) \cdot \hat{\mathbf{n}} \right)} \quad (3.24)$$

Also, the tangential contact force is calculated as follows.

$$\mathbf{F}_{ij}^t = \begin{cases} -\frac{j_t \hat{\mathbf{n}}}{\Delta t} & (|j_t| < \mu_{ij}|j_n|) \\ -\frac{(\mu_{ij}j_n)\hat{\mathbf{n}}}{\Delta t} & (|j_t| \geq \mu_{ij}|j_n|) \end{cases} \quad (3.25)$$

$$j_t = \frac{|\mathbf{u}_t|}{\sum_{i=\{a,b\}} \left(M_i^{-1} + \left(\left(I_i^{-1}(\mathbf{r}c_i \times \hat{\mathbf{n}}) \right) \times \mathbf{r}c_i \right) \cdot \hat{\mathbf{n}} \right)} \quad (3.26)$$

3.2.4 Penalty-based Contact Model

For the collision model between rigid bodies, a penalty-based contact model that calculates the collision force based on the slight overlap between collision particles was considered. A penalty-based contact force model was first proposed by Cundall and Strack (1979) to analyze the collision of two particles, and the normal contact force is calculated in linear proportion to the overlap of the two particles. On the other hand, a non-linear system was proposed by Hertz's theory (Hertz, 1882), and the normal contact force is calculated in proportion to the 3/2

power of the overlap. A tangential contact force was proposed by Mindlin and Deresiewicz (1953), and the Hertz-Mindlin contact force model was derived by combining two models. Hertz-Mindlin model is commonly used in DEM and also applied in this study.

The calculation of contact force starts when the distance is less than the initial particle spacing like Equation (3.4). Then, the normal and tangential of contact force is estimated by the slight overlap. The normal component of the contact force is composed of the elastic spring force and the damping force. (Figure 3.4) It can be expressed as follows in non-linear proportion to the normal overlap(δ_n).

$$\mathbf{F}_{ij}^n = \mathbf{f}_{ij}^{n,r} + \mathbf{f}_{ij}^{n,d} = -k_n \delta_n^{1.5} \hat{\mathbf{n}} + c_n \delta_n^{0.25} \mathbf{u}_n \quad (3.27)$$

$$k_n = \frac{4}{3} E^* \sqrt{R^*} \quad (3.28)$$

$$c_n = \sqrt{\frac{10}{3}} \frac{\ln(e)}{\sqrt{\ln(e)^2 + \pi^2}} \sqrt{M^* K_n'}, \quad K_n' = 2E^* \sqrt{R^*} \quad (3.29)$$

where superscript n, r, d means the normal direction, repulsive spring force, and damping force respectively. k_n, c_n mean spring stiffness and damping coefficient of normal direction, $\hat{\mathbf{n}}, \mathbf{u}_n$ are unit normal vector and relative normal velocity of the two particles. E^*, G^*, R^*, M^* denote an equivalent value of Young's modulus, shear modulus, radius, and mass of the particle, and expressed as follows.

$$E^* = \left(\frac{1 - \nu_i^2}{E_i} + \frac{1 - \nu_j^2}{E_j} \right)^{-1} \quad (3.30)$$

$$G^* = \left(\frac{2 - \nu_i}{G_i} + \frac{2 - \nu_j}{G_j} \right)^{-1} \quad (3.31)$$

$$R^* = \left(\frac{1}{r_i} + \frac{1}{r_j} \right)^{-1} \quad (3.32)$$

$$M^* = \left(\frac{1}{m_i} + \frac{1}{m_j} \right)^{-1} \quad (3.33)$$

Similarly, the tangential contact force can be calculated as the repulsive force and damping force using the tangential overlap (δ_t), and friction force is considered additionally.

$$\mathbf{F}_{ij}^t = \begin{cases} \mathbf{f}_{ij}^{t,r} + \mathbf{f}_{ij}^{t,d} = -k_t \delta_t \hat{\mathbf{t}} + c_t \mathbf{u}_t & |\mathbf{F}_{ij}^t| < \mu_{ij} |\mathbf{F}_{ij}^n| \\ \mathbf{f}_{ij}^{t,friction} = -\mu_{ij} |\mathbf{F}_{ij}^n| \hat{\mathbf{t}} & |\mathbf{F}_{ij}^t| \geq \mu_{ij} |\mathbf{F}_{ij}^n| \end{cases} \quad (3.34)$$

$$k_t = 8G^* \sqrt{R^* \delta_n} \quad (3.35)$$

$$c_t = \sqrt{\frac{10}{3}} \frac{\ln(e)}{\sqrt{\ln(e)^2 + \pi^2}} \sqrt{M^* k_t} \quad (3.36)$$

where superscript t means the tangential direction. k_t, c_t mean spring stiffness

and damping coefficient of tangential direction, $\hat{\mathbf{t}}, \mathbf{u}_t$ are unit tangential vector and relative tangential velocity of the two particles. By considering both the normal and tangential components, the overall contact force between particles is expressed as follows.

$$\mathbf{F}_{ij}^c = \mathbf{F}_{ij}^n + \mathbf{F}_{ij}^t \quad (3.37)$$

3.2.5 Determination of Collision Model

In order to adopt an appropriate collision analysis method to be applied in this study, comparisons among the four methods described above were performed. The simulations were carried out in a perfectly elastic collision ($e = 1$), and Table 3.1 shows the momentum, angular momentum, and energy conservation calculated through each method. In the collision, the force exerted by two colliding particles is equal in magnitude and opposite in direction due to the action-reaction. Therefore, linear momentum and angular momentum were perfectly conserved in all methods.

In the case of the MBF model, the contact force (more precisely, the repulsive force) is calculated so that particles don't penetrate each other through the position information between the two particles. Therefore, the MBF model is not based on the physical collision and the kinetic energy conservation is not conserved.

In the case of the ideal plastic collision model, the contact force calculation is basically performed based on the sticking assumption. Therefore, when the contact of solid bodies is detected according to the distance condition, the bodies stick to each other rather than repel each other in this method. (Figure 3.5)

In both cases of the IBF model and the spring-dashpot model, the kinetic energy is well conserved as shown in Table 3.1, which is not conserved in the MBF model and ideal plastic model. So, the simulation of elastic collision shows good results without energy loss. In the IBF model as described in Section 3.2.3, however, many mathematical operations are required to analyze the collision. This induces a higher computational time under the conditions implemented in this code. In this study, therefore, rigid body collision was performed based on the spring-dashpot model, and the details will be dealt with in the next sections.

3.3 Algorithm of RBD

3.3.1 Calculation of Rigid Body Information

In this study, a rigid body is expressed as a finite number of particles as shown in Figure 3.3. Therefore, the information of the rigid body can be easily calculated from the information of the particles constituting the rigid body. To calculate the contact force of rigid bodies, the total mass and center of mass should be calculated firstly as follows.

The number of particle constituting rigid body

$$num_I = \sum_I 1 \quad (3.38)$$

The total mass of rigid body

$$M_I = num_I \cdot m_i \quad (3.39)$$

Center of mass of rigid body

$$\mathbf{r}_{cm} = \frac{1}{M_I} \sum_I m_i \mathbf{r}_i \quad (3.40)$$

3.3.2 Contact Detection

Particle-based rigid body contact can be easily detected as collisions between particles of each rigid body. Therefore, if the other rigid body particle comes into the search range, the distance condition of the particles is calculated. Then, if the calculated distance is less than the sum of the radius of the two particles, it is determined that a collision of the bodies occurs. This can be expressed as the normal overlap(δ_n) as follows.

$$d_{ij} = |\mathbf{r}_{ij}| \quad (3.41)$$

$$\delta_n = r_i + r_j - d_{ij} \geq 0 \quad (3.42)$$

3.3.3 Contact Normal Calculation

Next, in order to calculate the direction of contact force, the conventional DEM method estimates the contact normal direction based on the center of the particles. (Figure 3.6) In this study, however, since finite particles constitute a rigid body when the collision direction is calculated as a mentioned process, the contact force can be calculated in an incorrect direction as shown in Figure 3.7.

To resolve this issue, Junior (2019) proposed an improved contact normal vector method, which defines the normal vector according to the types of colliding particles. For example, in a cube-shaped rigid body, rigid particles can be located on the face, edge, and vertex. (Figure 3.8) This can be determined by the number of particles that are in contact with. (5 in face, 4 in edge, and 3 in vertex) If at least one of the two particles is located on the surface, the contact normal vector is determined as the corresponding surface normal vector. On the other hand, if neither particle is located on the surface, the normal vector is determined based on the center of the colliding particles, which is used in conventional DEM.

- ◆ If i particle is on the face,

$$\hat{\mathbf{n}}_c = \hat{\mathbf{n}}_i \quad (\text{The normal of } i \text{ particle})$$

- ◆ If i is not on the face, but j is on the face,

$$\hat{\mathbf{n}}_c = -\hat{\mathbf{n}}_j \quad (\text{The reverse normal of } j \text{ particle})$$

- ◆ If i, j both particles are not on the face,

$$\hat{\mathbf{n}}_c = \left(\frac{\mathbf{r}_{ij}}{|\mathbf{r}_{ij}|} \right) \quad (\text{Unit distance vector})$$

Using the well-defined contact normal vector and the normal overlap, the position vector and the relative velocity at the contact point can be obtained as follows. (Figure 3.9)

$$\mathbf{x}_{cp} = \mathbf{x}_i + (r_i - 0.5\delta_n) \cdot \hat{\mathbf{n}} \quad (3.43)$$

$$\mathbf{u}_{rel} = (\mathbf{u}_j + \mathbf{w}_j \times (\mathbf{x}_{cp,j} - \mathbf{x}_{cm,j})) - (\mathbf{u}_i + \mathbf{w}_i \times (\mathbf{x}_{cp,i} - \mathbf{x}_{cm,i})) \quad (3.44)$$

where $\mathbf{x}, \mathbf{u}, \mathbf{w}$ denotes the position vector from the zero point, the velocity, and the angular velocity, respectively. Subscript cp, cm mean the contact point and center of mass, respectively. $\mathbf{x}_{cm,a}$ means the center of the mass position vector of the rigid body belonging particle $a(= i, j)$. From the calculated relative velocity at the contact point, the normal and tangential relative velocity vector can be expressed as

$$\mathbf{u}_n = |\mathbf{u}_{rel} \cdot \hat{\mathbf{n}}| \quad (3.45)$$

$$\mathbf{u}_t = \mathbf{u}_{rel} - \mathbf{u}_n \quad (3.46)$$

where subscript n, t denote the normal direction and tangential direction, respectively. Using this, the tangential unit vector and the tangential overlap(δ_t) can be defined.

$$\hat{\mathbf{t}} = \frac{\mathbf{u}_t}{|\mathbf{u}_t|} \quad (3.47)$$

$$\delta_t = \delta_{t,0} + |\mathbf{u}_t| \Delta t \quad (3.48)$$

where Δt means the time step of the simulation.

3.3.4 Contact Force Calculation

Using the information of the position and velocity of the colliding particles at the contact point, the contact force in the normal and tangential direction is calculated based on the spring-dashpot model mentioned in Section 3.2.4. (Equation (3.49)-(3.50))

◆ Normal contact force

$$\mathbf{F}_{ij}^n = \mathbf{f}_{ij}^{n,r} + \mathbf{f}_{ij}^{n,d} = -k_n \delta_n^{1.5} \hat{\mathbf{n}} + c_n \delta_n^{0.25} \mathbf{u}_n \quad (3.49)$$

$$c_n = \sqrt{\frac{10}{3}} \frac{\ln(e)}{\sqrt{\ln(e)^2 + \pi^2}} \sqrt{M^* K'_n}, \quad K'_n = 2E^* \sqrt{R^*}$$

◆ Tangential contact force

$$\mathbf{F}_{ij}^t = \begin{cases} \mathbf{f}_{ij}^{t,r} + \mathbf{f}_{ij}^{t,d} = -k_t \delta_t \hat{\mathbf{t}} + c_t \mathbf{u}_t & |\mathbf{F}_{ij}^t| < \mu_{ij} |\mathbf{F}_{ij}^n| \\ \mathbf{f}_{ij}^{t,friction} = -\mu_{ij} |\mathbf{F}_{ij}^n| \hat{\mathbf{t}} & |\mathbf{F}_{ij}^t| \geq \mu_{ij} |\mathbf{F}_{ij}^n| \end{cases} \quad (3.50)$$

The original form of damping term in the Mindlin model is proportional to the 0.25 power of the normal overlap(δ_n) as seen in Equation (3.49), but the exact damping force may not be calculated in the particle-discretized rigid body. Various studies on the damping term have been widely conducted to predict solid motion. [Hu, 2011] [Caserta, 2016] In this study, the damping coefficient proposed by Caserta (2016) has been used.

$$\hat{\delta}_n(t) + c_n \hat{\delta}_n(t)^{1.5} \hat{\delta}_n + \hat{\delta}_n(t)^{1.5} = 0 \quad (3.51)$$

$$c_n = -\frac{k_n}{u_0} \frac{a \cdot \ln(e)}{b + c \cdot \ln(e)} \quad (3.52)$$

where constant a, b, c have the value of 8.693764, 5.573076, and 1.966760, respectively. And u_0, e denote the impact velocity at the initial collision and the restitution coefficient. The second term of Equation (3.51) corresponds to the damping term and is proportional to 1.5 power of the normal overlap unlike 0.25 in Mindlin model.

Also, the frictional force was modified and implemented using the sigmoidal functions as follows, so that the velocity in the tangential direction has a continuous value at the origin. [Vetsch, 2011]

$$\mathbf{f}_{ij}^{t,friction} = -\mu_{ij} |\mathbf{F}_{ij}^n| \tanh(8\delta_t) \hat{\mathbf{t}} \quad (3.53)$$

where μ_{ij} means the kinetic friction coefficient between i and j particles, δ_t is the rate of tangential deformation.

By modifying the damping term and frictional term, a more accurate contact force calculation can be possible, and the V&V simulations will be dealt with in Section 3.5.

3.3.5 Summation of Rigid Body Particles

Through the above processes, the contact force applied to the particles can be calculated. And using the contact force of each particle, the total force applied to

the rigid body can be obtained by summing the forces calculated in all particles constituting the rigid body. Also, the total torque of the rigid body can be expressed from the contact force of each particle and the position vector from the center of mass to each particle.

$$M_I \frac{d\mathbf{u}_I}{dt} = \sum_{i \in \text{rigid } I} \mathbf{F}_i = \sum_{i \in \text{rigid } I} (\mathbf{F}_i^c + m_i \mathbf{g}) \quad (3.54)$$

$$I \frac{d\mathbf{w}_I}{dt} = \sum_{i \in \text{rigid } I} \boldsymbol{\tau}_i = \sum_{i \in \text{rigid } I} (\mathbf{r}_i - \mathbf{r}_{cm,i}) \times \mathbf{F}_i \quad (3.55)$$

In order to perform simulations on a large rigid body that is composed of many particles, a fast and efficient summation process is necessary. In this study, therefore, GPU parallelization on the summation process was performed and will be covered in Section 3.4.

3.3.6 Time Integration

The moment of inertia of the particles constituting the rigid body is expressed as follows.

$$I^{-1} = \begin{pmatrix} \sum m_i (y_i^2 + z_i^2) & -\sum m_i x_i y_i & -\sum m_i x_i z_i \\ -\sum m_i x_i y_i & \sum m_i (x_i^2 + z_i^2) & -\sum m_i y_i z_i \\ -\sum m_i x_i z_i & -\sum m_i y_i z_i & \sum m_i (x_i^2 + y_i^2) \end{pmatrix}^{-1} \quad (3.56)$$

Using the inertia of momentum, the velocity, angular velocity, and position of particles are updated and the behavior of the rigid body is analyzed. The overall algorithm of rigid body contact force is shown in Figure 3.10.

$$\mathbf{u}_i(t) = \mathbf{u}_{0,i} + \frac{\sum \mathbf{F}_i}{M_i} \Delta t \quad (3.57)$$

$$\mathbf{w}_i(t) = \mathbf{w}_{0,i} + I^{-1} \sum \boldsymbol{\tau}_i \Delta t \quad (3.58)$$

$$\frac{d\mathbf{r}_i(t)}{dt} = \mathbf{u}_i(t) + \mathbf{w}_i(t) \times (\mathbf{r}_i(t) - \mathbf{r}_{cm,i}(t)) \quad (3.59)$$

3.4 GPU Parallelization

The force applied by the rigid particles, equal to the fluid particles, can be calculated by the neighboring particles within the search range (Section 2.3.4). As mentioned in the previous section, in order to calculate the net force of the rigid body, the values of the particles constituting the rigid body should be summed. Since the size and shape of the rigid body are different from case by case, however, it is not easy to define an appropriate search range. Therefore, another efficient algorithm is needed to calculate the properties of the rigid body. In this study, the GPU parallelization algorithms were implemented to efficiently and quickly sum the properties of the particles for the entire analysis domain, which will be dealt with in the next subsection.

3.4.1 Algorithm 1: Atomic Operation

The summation on multiple rigid particles can be efficiently performed by using the GPU threads simultaneously. When performing operations between threads independently, the calculations are not affected by each other even if threads are activated at the same time. However, a memory racing condition can occur when performing successive operations among threads. For example, suppose that each thread reads the x value and adds 1 to x . The desired process is that a calculation is performed that reads $x=7$ in thread-1, adds 1 to return 8, and then reads $x=8$ in thread-2 and adds 1 to return 9, etc. However, if the threads are not properly synchronized, a memory racing condition, as the name suggests, can occur in which the value $x = 7$ is read from thread-2 before the operation is completed in thread-1. (Figure 3.11) For this, thread synchronization is necessary, and CUDA architecture provides an atomic operation function for accurate calculation.

The atomic operation function accesses memory to perform the calculation without the memory racing among threads. As can be seen in Figure 3.12, when the properties of unsorted rigid particles are listed in the threads, it is possible to access the desired address and store the value based on the rigid body number. Therefore, the properties of each rigid body can be estimated by storing the values of rigid particles in each memory. Through this, the properties of rigid particles can be summed efficiently and quickly without memory racing using the atomic operation. However, the efficiency can be varied depending on the type of memory to be stored. As shown in Figure 3.13, the CUDA memory structure can be represented briefly. Shared memory is accessible only among threads constituting the same block, whereas global memory is accessible by all threads. In this, shared memory has the

advantage of fast access speed while the memory size is small, while global memory has a large memory size but has a slow access speed. Therefore, the efficiency of the GPU parallelization algorithm may vary depending on the memory type used in the code.

At first, in this study, the GPU parallelization algorithm was executed to access only global memory and store values. For computational efficiency, the threads in each block store values in the shared memory, and then access the global memory only as much as the number of blocks. The former has significantly low computation speed due to the access number as much as the number of particles ($\approx \text{block} * \text{thread}$). On the other hand, the latter algorithm using the shared memory improves the computational speed very efficiently only with the access number as much as blocks. (Figure 3.14) Although reduction of rigid bodies is carried out very efficiently, there is a limitation in that the number of rigid bodies is constrained due to the small shared memory size.

3.4.2 Algorithm 2: Sorting

In order to simulate a large number of rigid bodies case, a new GPU parallelization algorithm is needed. For this, CUBLAS MPI function was applied to perform the reduction on rigid particles having the same rigid body number (key). The rigid particles can be reduced by key applying this function, however, if the particles are not successively aligned, a problem occurs because they are recognized as different keys as shown in Figure 3.15. To resolve this problem, a sorting algorithm was applied before the reduction process. (Figure 3.16) So, the efficient

GPU parallelization on the rigid bodies without limitation of the number of bodies was established.

Figure 3.17 shows the comparison of computation speed for each algorithm. Algorithm 1-2 with shared memory shows the fastest computation speed, and in the sorting algorithm, a large number of rigid body simulations can be performed with a small speed degradation. Some GPU parallelization algorithms have been implemented in the code, and a flexible application is possible by using the appropriate algorithm depending on the simulation conditions.

3.5 Code V&V Simulations

For the verification and validation of the implemented collision model, the basic simulations of conservation (momentum, angular momentum, and kinetic energy) were performed. Also, simulations on the damping and friction force were carried out. Lastly, collisions of multi-rigid bodies including all phenomena were analyzed. All V&V simulations are summarized in Table 3.2

3.5.1 Conservation of Momentum & Angular Momentum

Since the collision between rigid bodies is an interactive force that is exchanged with each other, the force is identical in magnitude but opposite in direction due to the action and reaction. Therefore, the momentum and angular momentum must be conserved. The below equations show the momentum and angular momentum conservation in the collision between rigid body 1 and rigid body 2.

- ◆ Momentum conservation

$$m_1 \mathbf{u}_1 + m_2 \mathbf{u}_2 = m_1 \mathbf{u}'_1 + m_2 \mathbf{u}'_2$$

- ◆ Angular momentum conservation

$$\mathbf{L} = \mathbf{L}'$$

$$\mathbf{L} = (I_1 \boldsymbol{\omega}_1 + m_1 \mathbf{r}_1 \times \mathbf{u}_1) + (I_2 \boldsymbol{\omega}_2 + m_2 \mathbf{r}_2 \times \mathbf{u}_2)$$

$$\mathbf{L}' = (I_1 \boldsymbol{\omega}'_1 + m_1 \mathbf{r}_1 \times \mathbf{u}'_1) + (I_2 \boldsymbol{\omega}'_2 + m_2 \mathbf{r}_2 \times \mathbf{u}'_2)$$

First, analyses were performed on the collision between rigid bodies with the cube shape, and the results showed that the physical quantities (momentum, angular momentum) are well preserved. In addition, collision simulations on other shapes such as a sphere, cross, and ellipse were carried out and showed good results. (Figure 3.18)

3.5.2 Conservation of Kinetic Energy in Elastic Collision

If there is no dissipation term like damping or friction, the kinetic energy of the system must be conserved. The kinetic energy can be divided into translational energy and rotational energy.

- ◆ Kinetic energy

$$E_{kinetic} = E_{translation} + E_{rotation} = \frac{1}{2} m \mathbf{u}^2 + \frac{1}{2} I \boldsymbol{\omega}^2$$

- ◆ Energy conservation

$$E = E'$$

$$E = \left(\frac{1}{2} m_1 \mathbf{u}_1^2 + \frac{1}{2} I_1 \mathbf{w}_1^2 \right) + \left(\frac{1}{2} m_2 \mathbf{u}_2^2 + \frac{1}{2} I_2 \mathbf{w}_2^2 \right)$$

$$E' = \left(\frac{1}{2} m_1 \mathbf{u}'_1{}^2 + \frac{1}{2} I_1 \mathbf{w}'_1{}^2 \right) + \left(\frac{1}{2} m_2 \mathbf{u}'_2{}^2 + \frac{1}{2} I_2 \mathbf{w}'_2{}^2 \right)$$

In order to verify the energy conservation, the perfectly elastic collision simulations without the damping and friction ($e = 1, \mu = 0$) were performed, and the kinetic energy of the system is well conserved under 2% error.

3.5.3 Bouncing Block

In the normal contact force, the damping force is calculated based on the restitution coefficient (e) shown in Equation (3.49). The elastic collision analyzed above corresponds to the ideal condition where $e = 1$, and in general, the restitution coefficient has a value between $0 < e < 1$. The relative velocity before and after the collision can be expressed as follows by using the restitution coefficient according to Newton's law of impact.

$$e = -\frac{\mathbf{u}_{rel,after}}{\mathbf{u}_{rel,beforce}} = \frac{-(\mathbf{u}'_1 - \mathbf{u}'_2)}{\mathbf{u}_1 - \mathbf{u}_2} \quad (3.60)$$

In order to verify whether the implemented collision model is well simulated or not according to the restitution coefficient (e), 2D bouncing solid simulations were carried out depending on the restitution coefficient. The simulation conditions are summarized as follows.

◆ Density of the solid:	$\rho_s = 2,700 \text{ [kg/m}^3\text{]}$
◆ Initial falling height:	$H_0 = 0.5 \text{ [m]}$
◆ Solid geometry:	$D = 0.1 \times 0.1 \text{ [m}^2\text{]}$
◆ Initial particle spacing:	$\Delta x = 0.01 \text{ [m]}$ (100 particles)
◆ Restitution coefficient:	$e = 1.0, 0.8, 0.5 \text{ [-]}$
◆ Time-step:	$\Delta t = 1.0 \times 10^{-6} \text{ [sec]}$

As shown in Figure 3.19, simulations were performed for three conditions. ($e = 1.0, 0.8, 0.5$) For the ideal elastic condition ($e = 1.0$), the kinetic energy must be conserved as discussed in Section 3.5.2, and it can be verified that the velocity before and after the collision has the same magnitude and recovers to the initial falling height. Meanwhile, for the general condition ($e < 1.0$), kinetic energy dissipation occurs, and this magnitude can be determined by the damping term in Hertz's model. For the comparisons, the analytic solutions of the height and velocity at the time t can be derived as follows.

$$H = \mathbf{u}_0 t + 0.5 \mathbf{a} t^2 \quad (3.61)$$

$$\mathbf{u} = \mathbf{u}_0 + \mathbf{a} t \quad (3.62)$$

The simulation results show a good agreement with the analytic solution and showed that the implemented damping model of the normal contact force in this study is verified. (Figure 3.20-21)

3.5.4 Sliding Block on a Slope

From the previous verification simulations, the contact force in the normal direction was verified. Now, in order to verify the tangential contact force, a simple example was simulated. There is a box at rest on the ground, and the external force acts in the horizontal direction with $F_{ext} = f(time) = 98 * time [N]$. As shown in Figure 3.22, a solid box is subjected to gravity and the resulting normal force in the vertical direction, and the external force and the resulting friction force in the horizontal direction. Figure 3.23 shows the force and velocity in the normal direction the box receives. As the calculation starts and gravity acts, a slight overlap occurs with the ground. And the normal contact force is well calculated as $98 N$ which is the same magnitude with gravity force. Figure 3.24 shows the force and velocity in the tangential direction the box receives. The static frictional force on the box is $9.8 N$, which is the value of the normal contact force $98 N$ and the friction coefficient 0.1 . And the box doesn't move until the external force becomes larger than the static friction force. From about 0.1 second when the external force becomes $9.8 N$, the box starts to move by satisfying the condition of "external force $>$ frictional force". And it is verified that the simulation is in good agreement with the analytical solution.

Through the above analysis, it was confirmed that the tangential contact force used in this study is correctly applied, and then the simulations were performed on the sliding block on an inclined slope. The gravity force applied by the solid body with the degree θ can be represented in Figure 3.25. The solid body moves with the force in the tangential direction that are the tangential gravity force (F_t) and the

friction force which is the function of the normal force. The simulation conditions are as follows.

- ◆ Density of the solid: $\rho_s = 2,000 \text{ [kg/m}^3\text{]}$
- ◆ Solid geometry: $D = 1.0 \times 1.0 \text{ [m}^2\text{]}$
- ◆ Initial particle spacing: $\Delta x = 0.05 \text{ [m]}$ (400 particles)
- ◆ Slope degree: $\theta = 15, 30, 45 \text{ [}^\circ\text{]}$
- ◆ Friction coefficient: $\mu = 0.0, 0.2, 0.5 \text{ [-]}$
- ◆ Time-step: $\Delta t = 1.0 \times 10^{-6} \text{ [sec]}$

Through the forces acting on the rigid body, the analytic solution for the θ degree and the friction coefficient μ at the time t can be expressed as follows.

$$x = 0.5[g(\sin\theta - \mu\cos\theta)\cos\theta]t^2 \quad (3.63)$$

$$y = 0.5[g(\sin\theta - \mu\cos\theta)\sin\theta]t^2 \quad (3.64)$$

Figure 3.26-3.27 show the comparisons of the simulation results according to the friction coefficient and the slope degree with the analytic solution. The simulation results show a good agreement with the analytic solution and showed that the implemented friction model of the tangential contact force in this study is verified.

3.5.5 Collapse of Stacked Multi-body

Through the verification simulations performed previously, the implemented contact force including elastic force, damping force, and friction force showed a good agreement with analytical solutions in the collision between single solid bodies. For a more complicated collision analysis, the multi-rigid body simulations including all physics were carried out and compared with the experimental data.

Zhang (2009) conducted experiments on the behavior of stacked multi-cylinder. The initial cylinders in the acrylic resin tank are stacked in 6 layers, and when the plate is open cylinders collapse by the gravity-driven force and the solid cylinders move with collision each other. The particle-based solid body consists of about 500 rigid particles in this study. Poisson ratio of the aluminum cylinder and acrylic resin tank is used as 0.3, and shear modulus is used as 25.5 *GPa* and 1.15 *GPa*, respectively. Since information on the friction coefficient was not given in the experimental conditions, parametric studies were performed to adopt an appropriate friction coefficient, and it was determined to be 0.1 in this simulation. And to prevent non-physical motion of the solid cylinders the damping coefficient was set to be 0.2. The simulation conditions are as follows.

- ◆ Density of the cylinder: $\rho_s = 2,700 \text{ [kg/m}^3\text{]}$
- ◆ Cylinder geometry: $D = 1.0 \text{ [cm]}$, $h = 9.9 \text{ [cm]}$
- ◆ Acryl tank geometry: $L \times D \times H = 26 \times 10 \times 26 \text{ [cm}^3\text{]}$
- ◆ Initial particle spacing: $\Delta x = 0.04 \text{ [cm]}$ (493 particles per solid)
- ◆ Time-step: $\Delta t = 1.0 \times 10^{-6} \text{ [sec]}$

Figure 3.28 shows the comparison of the rigid body motion over time with the experimental data and good agreement. When the plate is opened, the rigid bodies collapse due to the gravitational force and move forward. As the slope is formed, the solid in the front part slides and rolls alone, and some solids follow it. The series of processes shows almost the same trend as in the experiment and is well predicted by the contact force calculation method implemented in this study.

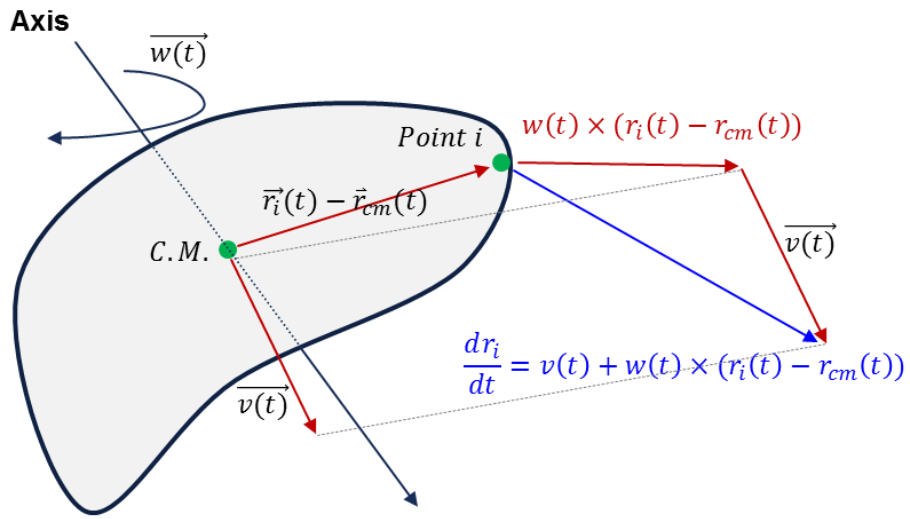


Figure 3.1 Motion of rigid body

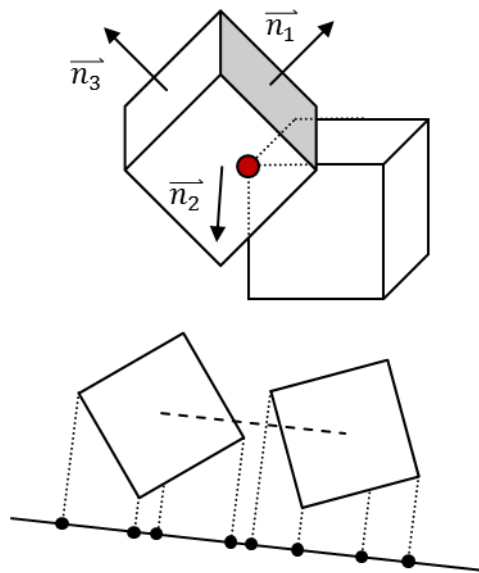


Figure 3.2 Grid-based contact detection

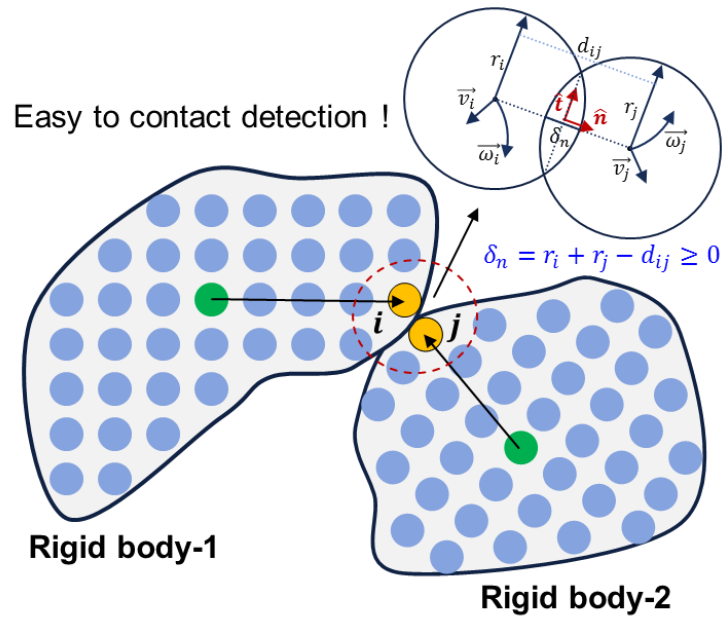


Figure 3.3 Particle-based contact detection

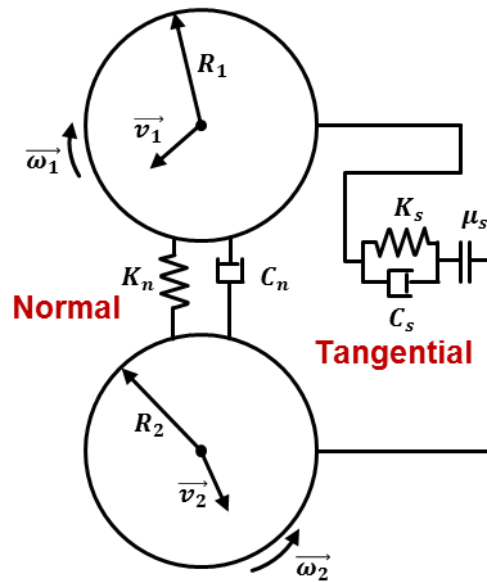


Figure 3.4 The concept of spring-dashpot model

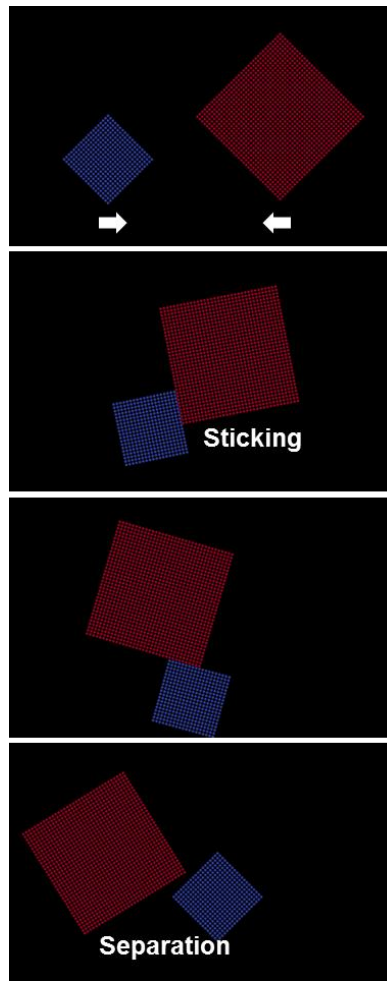


Figure 3.5 Sticking collision in IBF model

Table 3.1 Comparison of collision results

			1. MBF	2. Plastic	3. IBF	4. Penalty-based
Before collision	Linear momentum	x	-273.40			
		y	0			
	Angular momentum (Rigid A & B)		-604.31 + 1569.96 = 965.65			
	Energy (Translation & Rotation)		407.45 + 135.78 = 543.23			
After collision	Linear momentum	x	-273.40	-273.40	-273.40	-273.40
		y	0	0	0	0
	Angular momentum		964.48	965.65	965.64	965.65
	Energy (Translation & Rotation)		203.28 (62%)	334.29 (38%)	545.89 (0.5%)	538.30 (0.9%)

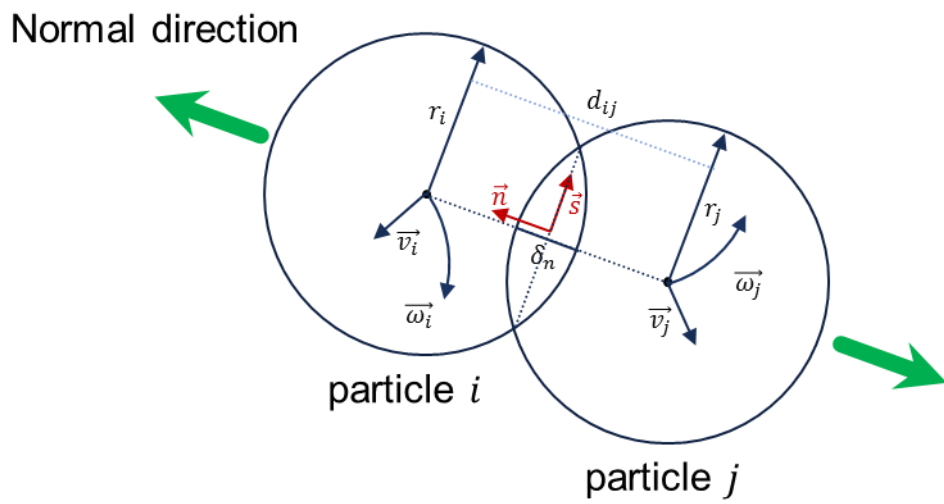


Figure 3.6 Single particle collision (DEM)

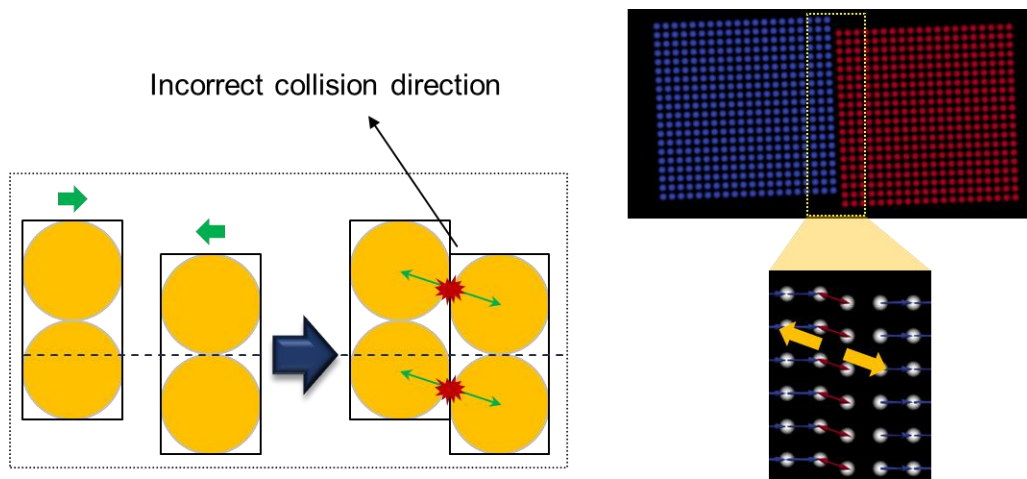


Figure 3.7 Incorrect calculation in particle-based rigid body collision

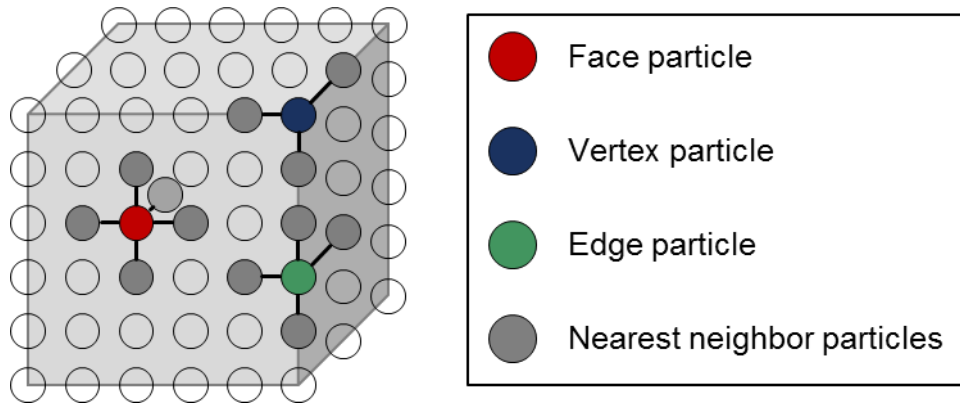


Figure 3.8 Rigid particle type in cubic geometry

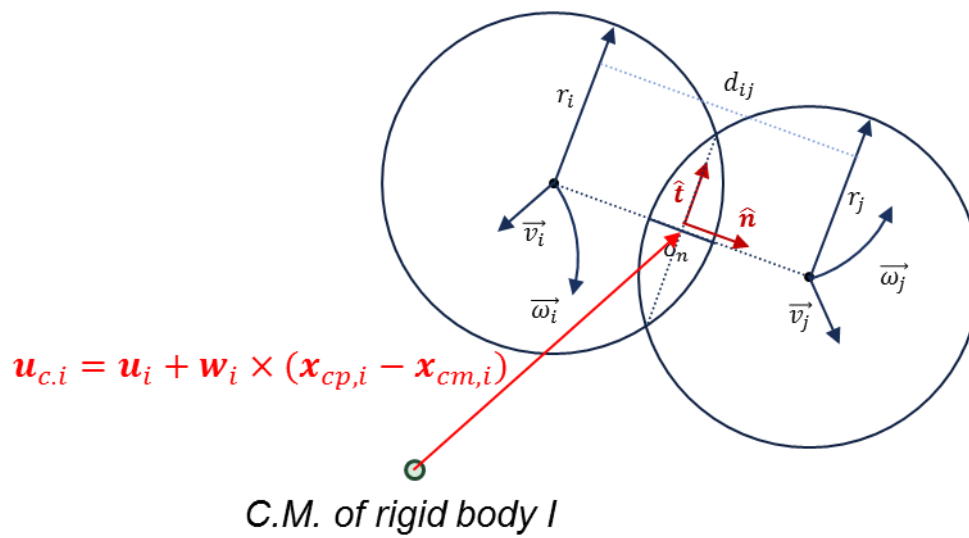


Figure 3.9 Velocity vector at contact point

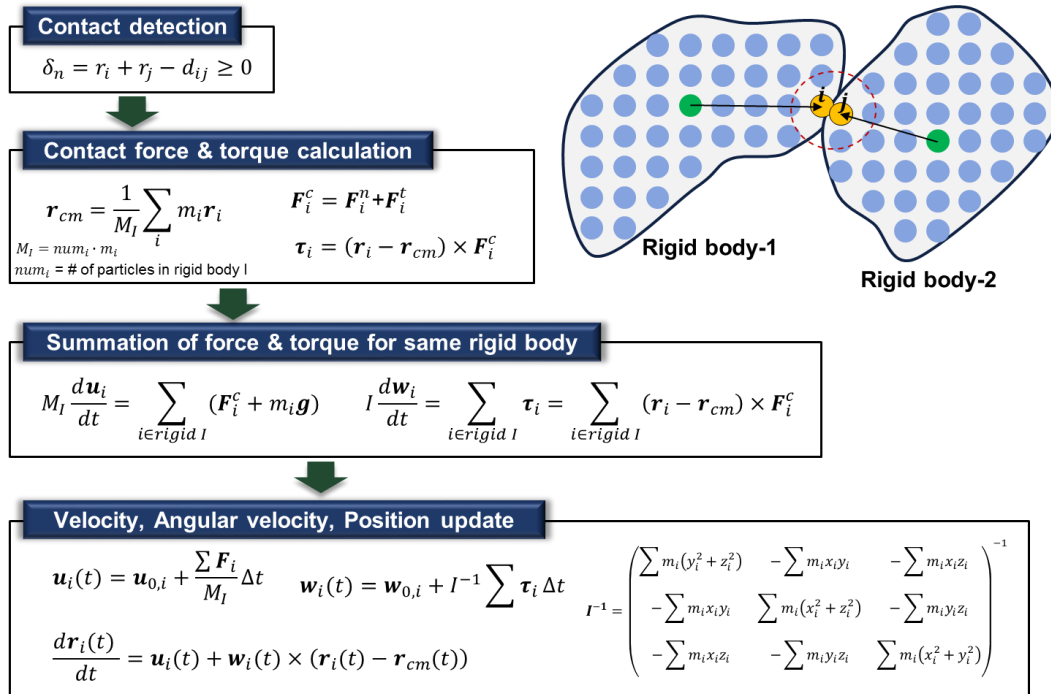


Figure 3.10 Algorithm of rigid body motion

Step	Example	Step	Example
Thread-1 read x	Read x=7	Thread-1 read x	Read x=7
Thread-1 calculate +1	8	Thread-2 read x	Read x=7
Thread-1 return x	x=8	Thread-1 calculate +1	8
Thread-2 read x	Read x=8	Thread-2 calculate +1	8
Thread-2 calculate +1	9	Thread-1 return x	x=8
Thread-2 return x	x=9	Thread-2 return x	x=8

Figure 3.11 Memory racing condition

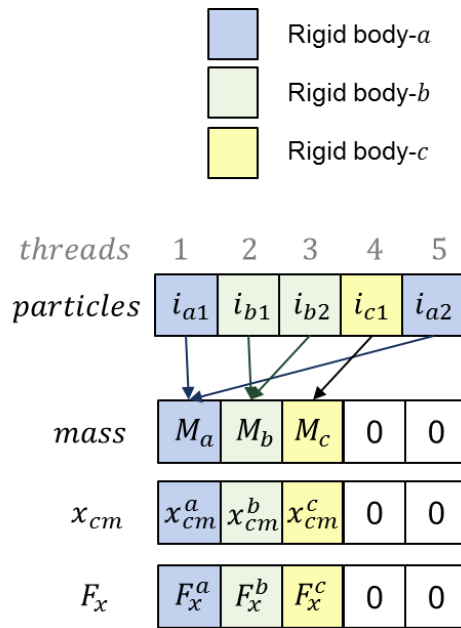


Figure 3.12 AtomicAdd operation

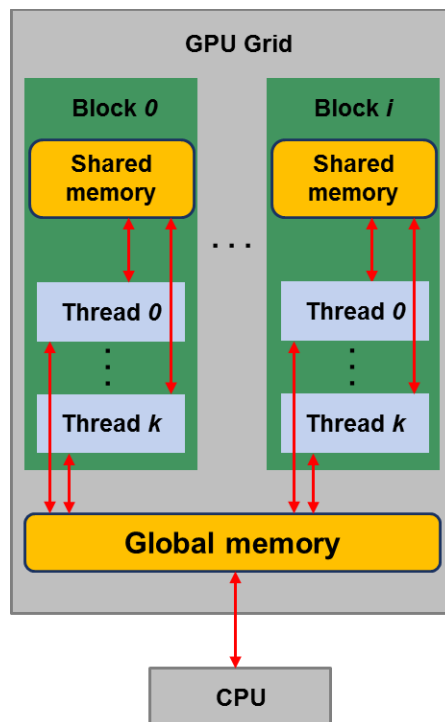


Figure 3.13 CUDA memory structure

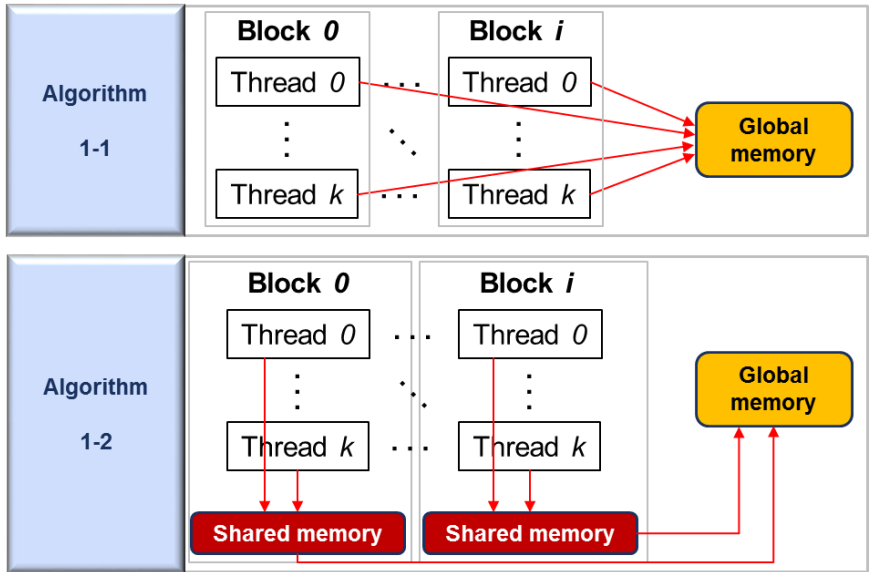


Figure 3.14 GPU parallelization algorithms

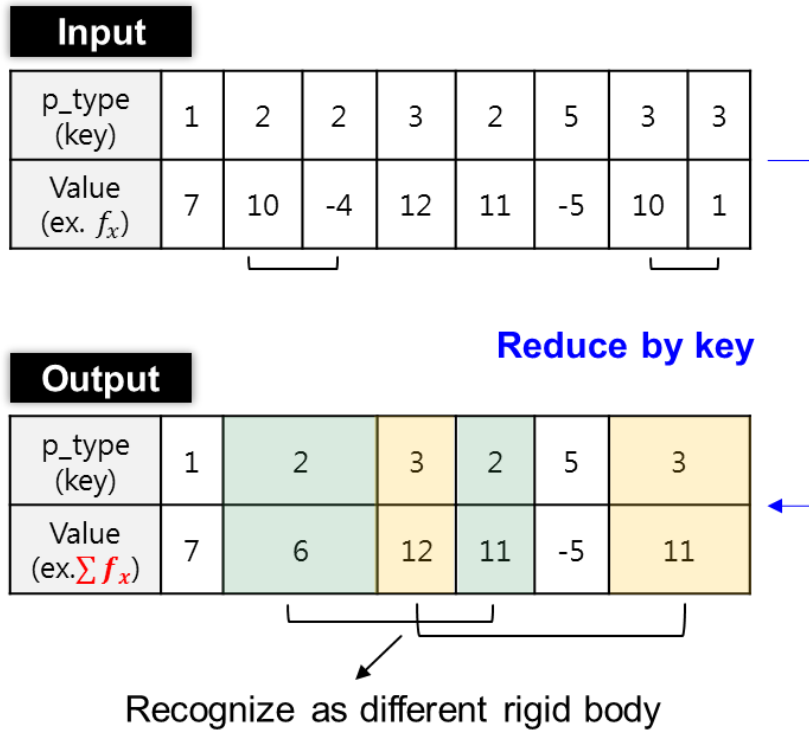


Figure 3.15 Reduction process without sorting

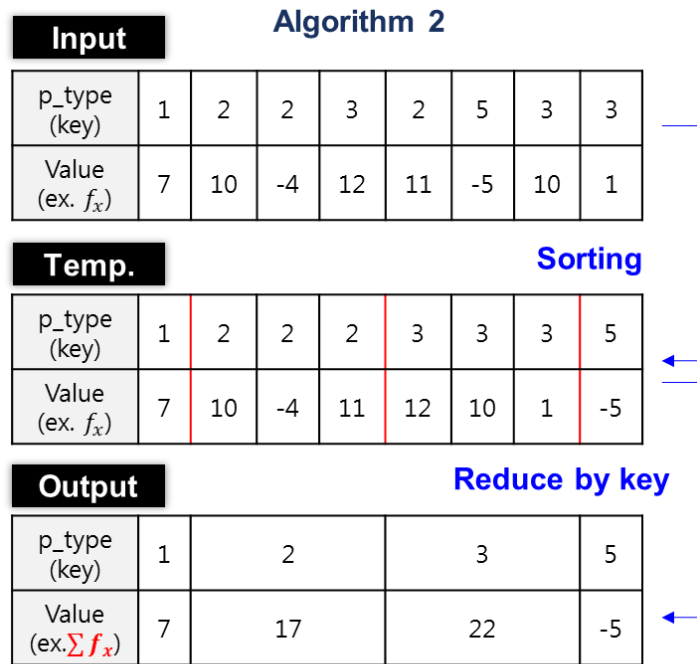


Figure 3.16 Reduction process with sorting

Table 3.2 V&V simulations for solid-solid interactions

V&V Cases	
Single-Rigid Body	
Normal/Tangential Elastic Force	Elastic Collision Simulation (2D/3D)
	<ul style="list-style-type: none"> ✓ Momentum Conservation ✓ Angular Momentum Conservation ✓ Energy Conservation
Normal Damping Force	Bounce Simulation (2D)
	<ul style="list-style-type: none"> ✓ Restitution coefficient ($e = 1.0, 0.8, 0.5$)
Tangential Friction Force	Slope Simulation (2D)
	<ul style="list-style-type: none"> ✓ Friction coefficient ($\mu = 0.0, 0.2, 0.5$) ✓ Slope angle ($\theta = 15^\circ, 30^\circ, 45^\circ$)
Multi-Rigid Body	
Normal/Tangential All physics	Stacked Multi-Body Simulation (2D)
	<ul style="list-style-type: none"> ✓ All included (Elastic, Damping, Friction)

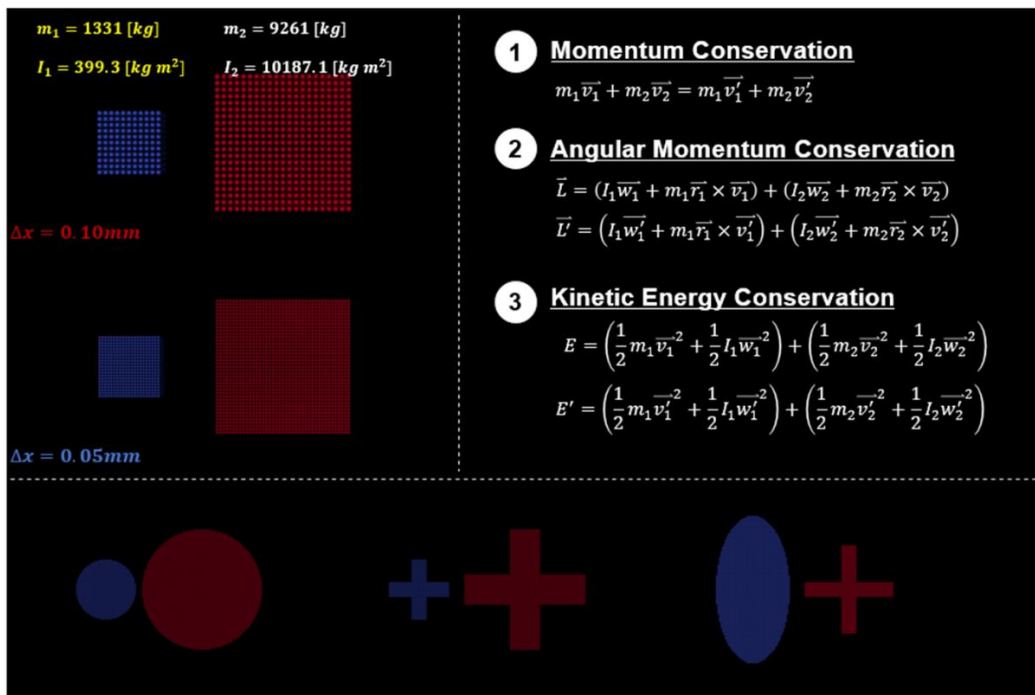
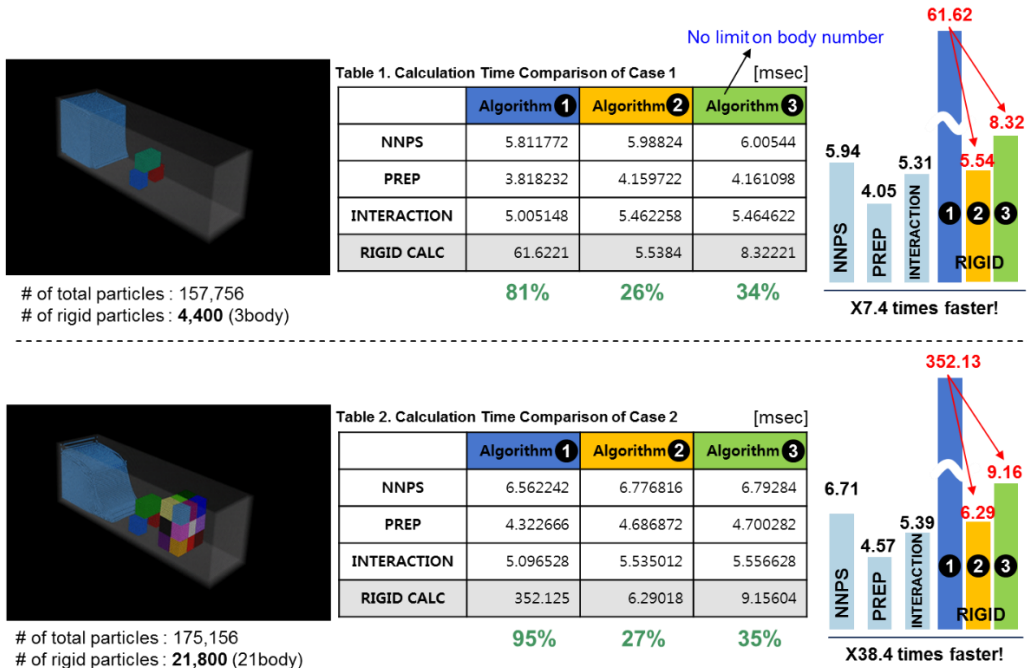


Figure 3.18 Conservation of momentums and energy for several shapes

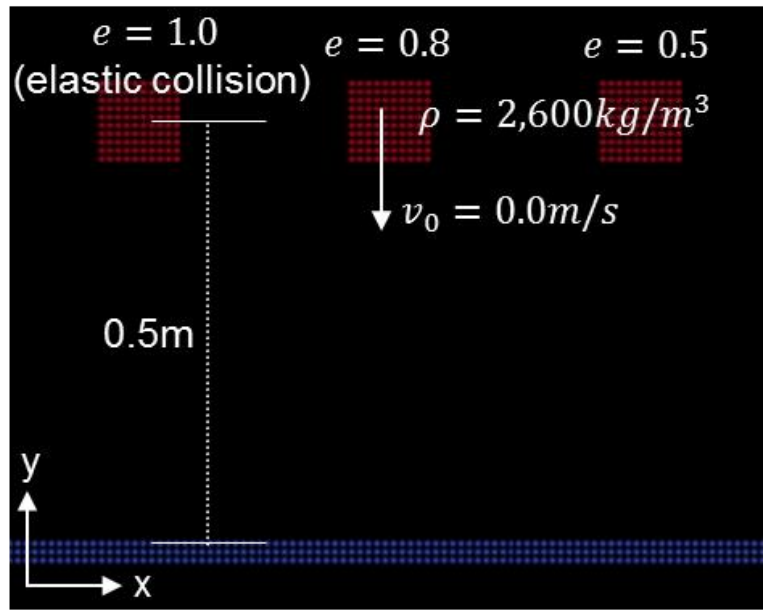


Figure 3.19 2D bouncing simulations for restitution coefficient

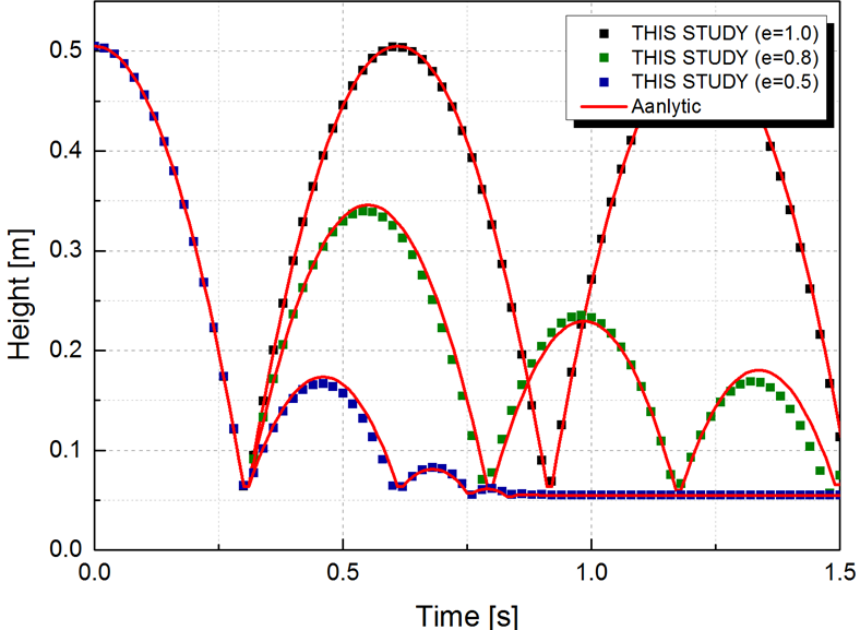


Figure 3.20 Height of bouncing solid with analytic solution

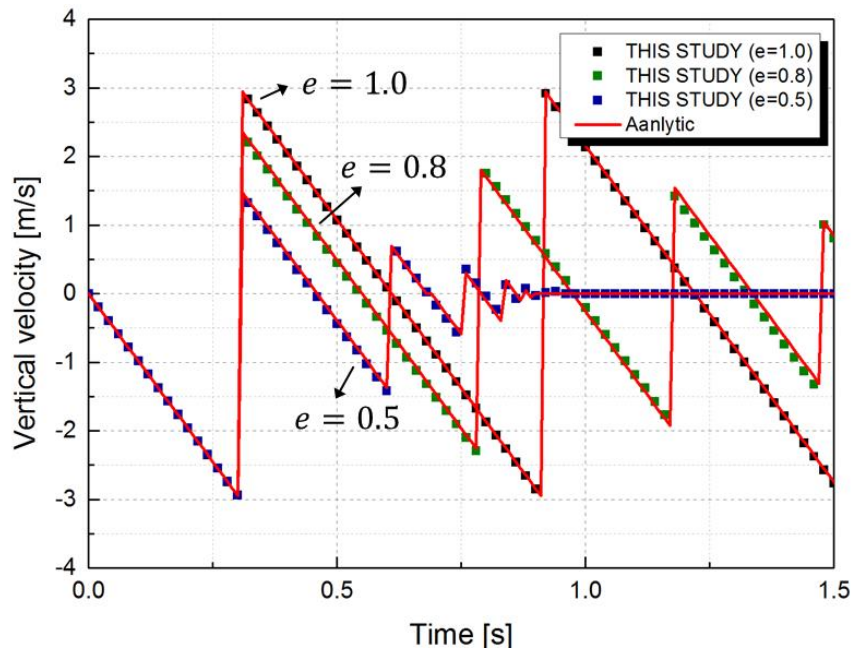


Figure 3.21 Vertical velocity of bouncing solid with analytic solution

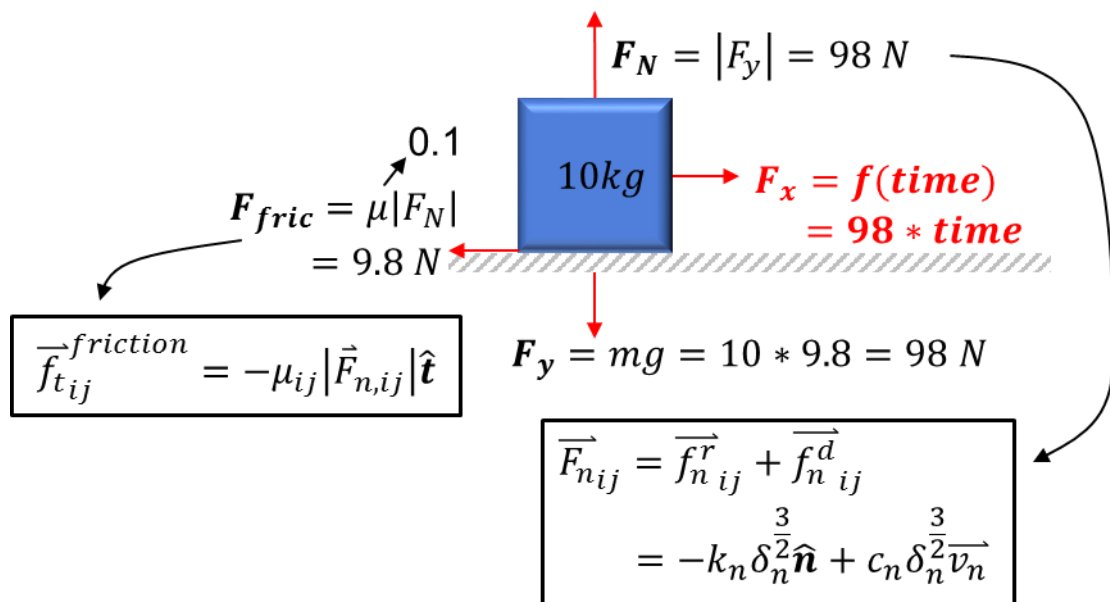


Figure 3.22 Forces acting on the box

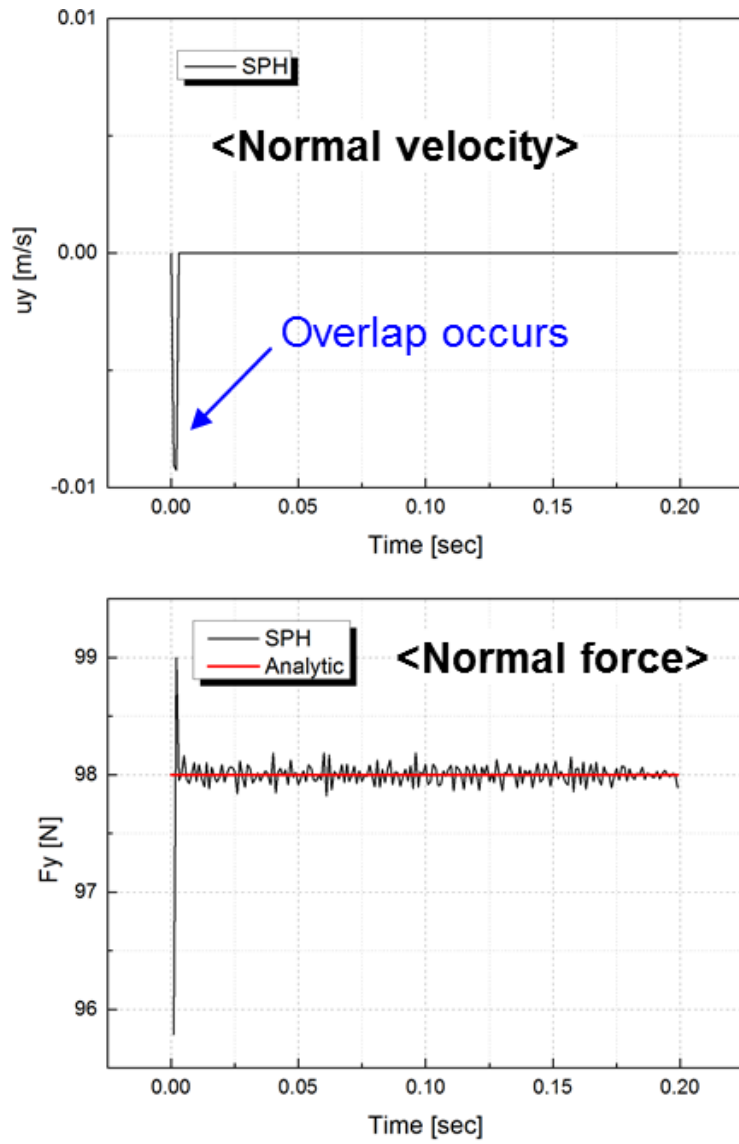


Figure 3.23 Simulation results in normal direction of the box

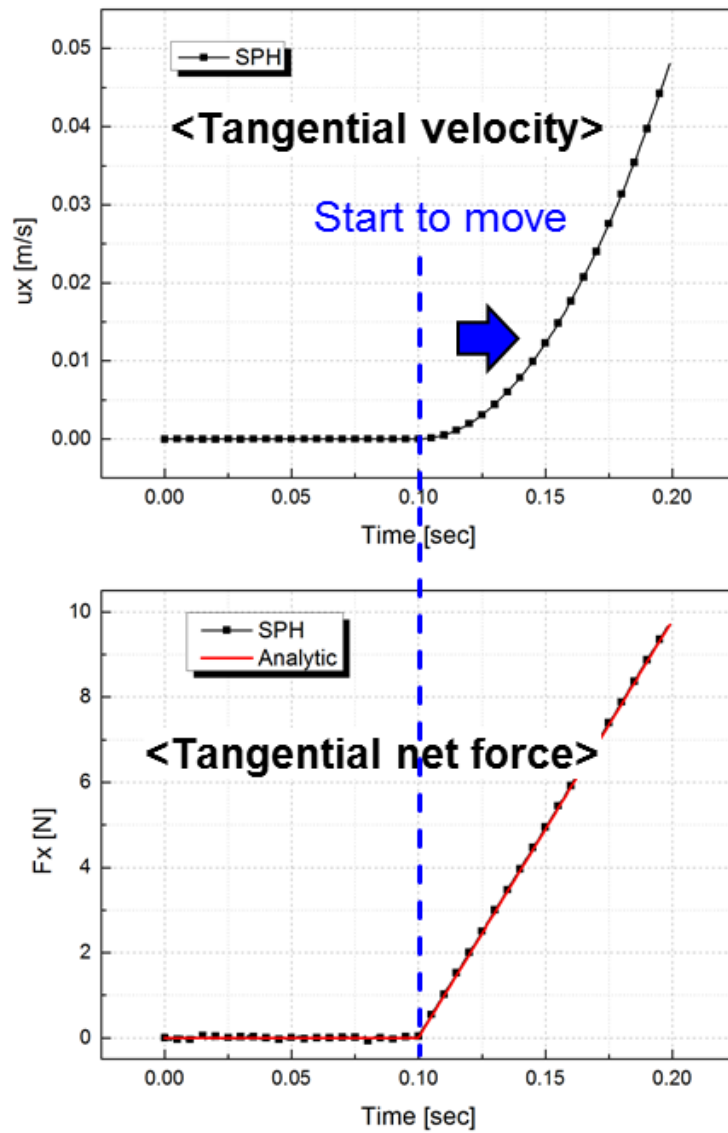


Figure 3.24 Simulation results in tangential direction of the box

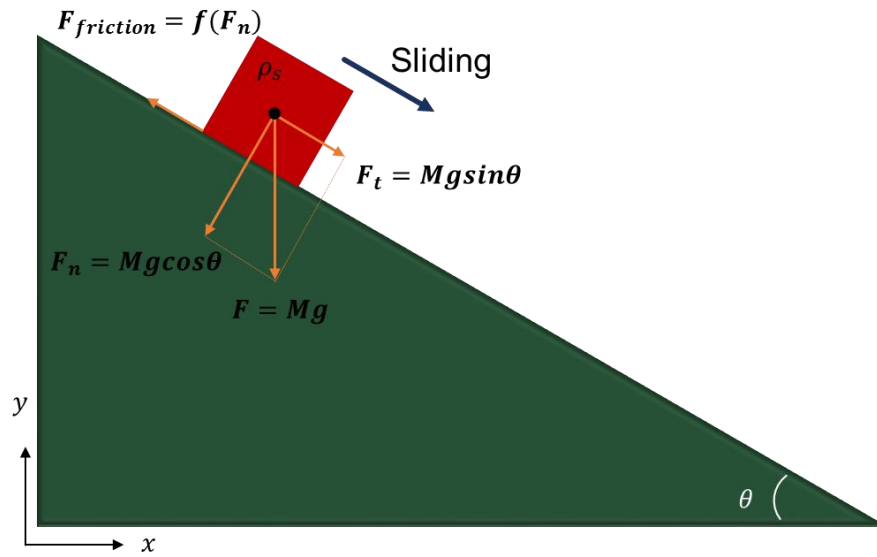


Figure 3.25 Forces applied on the solid body

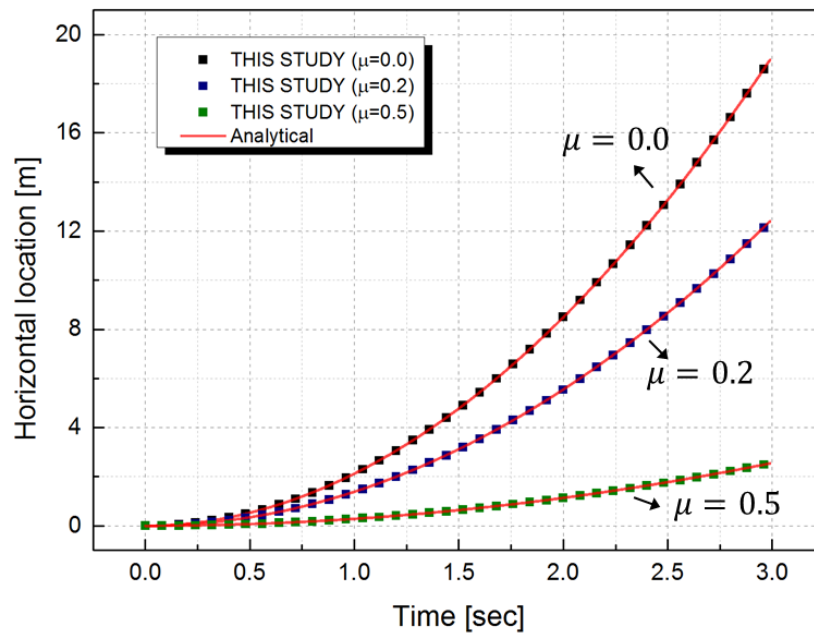


Figure 3.26 Horizontal location according to the friction coefficient

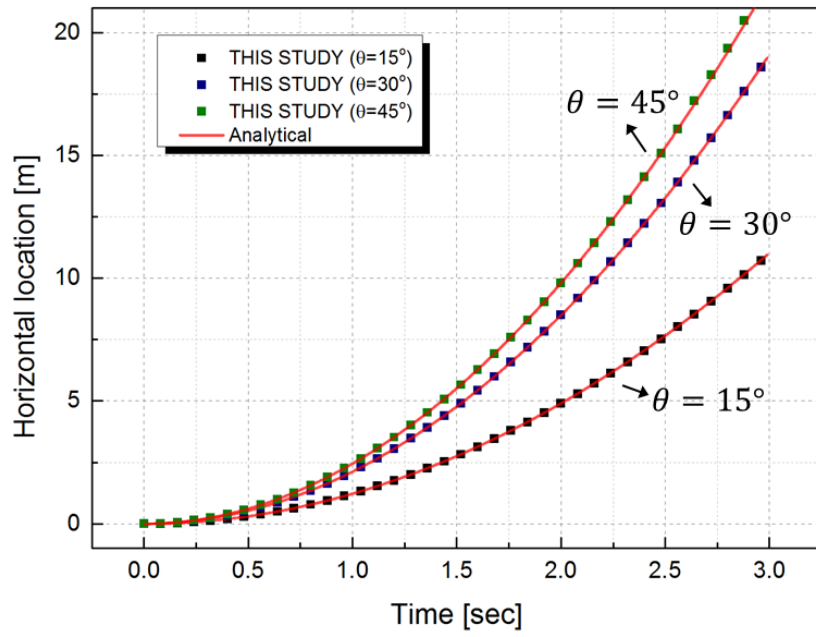


Figure 3.27 Horizontal location according to the slope degree

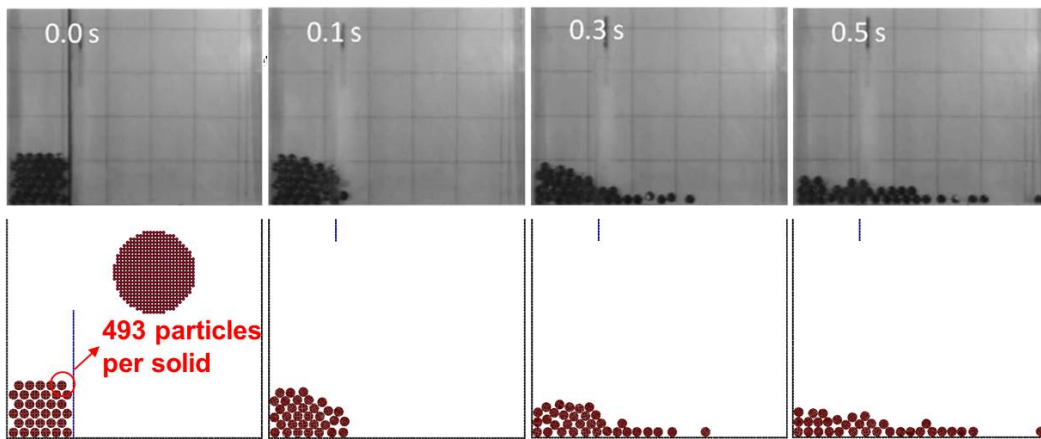


Figure 3.28 Snapshots of rigid body motion comparison

Chapter 4

Two-way Coupling of SPH-RBD

4.1 Resolved Approach

For the coupling of rigid body dynamics with the SPH method, the resolved approach was adopted in this study. In the resolved approach, the phases of the fluid and solid are completely separated from each other, which has a clear boundary domain in the simulation. In addition, since the interactions between fluids and rigid bodies are analyzed based on the 1st principle, there is no need for an empirical correlation depending on the solid shape. So, the analysis can be performed regardless of the shape or size of the solid bodies. Therefore, the hydrodynamic interactions between non-spherical solids and fluids can be easily analyzed regardless of the solid geometry. In this study, the basic SPH governing equations mentioned in Section 2 have been used for the interaction between fluid and rigid particles.

4.2 Governing Equations

4.2.1 Solid Phase

To estimate the hydraulic forces between fluids and solids exactly, it is most

important to calculate the pressure gradient term in the momentum conservation equation. Firstly, an accurate pressure estimation of fluid and solid is necessary. Then, the pressure force between particles is calculated based on the pressure gradient. In this study, for the pressure estimation of the rigid body particles, the method proposed by Adami (2012) has been adopted as follows.

The force balance equation on the rigid body surface can be established in order to accurately approximate the pressure gradient of the fluid particles around the rigid particle.

$$\frac{d\mathbf{u}_f}{dt} = -\frac{\nabla P_f}{\rho_f} + \mathbf{g} = \mathbf{a}_s \quad (4.1)$$

where the subscript f, s means fluid particle and rigid particle. The position vector $d\mathbf{l}$ between the rigid particle and fluid particle can be expressed in the form of an integral as follows, and the pressure of the rigid particles can be estimated from the pressure of the neighboring fluid particles.

$$\int \nabla P_f \cdot d\mathbf{l} = \rho_f \int (\mathbf{g} - \mathbf{a}_s) \cdot d\mathbf{l} \quad (4.2)$$

$$P_s = P_f + \rho_f (\mathbf{g} - \mathbf{a}_s) \cdot \mathbf{r}_{sf} \quad (4.3)$$

Since several fluid particles around the rigid particle are involved in the property calculation, the pressure on the rigid body surface can be derived through the following SPH summation form.

$$P_s = \frac{\sum_f P_f W_{sf} + (\mathbf{g} - \mathbf{a}_s) \cdot \sum_f \rho_f \mathbf{r}_{sf} W_{sf}}{\sum_f W_{sf}} \quad (4.4)$$

Then, the pressure force can be calculated based on the pressure gradient of particles as follows.

$$\mathbf{F}_{f \rightarrow s}^p = -m_s m_f \left(\frac{P_s + P_f}{\rho_s \rho_f} \right) \nabla W_{fs} \quad (4.5)$$

The net force exerted on a rigid body can be expressed as the sum of the pressure force by the fluid and the contact force between the rigid bodies discussed in the previous chapter.

$$\mathbf{F}_s = M_s \frac{d\mathbf{u}_s}{dt} = \sum_{i=1}^{N_s} (\mathbf{F}_{s \rightarrow s}^c + m_s \mathbf{g}) + \sum_{i=1}^{N_s} \left(\sum_{j=1}^{N_f} \mathbf{F}_{f \rightarrow s}^p \right) \quad (4.6)$$

$$I \frac{d\mathbf{w}_s}{dt} = \sum_{i=1}^{N_s} \boldsymbol{\tau}_i = \sum_{i=1}^{N_s} (\mathbf{r}_i - \mathbf{r}_{cm}) \times \mathbf{F}_s \quad (4.7)$$

N_s and N_f mean the number of rigid particles and fluid particles within the searching range.

4.2.2 Fluid Phase

Just as a rigid particle is received the hydraulic force by a fluid particle, the fluid particle must also be subjected to the force with the same magnitude by action-reaction. Therefore, the pressure force that the fluid particle received from the rigid particles can be calculated through the following equation, which has the same magnitudes but opposite in direction as Equation (4.5).

$$\mathbf{F}_{s \rightarrow f}^p = -m_f m_s \left(\frac{P_f + P_s}{\rho_f \rho_s} \right) \nabla W_{sf} \quad (4.8)$$

The net force of the fluid particle can be expressed as follows by summing all the hydraulic forces received by the fluid particles and rigid body particles.

$$\mathbf{F}_f = m_f \frac{d\mathbf{u}_f}{dt} = \sum_{f=1}^{neighbor} \mathbf{F}_{f \rightarrow f}^{all} + \sum_{s=1}^{neighbor} \mathbf{F}_{s \rightarrow f}^p \quad (4.9)$$

4.3 Algorithm of SPH-RBD Code

A particle-based rigid body model is applied with the basic SPH code algorithm in this study, and the calculations for fluid particles and rigid particles are performed together. However, since the pressure of rigid particles is estimated from the pressure of the fluid particles as mentioned in the previous section, the pressure calculation part of the rigid body particles is located after pressure estimation of

fluid particles. Therefore, the overall calculation process does not depart from the original one even though there are some calculations on the rigid body particles. The computational algorithm for SPH-RBD code is as follows. The initial calculation algorithm part is the same as the original SPH code, and the pressure calculation of rigid particles is performed after calculating the fluid particles. Then, calculation of the hydrodynamic interaction between fluid particles and rigid particles is carried out and contact forces between rigid bodies are added to the interaction calculation part. The motion of the rigid body is updated by summing all values of the particles constituting the rigid body, and the time integration is performed. Figure 4.1 shows the simplified algorithm of the SPH-RBD code.

In general, there are several basic criteria that should be applied in the SPH analysis. The first is Courant-Friedrichs-Lewy (CFL) criterion required for explicit time integration for numerical stability. CFL criterion can be expressed as the speed of sound (c), which is about 10 times of the maximum speed expected in the simulation as mentioned in Section 2.1 and smoothing length (h) proportional to particle resolution.

$$\Delta t_{CFL} = \min\left(\frac{h}{c}\right) \quad (4.10)$$

Also, the other time step criterion was proposed by Monaghan (1989) and expressed as the magnitude of the acceleration received by the SPH particles (f).

$$\Delta t_f = \min\left(\sqrt{\frac{h}{|f|}}\right) \quad (4.11)$$

Morris et al. (1997) proposed the time-step criterion considering the viscous diffusion as follows.

$$\Delta t_v = \min\left(0.125 \frac{h^2}{\nu}\right) \quad (4.12)$$

where ν is the kinetic viscosity. Therefore, the SPH simulation should be performed by setting the smallest time-step among the above three criteria.

$$\Delta t_{SPH} = \min(\Delta t_{CFL}, \Delta t_f, \Delta t_v) \quad (4.13)$$

In the case of rigid particles, the DEM time-step criterion is applied in the simulation and expressed as the mass (m) and the spring coefficient of rigid particles (k_n). (Lemieux et al., 2008)

$$\Delta t_{DEM} = \min\left(\frac{\pi}{50} \sqrt{\frac{m}{k_n}}\right) \quad (4.14)$$

Therefore, when analyzing SPH fluid particles with rigid body particles together, the simulation should be performed using the minimum time-step for numerical stability and reliable results.

$$\Delta t = \min(\Delta t_{SPH}, \Delta t_{DEM}) \quad (4.15)$$

In the rigid body collision analysis, it was confirmed that the simulation results

converge as the time-step became smaller, and it was judged to be reliable at the time-step under $2e^{-6}$. Therefore, since the DEM time-step is comparable or smaller than the SPH time-step in this study, the simulations were performed in the order of $1e^{-6}$ time-step.

4.4 Code V&V Simulations

For the verification and validation of the fluid-rigid coupling model, the basic hydrodynamic simulations between fluid and single rigid body were performed. For the more complicated condition, the simulations that include the interaction with fluid particles and multi rigid bodies were also carried out. All V&V simulations are summarized in Table 4.1.

4.4.1 Karman Vortex Problem

(i) Flow around single cylinder

In order to verify whether the previously applied pressure calculation at the solid boundary is well simulated or not, Karman vortex problems were simulated. In the Karman vortex, the drag/lift forces occur due to the hydrodynamic interaction between the solid and the fluid, and the vortex is created in the rear region of the solid. Figure 4.2 shows the simulation geometry for the Karman vortex problem. The tube is $L = 17D$, $H = 15D$ and the solid is located $5D$ away from the inlet with diameter $D = 0.1$ m. The simulation was performed in $Re = 100$ condition

with $\rho = 1000 \text{ kg/m}^3$, $\mu = 1.0 \text{ Pa}\cdot\text{s}$, and $u_{inlet} = 1.0 \text{ m/s}$. The open boundary condition is applied for continuous flow, and a no-slip condition near the solid boundary is applied. In addition, the continuity equation is used for mass conservation with δ – SPH, and a particle shifting technique is applied to prevent non-physical particle arrangement.

Figure 4.3 shows the relationship between Reynolds number versus drag coefficient for a circular cylinder. Drag coefficient, lift coefficient, and Strouhal number can be expressed as follows.

$$C_D = \frac{F_D}{0.5\rho U_\infty^2 D} \quad (4.16)$$

$$C_L = \frac{F_L}{0.5\rho U_\infty^2 D} \quad (4.17)$$

$$St = \frac{fD}{U_\infty} \quad (4.18)$$

The results of this study show 1.423 for drag coefficient and 0.348 for lift coefficient. (Figure 4.4) The drag coefficient consists of pressure drag and viscous drag, and the ratios are 77% and 23%, respectively. The simulation results in this study show good agreement, and the comparison with other researches on drag and lift coefficient is summarized in Table 4.2.

Next, the simulations were carried out for a square cylinder with a non-spherical shape. The simulation conditions are the same with the previous one, and the square cylinder has a length of D . Figure 4.5 shows the relationship between Reynolds

number and Strouhal number which characterizes the oscillation period of vortex shedding. The comparison of the simulation results is summarized in Table 4.3 for $Re = 100$ condition. The drag coefficient and Strouhal number in the square cylinder condition show a good agreement with other simulation results. Figure 4.6 shows the drag coefficient value in the low Reynolds number region, and also shows good agreement with other simulations. Figure 4.7 shows the vorticity of the circular and square cylinders.

(ii) Flow around multi cylinder

Vortex shedding simulations in multi-cylinder were also performed in order to confirm the effect of secondary flow motion where the flow field is affected by the solid boundary in front and the rear boundary is again influenced by this flow field. Case 1 is similar to the previous one, but the solid boundary is located at $10D$ instead of $5D$. In cases 2 and 3, cylinders are located in $5D$ and $10D$ with a fixed location in case 2, but the front solid oscillates up and down with a period of π in case 3. Figure 4.8 shows the vorticity, and Figure 4.9-4.10 shows the drag and lift coefficient for three cases, respectively. In case 1, the simulation results show almost the same as those of the previous one in vorticity and drag/lift coefficient. The slight differences are due to a small change in the flow velocity as the cylinder position is changed. In case 2, vortex shedding is formed due to the influence of the solid boundary located in the front, and the rear boundary is affected by this changed flow. The rear cylinder receives very little drag and lift force since the flow is restricted from the cylinder located in front. In case 3, it can be seen that the vortex shedding is formed by the movement of the cylinder with the period, and the

drag coefficient also has the same period. Because the flow is asymmetrically formed at the top and the bottom of the rear cylinder, a large lift force is calculated.

Through the conducted simulations, it can be shown that the solid-fluid hydrodynamic interactions of spherical as well as non-spherical shapes have good agreement with the previous studies. Also, it is confirmed that the pressure calculation method using the Neumann pressure boundary condition implemented in this study simulates the fluid-solid interaction well.

4.4.2 Water Entry

The water entry problem is a widely used example for analyzing the hydrodynamic interaction between fluid and solid, and the experimental and analytical studies on this are vary depending on the initial velocity of the wedge, weight, and angle, etc. In this study, the experiment of Zhao (1997) is adopted as reference data, and Figure 4.10 shows the geometry of the water entry simulation. The size of the water pool is $4 \times 1 \times 2 \text{ m}^3$ and the mass of the wedge is 241 kg and the wedge angle is 30° , and the initial velocity at the surface of the pool is 6.15 m/s . The total number of particles is 326,516 for 0.5 mm particle resolution, and the $1\text{e}^{-6} \text{ sec}$ time-step was used.

In order to exclude the effect on the 3D, Zhao's experiments were conducted on the unit length of 1 m . Therefore, for computational efficiency, the simulation performed in this study is carried out under 2-dimensional geometry that implies unit length in the y-direction. The SPH simulation result of vertical velocity change of the wedge is compared with the experimental data and another simulation result of Ren (2014), and shows a good agreement. (Figure 4.12)

4.4.3 Sinking & Rotating Body

Next, the V&V simulation was performed on the example in which the physical properties of solid and fluid are artificially set. The solid body located at the surface of the pool has a biased center of mass, and rotates and sinks into the tank over time. (Figure 4.13) The solid body is $1L \times 0.5L$ and L is 1 m . The center of mass is $(0.25, 3.0)$, and the total mass, the inertia of momentum is 1 kg and 0.083 kgm^2 , respectively. The fluid tank is $4L \times 5L$ and filled with up to $3L$. The density and kinematic viscosity of the fluid is 1 kg/m^3 and $0.002\text{ m}^2/\text{s}$, respectively. The artificial gravity acceleration is 1 m/s^2 in the simulation. This example is a hypothetical condition, and mutual verifications have been actively performed among various analysis methodologies. The biased center of mass causes the solid body to rotate as it sinks into the pool, which induces the horizontal motion of the solid body. The SPH simulations were performed for a particle resolution $L/\Delta x = 100$, and the results on the center of mass and the rotational angle are compared with other simulation results. Figure 4.14-4.16 represent the comparisons with other simulation results and show a good agreement with other methodologies.

4.4.4 Floating & Falling Body

The 3D simulations were carried out on the floating and falling experiment carried out by Wu (2014). In the floating case, the water pool is $150 \times 140 \times 140\text{ mm}^3$ and filled with water up to 52 mm . The initial solid body is fixed at the bottom and has a size of $48 \times 49 \times 24\text{ mm}^3$ and $\rho_s = 800.52\text{ kg/m}^3$. In this study, the particle resolutions and time-step interval is $\Delta x = 2\text{ mm}$, and $\Delta t =$

$5e^{-6}$ sec, respectively. Figure 4.17 shows the initial simulation setup. As shown in Figure 4.18, as the rigid body begins to move, it floats to the surface and vibrates. In an ideal circumstance, the theoretical period of vibration can be expressed as follows, and for the given condition, it has a 0.347 sec.

$$T = 2\pi \sqrt{\frac{L}{g} \cdot \frac{\rho_f}{\rho_s}} \quad (4.19)$$

where T denotes the period of vibration, and L, g mean the height of the solid body and gravitational acceleration. ρ_f, ρ_s is the density of fluid and solid body, respectively. The period of vibration of the solid body in the simulation is 0.376 sec similar to that of the experiment, 0.367 sec. In this study, the floating body simulation was performed without air particles since it is not a dynamic situation where the behavior of solid and fluid changes actively, which may be a factor that can induce a slight difference with the experiment.

Next, the falling solid simulation was conducted and compared with the experimental result. As shown in Figure 4.19, the geometry of the water pool is the same as the previous case and filled with water up to 131 mm, and the falling object has 20 mm length for each side with $\rho_s = 2120 \text{ kg/m}^3$. The solid body sinks without rotation and reaches the bottom at about 0.365 sec. Figure 4.20 is the result of the vertical location of the solid body and shows good agreement with the experimental data.

The validation on the interaction of fluid and a single rigid body was conducted through these simulations, and it shows good agreement with the experimental results. For this, good applicability of the resolved approach based on the first principle was confirmed.

4.4.5 Collapse of Stacked Multi-body with Fluid

In order to analyze the interactions of many rigid bodies with fluids, Zhang (2009)'s experiments were adopted as reference data. The experiments were conducted on the shape of the circular cylinder stacked from 6 layers to 12 layers (4 cases) with the initial water dam height of 12 cm. The acrylic resin tank with $26 \times 10 \times 26 \text{ cm}^3$ and the aluminum circular cylinders with 1.0 cm diameter, 9.9 cm length were used. The mixture of solids and fluid collapses as the moving plate is withdrawn upward with the velocity 2.0 m/s. Figure 4.21 shows a comparison of the experimental and analysis results with 6 layers and 12 layers. As shown in the figure, the behavior of the cylinders over time shows a similar tendency to that of the experiment. The piled cylinders are towed by the gravity-driven water collapse and dambreak proceeds. In the case of 6 layers (left side of Figure 4.21), it can be seen that the front and rear ends of the stacked cylinders are divided clearly, which is well observed in the experiment. Figure 4.22 shows a comparison of arrival time depending on the cylinder layers. The simulation results show good agreement with experimental data, and the error is acceptable since the comparison is on a very small time scale.

In the simulation geometry, the interface of the fluid highly changes according to the fluid motions, and the simulation results of single-phase and multi-phase can differ due to the existence of a lot of cavities. Figure 4.23 shows the comparisons between the single-phase simulation and the multi-phase simulation with air particles for the 6 layers condition. As seen in the figure, a free surface is formed around the rigid body as the water collapses at the beginning in the case of the single-phase simulation. In the SPH method, the properties of the interesting

particle are calculated based on the neighboring particles. So, if there are not enough neighboring particles, the SPH interpolation error may occur due to the lack of neighboring particles in the vicinity of the free surface in the single-phase simulation. On the other hand, in the multi-phase simulation, the calculation accuracy increases as air particles fill the free surface which reduces the interpolation error. In addition, the flow of fluid particles is locally restricted by the air particles, which also affects the rigid body behaviors. As can be seen in the single-phase simulation at 0.1 sec, there are a lot of empty spaces between the rigid bodies, whereas in the multi-phase simulation, it shows that the initial shape of the rigid bodies is well maintained similar to that of the experiment. The difference in the initial shape induces a larger difference over time. At 0.3 sec, the free surface of the fluid monotonically decreases in the simulation results, which matches well with the experiment. Also, at the rear end, the rigid cylinders are not disturbed and are well maintained. At the last simulation time (0.5 sec), the front and rear ends of the rigid bodies are clearly separated, and this tendency is well reproduced in the SPH simulations.

In this study, three-phase simulations were performed in two-dimensional geometry for computational efficiency in three-dimensional experiments. Although a good agreement is shown in comparison with the benchmark experiments, there can be errors that may occur due to discrepancy in dimensions. First, from the point of the solid view, it was confirmed that there is no large error caused by the discrepancies in dimensions through simple collision examples. From the fluid view, in addition, it can be seen that the difference in the dambreak results of the 2D and 3D is small by Jo et al. (2019) performed in this group. However, 2D is a perfectly ideal 3D geometry with unit length, which can induce local flow in the y-direction

in actual 3D simulation. As a result, some behaviors in the y-direction of the rigid body caused by the fluid motion may occur when analyzing solids and fluids together, which can have some effect on the simulation results. In addition, the benchmarking experiments were conducted using 9.9 *cm* circular cylinders in 10 *cm* water tank. So, the friction caused by the sidewall due to the y-direction motion can be one of the causes of errors, which is not considered in the 2-dimensional simulation. And uncertainties occurring in the experiment such as measurement errors can act as a potential error.

4.4.6 Code Application to Non-spherical Debris Sedimentation

When IVR (In-Vessel Retention) strategy fails during a severe accident in a nuclear reactor and the molten fuel is ejected out of the ex-vessel, the FCI phenomenon occurs under wet cavity conditions. The high momentum of the jet causes fragmentation of the molten fuel, and solid debris are generated due to heat transfer with the coolant. As the debris settle, a debris bed is formed on the concrete floor. And if the coolability of the bed is not sufficient, the next phase of the accident, MCCI, may occur. Therefore, the evaluation on the coolability of the debris bed is very important for reactor safety, and there are many factors that influence the coolability such as the shape and size of the solid debris, configuration of bed, internal flow path, and porosity, etc.

In this study, the simulations were carried out to confirm the applicability of the analysis system of hydrodynamic interactions between non-spherical solid debris and fluid to the debris sedimentation and debris bed formation. Since the previous experimental of non-spherical debris is limited in terms of debris shape and the

debris size is too small to simulate, it is difficult to perform the simulation using the existing experimental data in the currently set computational environment. So, the experimental apparatus on the non-spherical solid debris fragmentation is designed and constructed to get validation data.

(i) Experiment on non-spherical debris sedimentation

In order to perform the fragmentation simulations in the computing environment set in our group, an experimental apparatus as shown in Figure 4.24 was designed and constructed. The water tank made of transparent acrylic has the size of $200 \times 200 \times 700 \text{ mm}^3$, and a water drain port is installed at the bottom. The solid debris should be analytically representable and large enough to perform the simulations. Because the high resolution is required to exactly express curved solids such as a sphere, ellipse, etc., a rectangular-shaped solid fragment was used in this study to confirm the applicability of the developed code. One solid debris is $18 \times 18 \times 12 \text{ mm}^3$, and the experiments were carried out using solid column with $36 \times 36 \times 504 \text{ mm}^3$. The total number of solid debris is 168 ($3 \times 2 \times 28$) under this condition. (Figure 4.25) As the support plate open, the stacked solid debris fall into the water tank, and the process of fragmentation and sedimentation was observed over time and measured in the no-gas condition.

(ii) Simulation setup

Debris sedimentation simulations were performed under the same conditions with the experiments. The tank is filled with water at 38cm height initially, and

the density and dynamic viscosity of the water at room temperature is used as 1000 kg/m^3 and $0.001 \text{ Pa} \cdot \text{s}$, respectively. The solid debris with a density 1332.8 kg/m^3 begin to fall from 2 cm above the water surface. The shear modulus of the water tank and debris used in the simulations is 1.7 GPa and 0.03 GPa , respectively, and Poisson ratio of 0.3 is used for both materials. The friction coefficient and restitution coefficient was set as 0.5 and 0.8, respectively. The pre-determined resolution (particle spacing) is set to 3 mm identical to the fluid and solid, and the number of particles constituting one solid is 144. The total number of solid and fluid particles is about 25,000 and 570,103, respectively. A time-step of $2e^{-6} \text{ sec}$ was used for 1.5 second, and the simulations were performed in single-phase condition without gas.

(iii) Simulation results and discussion

Numerical simulations of non-spherical debris sedimentation were performed using the SPH-RBD coupled code developed in this study. Figure 4.26 shows a comparison of the experiment and simulation results of the sedimentation progress over time. As solid debris gets into the water pool initially, fragmentation begins due to the drag flow at the leading edge, and the solid column is fragmented into individual solids over time. The series of these processes were well reproduced in the SPH-RBD simulations, and it can be seen that the debris is deposited on the floor and a debris bed is formed eventually. Figure 4.27 shows the experiment and simulation results viewed from the top at 1.5 seconds. Since solid debris has a non-spherical shape, a debris bed can be possibly formed in an asymmetric shape rather than piled up one by one on the floor. [Cheng, 2017] Due to these characteristics of

the non-spherical debris shape, an internal flow path may be also developed inside the debris bed, which is a factor that can affect the coolability of the debris bed.

The experiments conducted in this study used a rubber mixture as solid debris for the ease and accessibility of the experiments and simulations. Since the rubber mixture has a small shear modulus value ($\sim 0.03 \text{ GPa}$), more overlap occurs in the simulations, and deformation may occur rather than the behaviors of a rigid body. Accordingly, the collision direction may differ depending on the degree of the overlap, which may lead to discrepancies in simulation results. In order to analyze these experimental conditions, the simulations were performed with a large restitution coefficient and friction coefficient, but there are still limitations. Adhesion between the fragments was also observed in the experiment when the fragments are wetted with water, which strongly affects the motion of debris. Therefore, it is necessary to use a solid body with some rigidity and to select a material with non-wettable surface properties for the accurate performance of experiments and simulations. Also, although the simulations were carried out under single-phase conditions, multi-phase simulations are needed to consider gas behaviors as shown in the experiment results. Due to the relatively large size of the solid used in this study, it is expected that the effect of the gas will not be large. However, consideration on the gas phase is necessary because the experimental phenomena are complicated and a large amount of gas is generated as shown in Figure 4.26.

Although there are some limitations in the experiment and simulations mentioned in the previous paragraph, it can be confirmed that the SPH-RBD coupled code developed in this study can be applied to the solid debris sedimentation in the nuclear reactor. For more accurate comparisons, it is necessary

to secure quantified solid debris whose characteristics don't change by conducting experiments. Also, quantified data is needed such as dispersion length, debris bed configuration and height, and internal flow path, etc. to validate simulation results with the experiment.

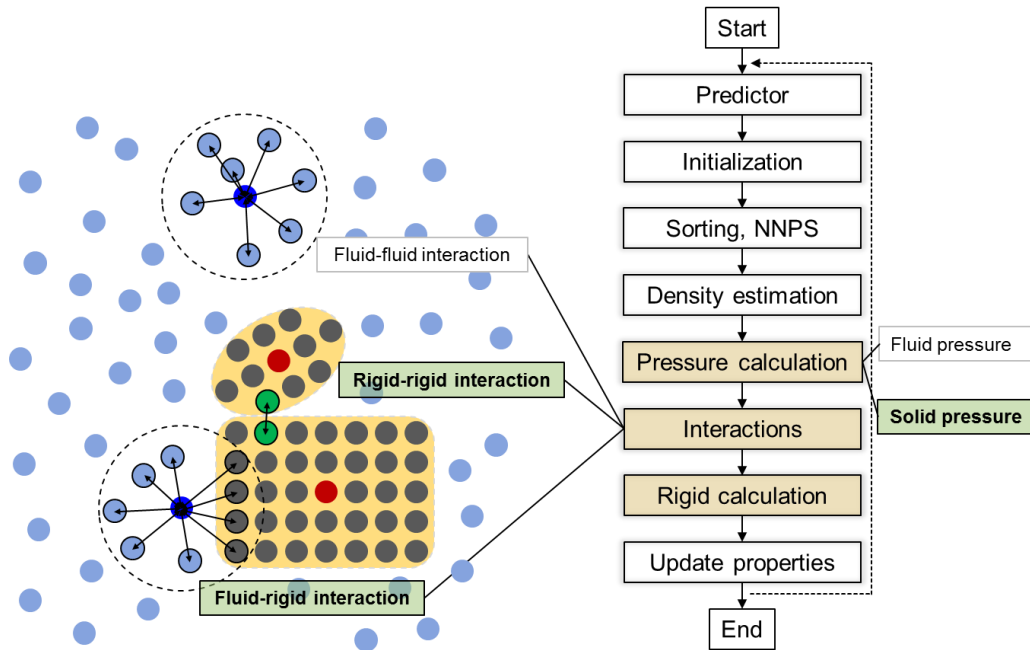


Figure 4.1 Simplified algorithm of SPH-RBD coupling code

Table 4.1 V&V simulations for fluid-solid interactions

V&V Cases	
Fluid & Single Rigid Body	
Hydrodynamic Interaction (Fluid-Solid)	Karman Vortex Problem (2D)
	✓ $F_{pres}(f \leftrightarrow s)$ (without translation, rotation)
	Water Entry Simulation (2D)
	✓ $F_{pres}(f \leftrightarrow s)$ (without rotation)
	Sinking & Rotating Body Simulation (2D)
✓ $F_{pres}(f \leftrightarrow s)$ (with rotation)	
	Floating & Falling Body Simulation (3D)
	✓ $F_{pres}(f \leftrightarrow s)$ (without rotation)
Fluid & Multi Rigid Bodies	
Hydrodynamic Interaction (Fluid-Solid) & Solid Collision (Solid-Solid)	Dambreak with Stacked Cube Simulation (3D)
	✓ All included ($F_{pres}(f \leftrightarrow s)$, $F_c(s \leftrightarrow s)$)
	Multi Body with Fluid Simulation (2D)
✓ All included ($F_{pres}(f \leftrightarrow s)$, $F_c(s \leftrightarrow s)$)	

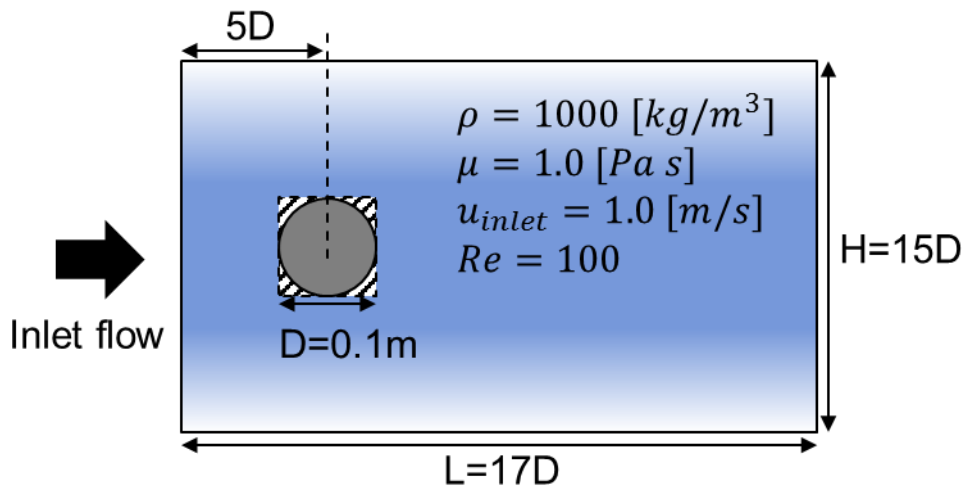


Figure 4.2 Geometry of Karman vortex simulation

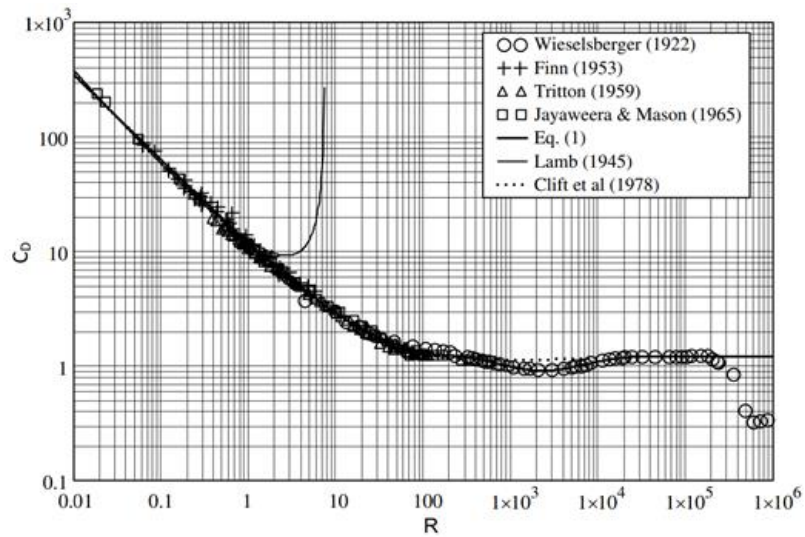


Figure 4.3 Drag coefficient versus Reynolds number (Cheng, 2013)

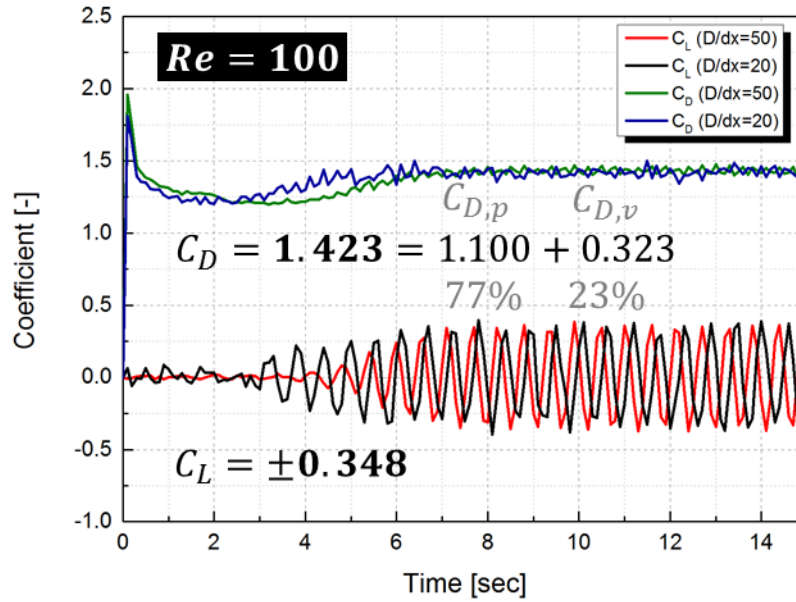


Figure 4.4 Simulation results of circular cylinder for Re=100

Table 4.2 Comparison of circular cylinder for Re=100

Re=100	Circular Cylinder		Method
	C_D	C_L	
This study	1.423 ± 0.021	0.348	SPH
Tafuni (2018)	1.474	0.322	SPH
Braza (1986)	1.364 ± 0.015	0.25	FVM
Ng (2009)	1.368 ± 0.016	0.360	FVM
Xu and Wang (2006)	1.423	0.34	FDM
Wang (2009)	1.379	0.357	FDM

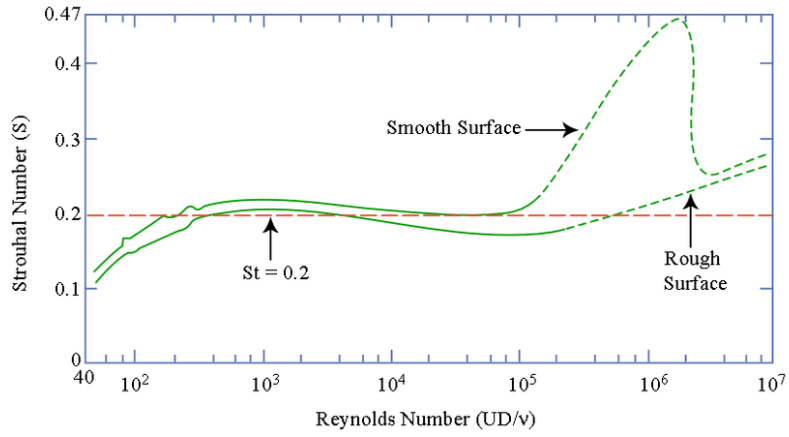


Figure 4.5 Strouhal number versus Reynolds number for square cylinder

Table 4.3 Comparison of square cylinder for Re=100

Re=100	Square Cylinder		Method
	Cd	St	
This study	1.504	0.154	SPH
Wang (1996)	1.52	0.15	FVM
Sohankar (1998)	1.478	0.146	FEM
Robichaux (1999)	1.53	0.154	FEM
Sen & Mittal (2011)	1.510	0.147	FEM
Li (2019)	1.438	0.1434	FVM

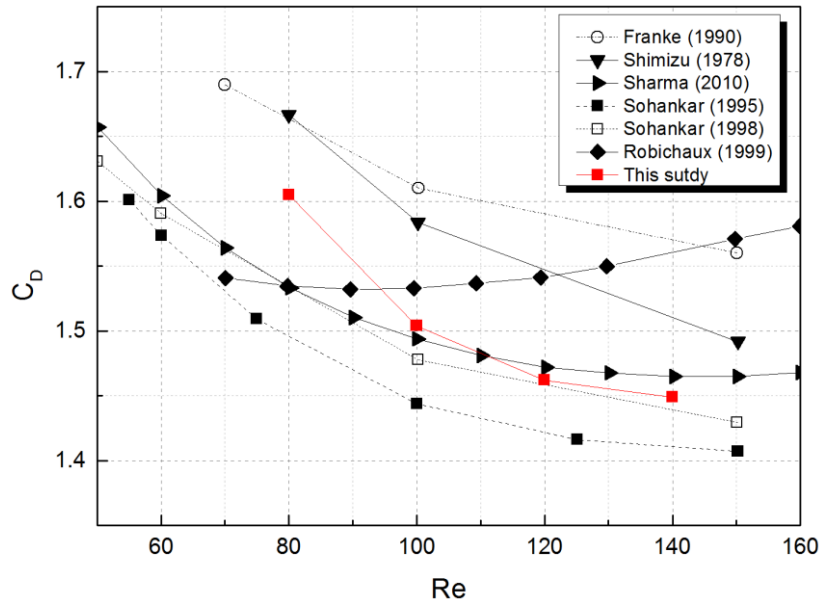


Figure 4.6 Drag coefficient of square cylinder in low Reynolds region

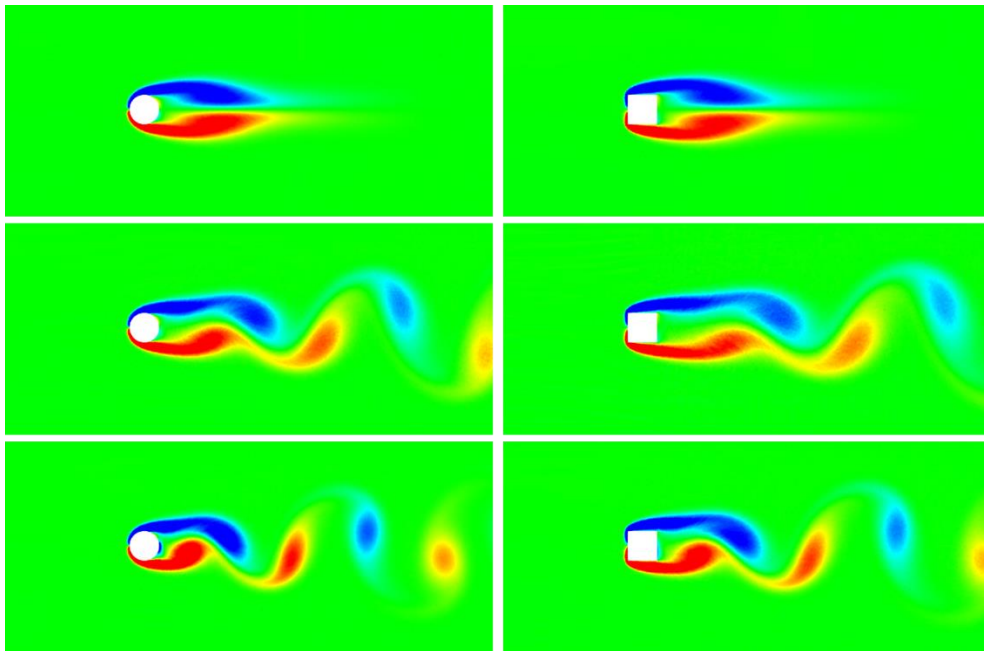


Figure 4.7 Vorticity of circular and square cylinder

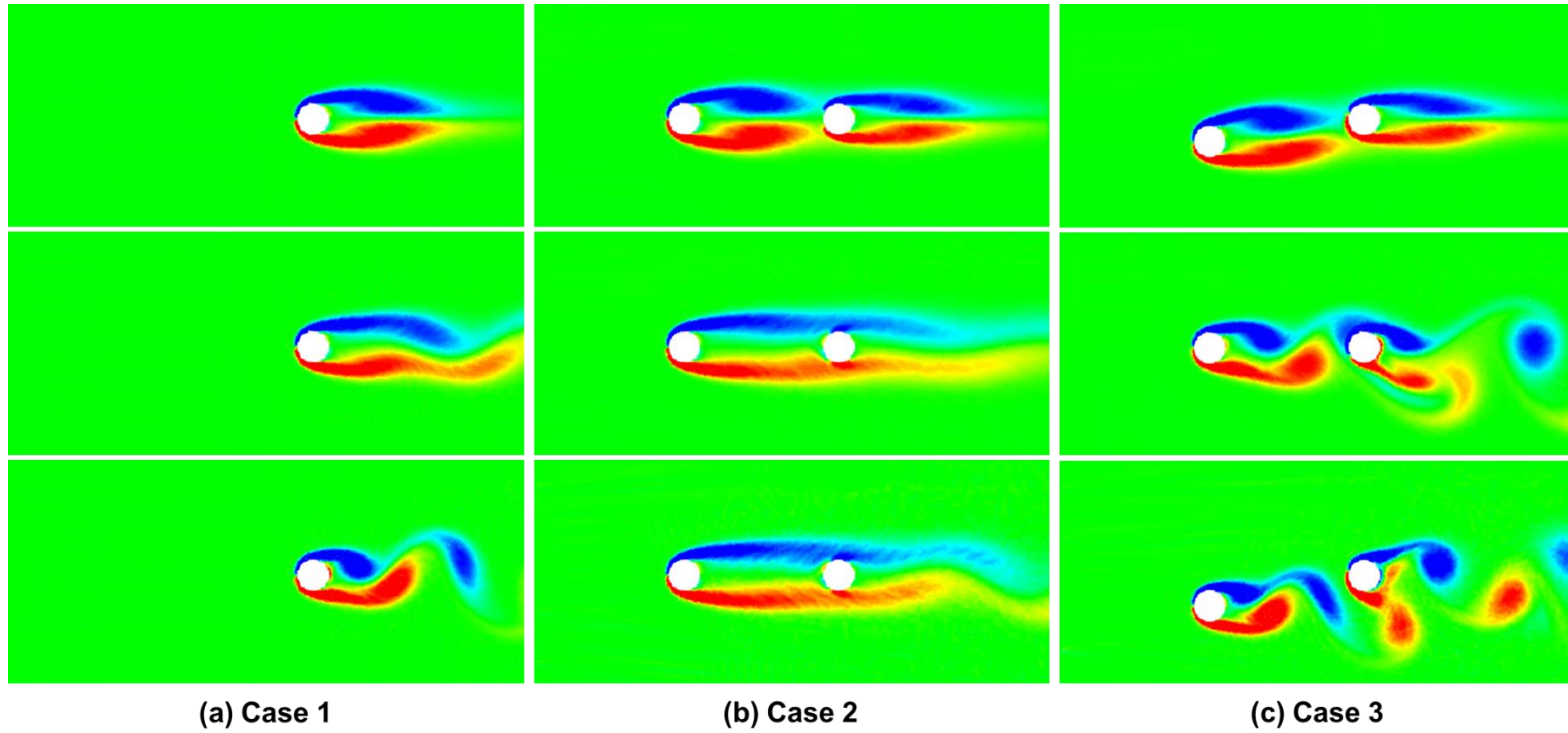


Figure 4.8 Vorticity for three cases: (a) case 1, (b) case 2, (c) case 3

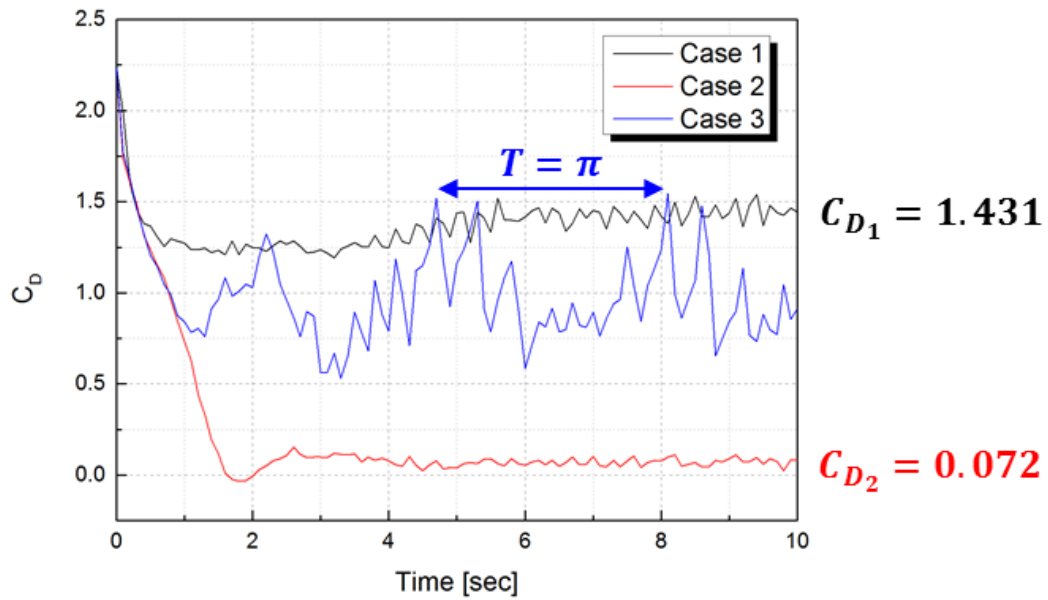


Figure 4.9 Drag coefficient for three cases with $Re = 100$

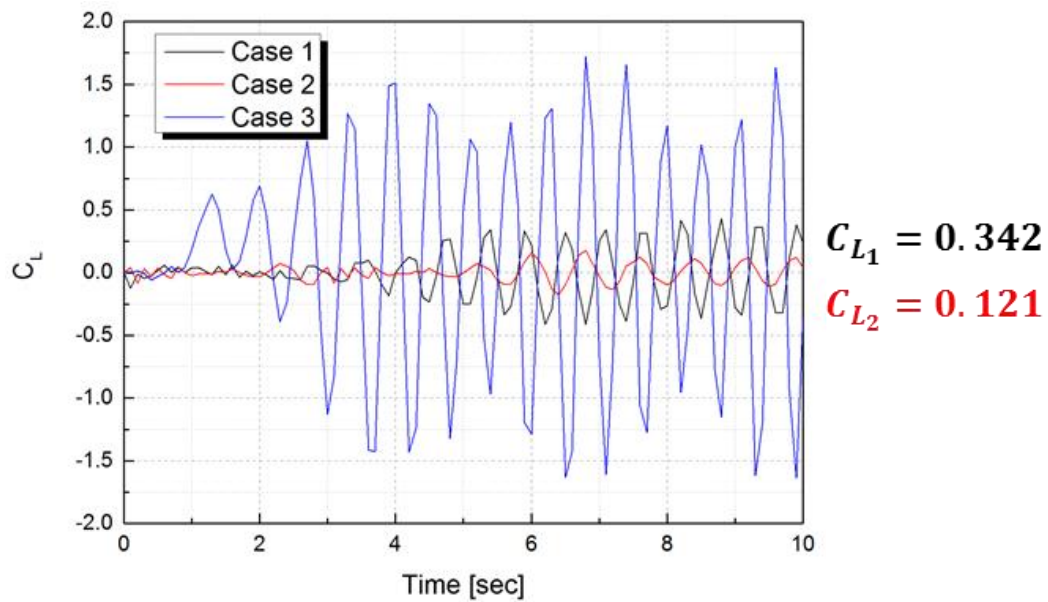


Figure 4.10 Lift coefficient for three cases with $Re = 100$

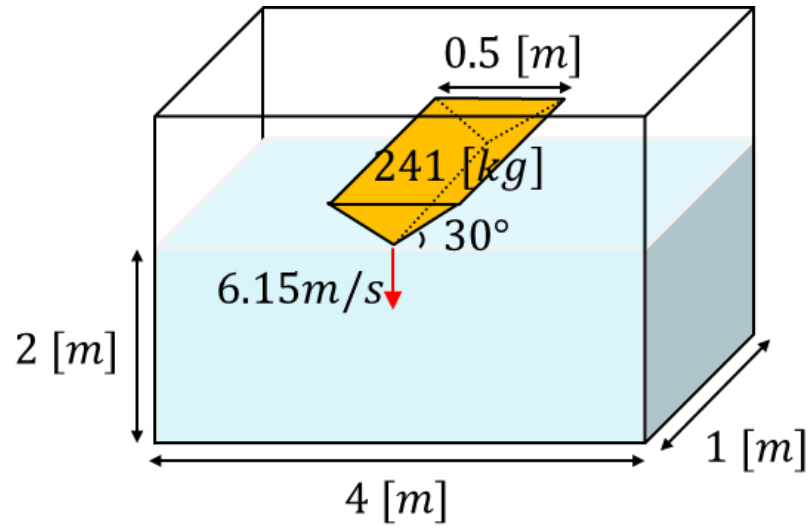


Figure 4.11 Schematic of wedge entry simulation

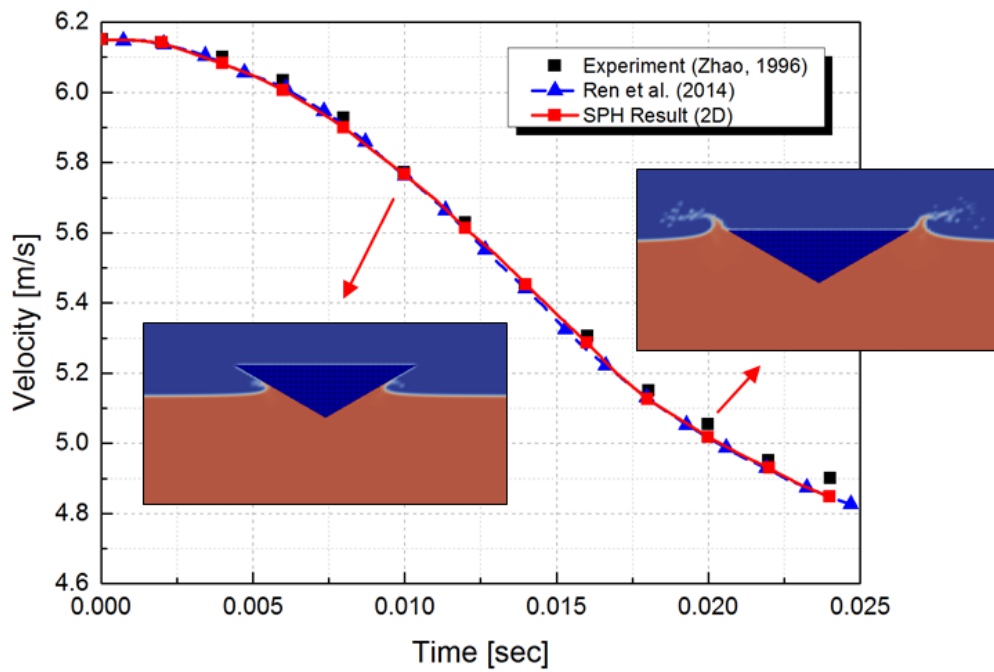
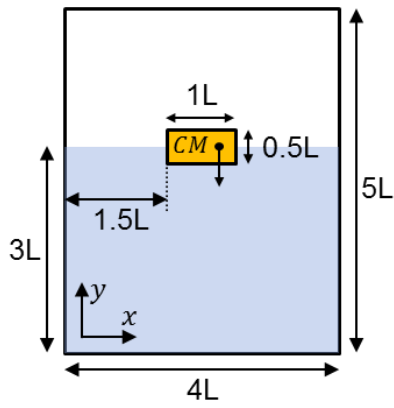


Figure 4.12 Comparison on the vertical velocity of the wedge



❖ Simulation Conditions

- $L = 1 [m]$
- $(x_{cm}, y_{cm}) = (0.25, 3.0)$
- $M = 1 [kg]$
- $I = 0.083 [kgm^2]$
- $\rho = 1 [kg/m^3]$
- $\nu = 0.002 [m^2/s]$
- $g = 1 [m/s^2]$

Figure 4.13 Geometry and conditions for simulation

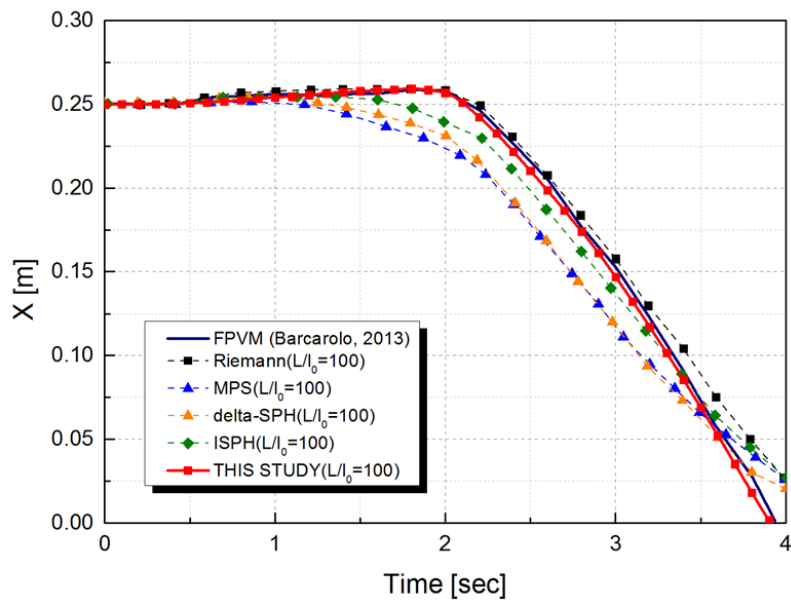


Figure 4.14 Comparison of the horizontal location of the solid

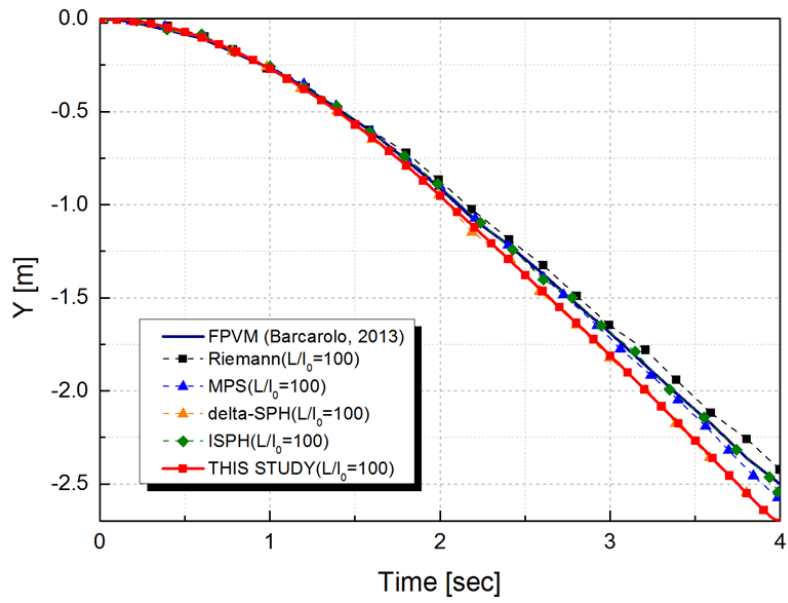


Figure 4.15 Comparison of the vertical location of the solid

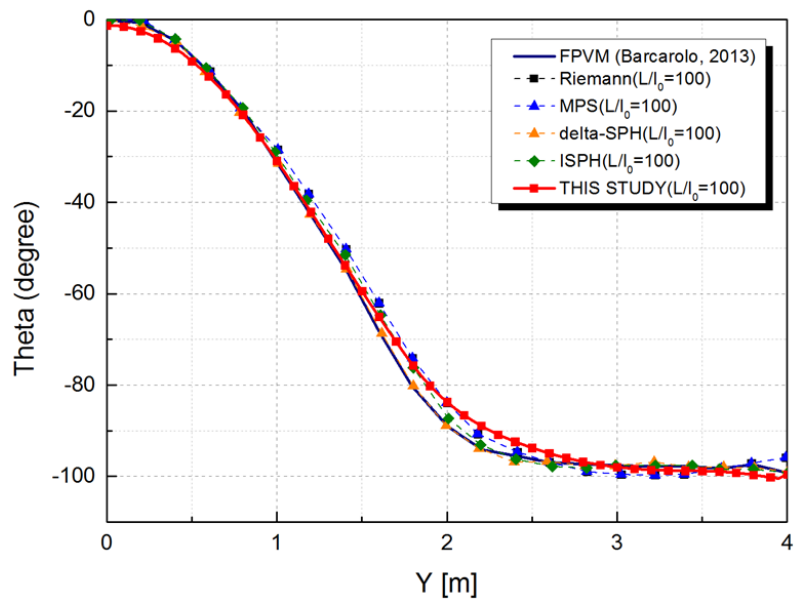


Figure 4.16 Comparison of the rotation angle of the solid

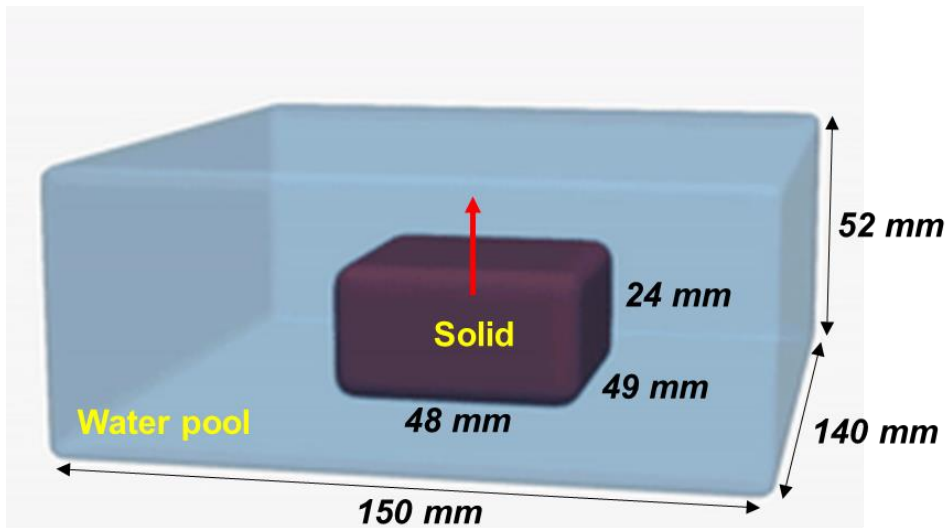


Figure 4.17 Snapshot of floating solid simulation

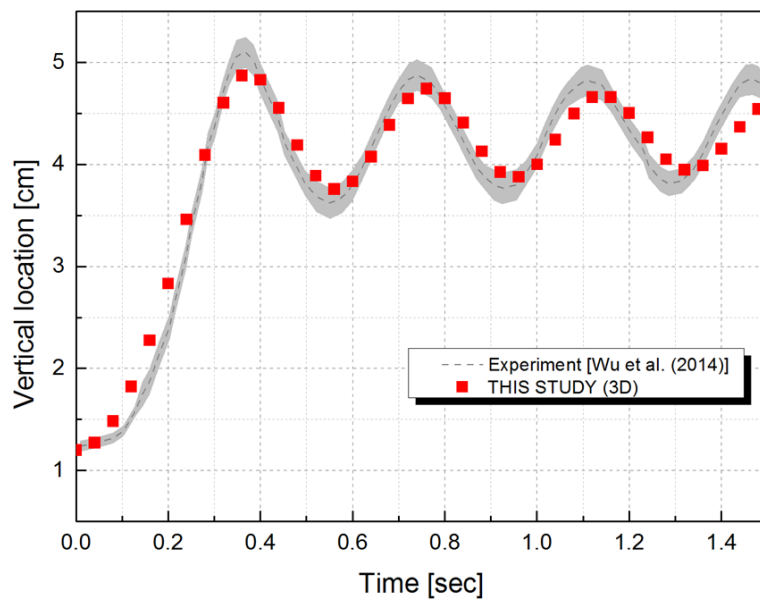


Figure 4.18 Simulation result with experimental data for floating solid

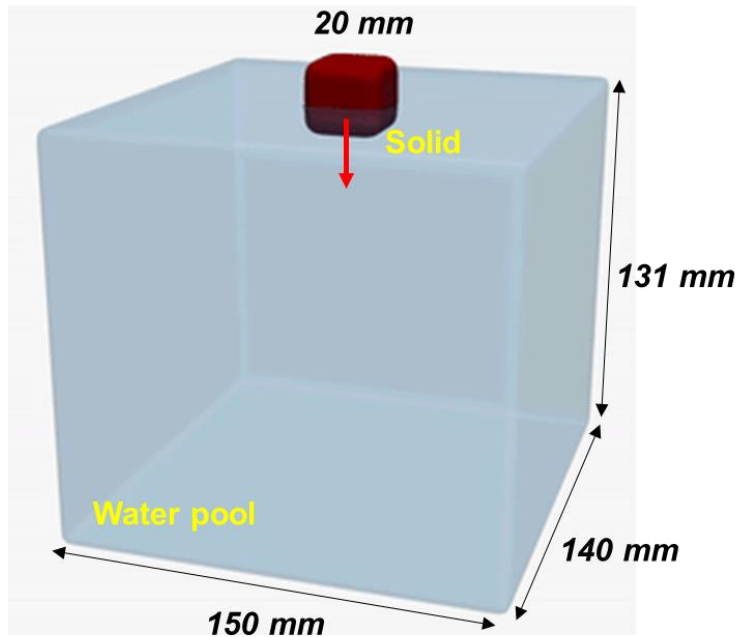


Figure 4.19 Snapshot of falling solid simulation

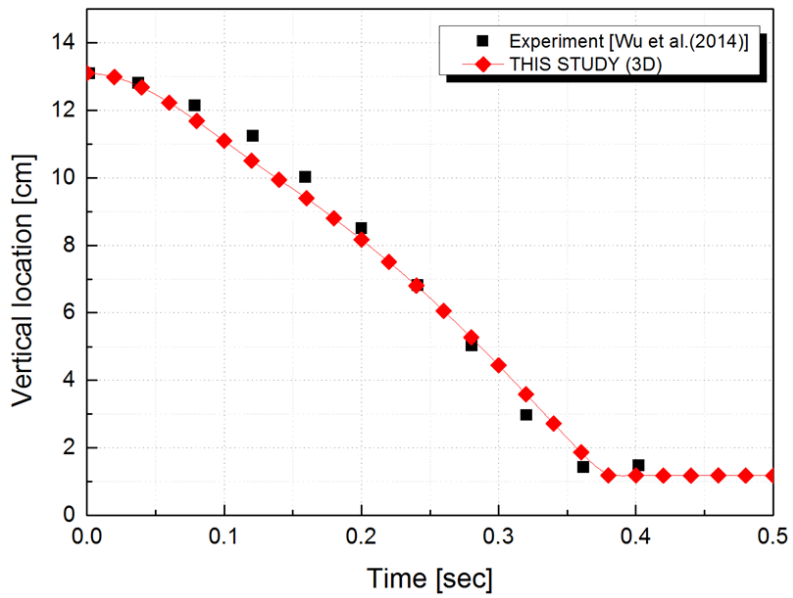


Figure 4.20 Simulation result with experimental data for falling solid

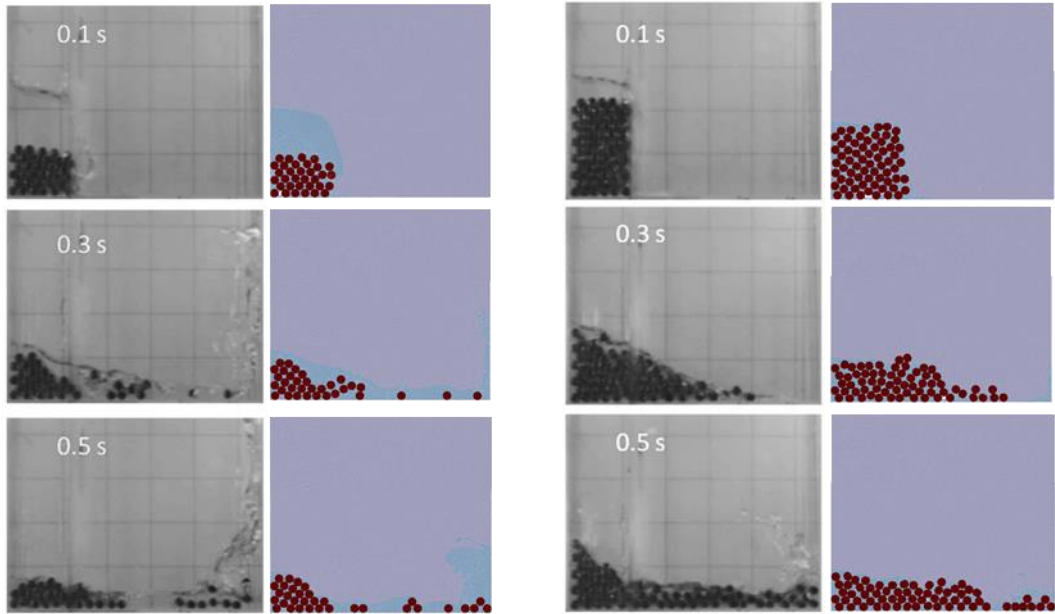


Figure 4.21 Snapshot of the multi-rigid behaviour: left (6layers), right (12layers)

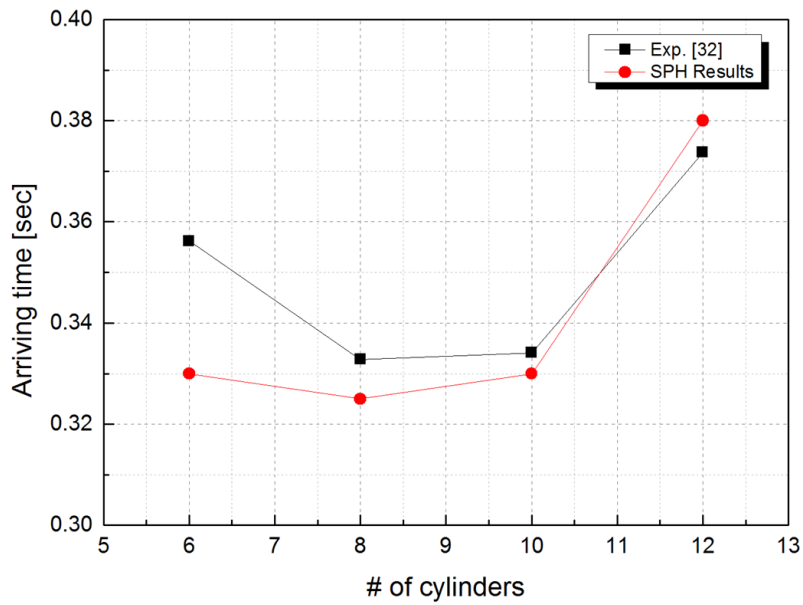


Figure 4.22 Comparison of arriving time with experiments

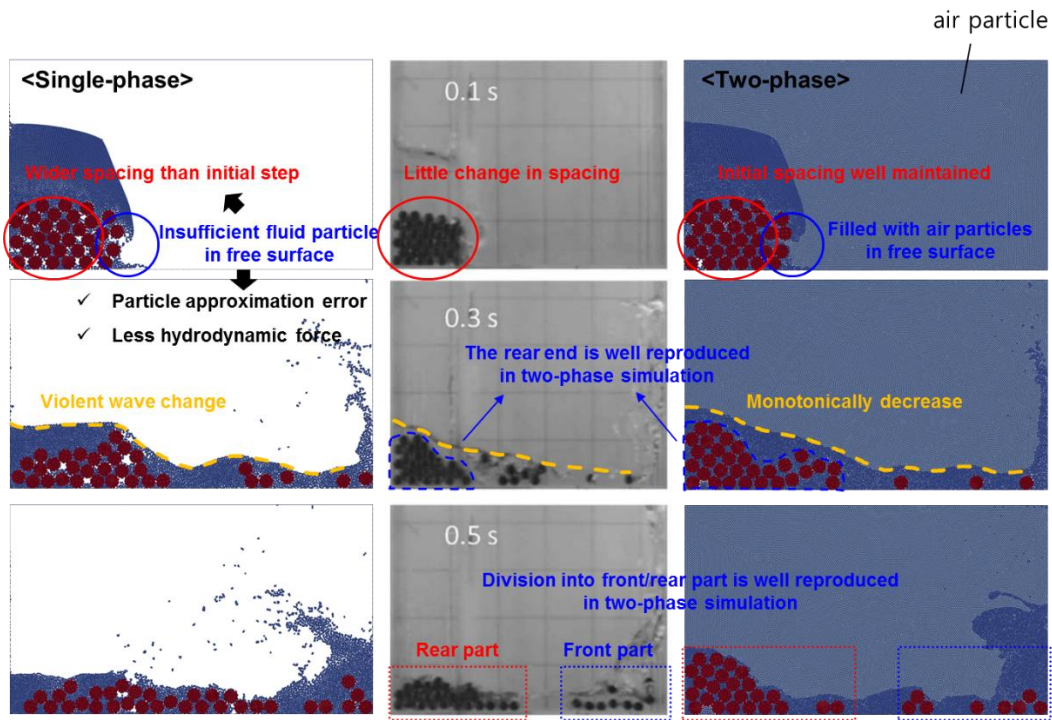


Figure 4.23 Comparison between single- and multi-phase simulations

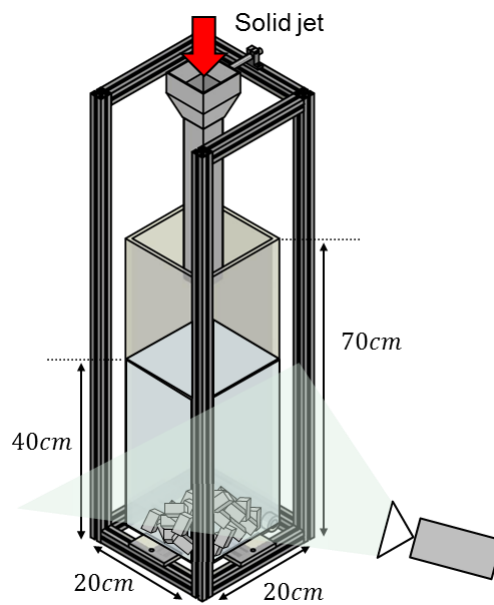


Figure 4.24 Schematic of sedimentation experiment apparatus

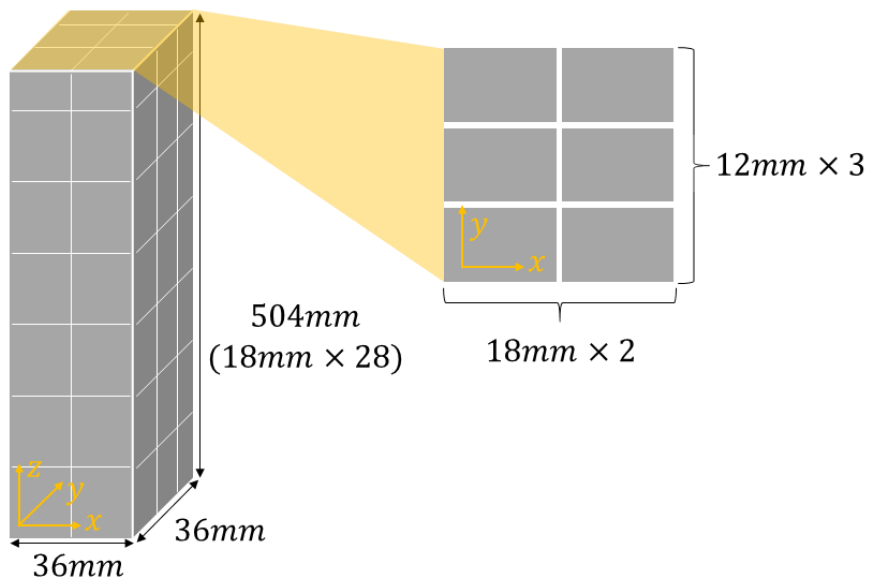


Figure 4.25 Stacked geometry of solid debris

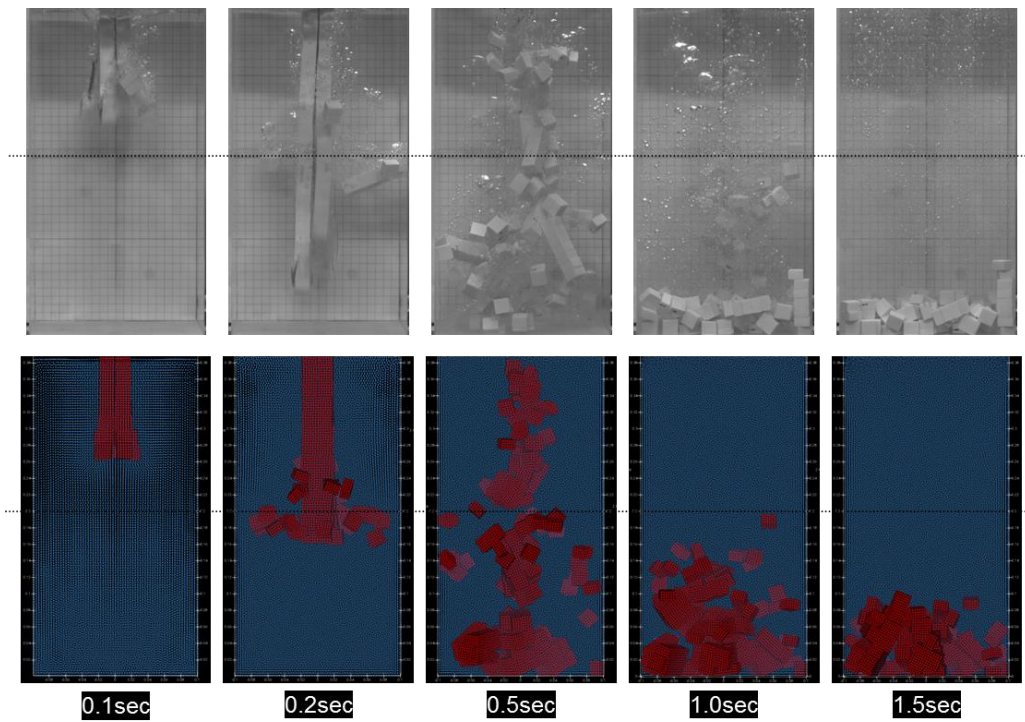


Figure 4.26 Comparison of non-spherical debris sedimentation

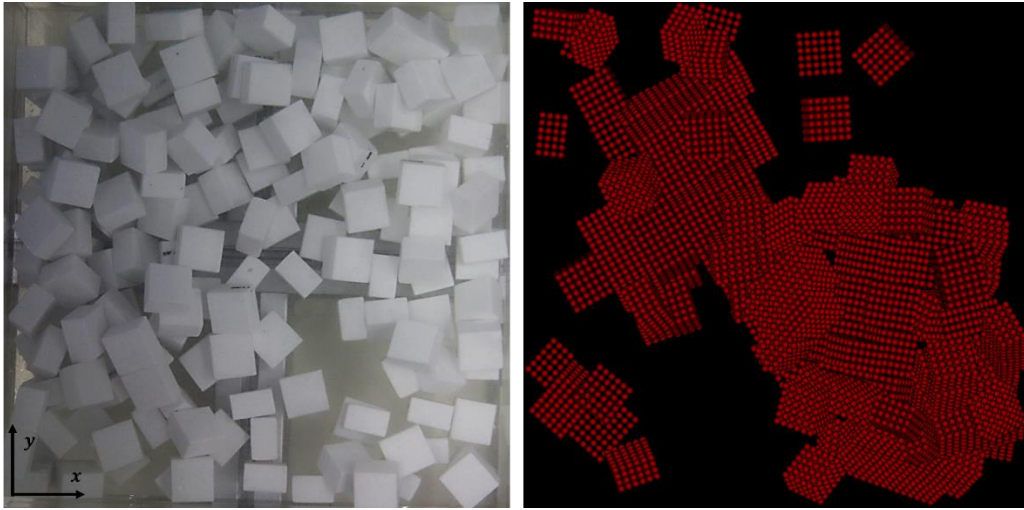


Figure 4.27 Snapshot of debris bed formation at the top view

Chapter 5

Conclusion

5.1 Summary

In this study, the fluid-solid analysis system with a non-spherical shape was developed using the SPH and RBD method to deal with the hydrodynamic issues in the nuclear field. For this main purpose, the achievements, results, and findings of detailed contents are as follows.

(i) **Development of Particle-based SPH Code**

For the incompressible multi-phase flow analysis, the Lagrangian-based SPH code (SOPHIA) has been developed. The basic conservation equations were implemented in the SOPHIA code, and multi-phase models such as normalized density model, improved surface tension model, and interface sharpness force model were also implemented. The various V&V cases like hydrodynamic interactions, heat transfer, and multi-phase simulations were carried out and showed good agreement with the experimental data and analytical solutions.

(ii) **Development of Non-spherical Solid Analysis System**

For the solid-phase analysis, the particle-based Rigid Body Dynamics (RBD)

has been implemented using the soft-sphere model which calculates the contact force based on particle overlap. Especially, the Hertz-Mindlin model which is most commonly used and verified in the DEM field is applied. The geometry of a rigid body can be easily expressed by a group of particles, and the behavior is simply analyzed through the collisions between rigid particles. The basic conservation quantities such as linear momentum, angular momentum, and kinetic energy due to the collision are well preserved in the simulations. Also, the implemented contact normal calculation method shows good results regardless of the type of collision. The various V&V simulations of single- and multi-rigid body collisions were carried out and showed good accordance with the experimental results and analytical solution.

(iii) Integration of SPH-RBD Model

In order to analyze the hydrodynamic interaction of the fluid and solid, the SPH method and RBD method are coupled using a fully resolved approach which doesn't require empirical correlations related to the solid shape. Also, the Neumann pressure boundary condition was implemented to estimate the accurate pressure of the solid body. The various V&V simulations including translational and rotational motion of the solid body by the fluids were conducted and showed good results with the experimental data.

(iv) GPU Parallelization of SPH-RBD Code

For computational efficiency, parallelization was carried out using Graphical Processing Unit (GPU). In the high-resolution simulations, the computational speed increases by up to 2 orders of magnitude compared to the CPU calculation. Also, in

order to calculate the properties of rigid particles constituting the rigid body efficiently and quickly, some GPU parallelization algorithms were implemented and showed good performance.

(v) **Code Application to Sedimentation of Non-spherical Solid Debris**

Using the GPU-parallelized SPH-RBD integrated code, the sedimentation simulations of non-spherical solid were conducted to confirm the applicability of the code developed in this study. Fragmentation and sedimentation of the non-spherical solid debris were well simulated, and it showed debris bed can be formed non-homogeneously, resulting in the possible internal flow path. Through the fluid-solid analysis system using the SPH-RBD method developed in this study, the applicability of non-spherical solid debris sedimentation was confirmed.

5.2 Recommendations

Through the present study, the following further studies are suggested.

- (i) In the present study, the same resolution of SPH particles and rigid particles is used. When there are a large amount of small solid bodies compared to the fluid domain, the analysis resolution is determined based on the small solids. This requires a lot of particles and can sometimes be insufficient. Therefore, it is recommended to analyze by applying multi-resolution to each fluid and solid particle.
- (ii) In this study, the sedimentation simulations were performed on the same

debris shape and size in order to confirm the applicability of the SPH-RBD code. Since the solid fragments of the molten core have different shapes and sizes with each other in the actual nuclear reactor accident, experimental or analytical data are needed for verification. As future work, it is recommended to obtain experimental data to analyze the different types of solid fragments.

- (iii) The simulations performed in this study are based on the laminar flow region. In a nuclear accident, it may be a turbulent region due to a large momentum of the jet, and this needs to be considered. Therefore, the consideration on the effects of turbulence in the vicinity of solid bodies is recommended.
- (iv) This study focuses on the hydrodynamic interaction of fluids and solids. However, various thermal behaviors such as solidification and boiling should be considered in actual reactor conditions. Therefore, the physical properties of the reactor materials should be implemented, and it is recommended to expand the scope for overall FCI process as shown in Figure 1.1.
- (v) Corium fragments can be electrically unstable, which can lead to electrical interactions between solid debris. If the size of the fragmented particles is quite small, the effect of the electrical interaction can be much larger than the mechanical interaction. Therefore, it is recommended to research on the electrical properties of corium debris.

Nomenclature

$f(r_i)$	Field function at the particle i
Ω	Support domain
W	Kernel function
h	Smoothing length [m]
h	Specific enthalpy [J/kg]
m	Mass [kg]
ρ	Density [kg/m^3]
\mathbf{r}_{ij}	Relative position vector between particle i and j
u	Velocity [m/s]
μ	Dynamic viscosity [$Pa \cdot s$]
g	Gravitational acceleration [m/s^2]
\dot{q}	Heat generation rate [$J/kg \cdot s$]
T	Temperature [K]
P	Pressure [Pa]
c_0	Speed of sound [m/s]
ρ_{ref}	Reference density [kg/m^3]
γ	EOS stiffness parameter
V	Volume [m^3]
k	Thermal conductivity [$W/m \cdot K$]
σ	Surface tension coefficient [N/m]
n	Surface normal vector
\hat{n}	Unit surface normal vector

c	Color field
Δt	Time-step [sec]
F_{ij}	Contact force between particle i and j [N]
e	Restitution coefficient
J	Impulse [$kg \cdot m/s$]
M	Total mass of the rigid body [kg]
I	Moment of inertia [$kg \cdot m^2$]
δ	Overlap between particles [m]
k_n	Spring stiffness coefficient
c_n	Damping coefficient
E^*	Equivalent Young's modulus [N/m^2]
E	Young's modulus [N/m^2]
G	Shear modulus [Pa]
G^*	Equivalent shear modulus [Pa]
R	Radius [m]
R^*	Equivalent radius [m]
M^*	Equivalent mass [kg]
u_0	Impact velocity [m/s]
w	Angular velocity [rad/s]
τ	Torque [$kg \cdot m^2/s^2$]
x, y, z	Cartesian coordinate [m]
L	Linear momentum [$kg \cdot m/s$]
E	Energy [J]
Δx	Initial particle distance [m]
θ	Degree [°]

ν	Kinetic viscosity [m^2/s]
C_D	Drag coefficient
C_L	Lift coefficient
F_D	Drag force [N]
F_L	Lift force [N]
St	Strouhal number
Re	Reynolds number

Superscripts

c	Corrector step
p	Predictor step
n	Normal direction
t	Tangential direction
r	Repulsive force
d	Damping force
c	Contact force
p	Pressure force

Subscripts

i	Center particle
j	Neighboring particles of particle i
f	Fluid phase
s	Solid phase

Bibliography

Adami, S., Hu, X. Y., & Adams, N. A. (2010). A new surface-tension formulation for multi-phase SPH using a reproducing divergence approximation. *Journal of Computational Physics*, 229(13), 5011-5021..

Adami, S., Hu, X. Y., & Adams, N. A. (2012). A generalized wall boundary condition for smoothed particle hydrodynamics. *Journal of Computational Physics*, 231(21), 7057-7075.

Amicarelli, A., Albano, R., Mirauda, D., Agate, G., Sole, A., & Guandalini, R. (2015). A Smoothed Particle Hydrodynamics model for 3D solid body transport in free surface flows. *Computers & fluids*, 116, 205-228.

Baraff, D. (1997). An introduction to physically based modeling: rigid body simulation I—unconstrained rigid body dynamics. SIGGRAPH course notes, 82.

Barcarolo, D. A. (2013). Improvement of the precision and the efficiency of the SPH method: theoretical and numerical study (Doctoral dissertation, Ecole Centrale de Nantes (ECN)).

Brookshaw, L. (1985). A method of calculating radiative heat diffusion in particle simulations. In *Proceedings of the Astronomical society of Australia* (Vol. 6, pp. 207-210).

Bui, H. H., Kodikara, J. A., Pathegama, R., Bouazza, A., & Haque, A. (2015). Large deformation and post-failure simulations of segmental retaining walls using mesh-free method (SPH). arXiv preprint arXiv:1501.04000.

Canelas, R. B., Crespo, A. J., Domínguez, J. M., Ferreira, R. M., & Gómez-Gesteira, M. (2016). SPH–DCDEM model for arbitrary geometries in free surface solid–fluid flows. *Computer Physics Communications*, 202, 131-140.

Cao, X. Y., Ming, F. R., Zhang, A. M., & Tao, L. (2018). Multi-phase SPH modelling of air effect on the dynamic flooding of a damaged cabin. *Computers & Fluids*, 163, 7-19.

Caserta, A. J., Navarro, H. A., & Cabezas-Gomez, L. (2016). Damping coefficient and contact duration relations for continuous nonlinear spring-dashpot contact model in DEM. *Powder Technology*, 302, 462-479.

Choi, H. Y., Chae, H., & Kim, E. S. (2021). Numerical simulation on jet breakup in the fuel-coolant interaction using Smoothed Particle Hydrodynamics. *Nuclear Engineering and Technology*.

Cundall, Peter A., and Otto DL Strack. "A discrete numerical model for granular assemblies." *geotechnique* 29.1 (1979): 47-65.

GIKEN, Structural Damage caused by earthquakes and Tsunamis, Disaster mitigation technologies with the implant method.

Gingold, R. A., & Monaghan, J. J. (1977). Smoothed particle hydrodynamics: theory and application to non-spherical stars. *Monthly notices of the royal astronomical society*, 181(3), 375-389.

Gissler, C., Peer, A., Band, S., Bender, J., & Teschner, M. (2019). Interlinked SPH pressure solvers for strong fluid-rigid coupling. *ACM Transactions on Graphics (TOG)*, 38(1), 1-13.

Gong, K., Shao, S., Liu, H., Wang, B., & Tan, S. K. (2016). Two-phase SPH simulation of fluid–structure interactions. *Journal of Fluids and Structures*, 65, 155-179.

Grenier, N., Antuono, M., Colagrossi, A., Le Touzé, D., & Alessandrini, B. (2009). An Hamiltonian interface SPH formulation for multi-fluid and free surface flows. *Journal of Computational Physics*, 228(22), 8380-8393.

Hashemi, M. R., Fatehi, R., & Manzari, M. T. (2012). A modified SPH method for simulating motion of rigid bodies in Newtonian fluid flows. *International Journal of Non-Linear Mechanics*, 47(6), 626-638.

Hu, G., Hu, Z., Jian, B., Liu, L., & Wan, H. (2010, August). On the determination of the damping coefficient of non-linear spring-dashpot system to model Hertz contact for simulation by discrete element method. In 2010 WASE International Conference on Information Engineering (Vol. 3, pp. 295-298). IEEE.

Hwang, B., Park, H. S., Jung, W. H., Lee, M., & Kim, M. H. (2019). Numerical validation and investigation for the sedimentation of solid particles in liquid pool using the CFD-DEM coupling algorithm. *Nuclear Engineering and Design*, 355, 110364.

Jin, Youngho, and Kwangil Ahn. "Improvement of Diagnostic Flow Chart in Severe Accident Management Guidance of OPR1000 Reflecting Fukushima Accident Experience." *Transactions of the Korean Nuclear Society Spring Meeting*. 2014.

Jo, Y. B., Park, S. H., Choi, H. Y., Jung, H. W., Kim, Y. J., & Kim, E. S. (2019). SOPHIA: Development of Lagrangian-based CFD code for nuclear thermal-hydraulics and safety applications. *Annals of Nuclear Energy*, 124, 132-149.

Johnson, K. L. "Contact Mechanics, Cambridge University Press, Cambridge, 1985."

Joubert, J. C., Wilke, D. N., Govender, N., Pizette, P., Tuzun, U., & Abriak, N. E. (2020). 3D gradient corrected SPH for fully resolved particle–fluid interactions. *Applied Mathematical Modelling*, 78, 816-840.

Junior, R. A. A., Cheng, L. Y., & Osello, P. H. S. (2019). An improvement of rigid bodies contact for particle-based non-smooth walls modeling. *Computational Particle Mechanics*, 6(4), 561-580.

Karbojian, A., Ma, W. M., Kudinov, P., & Dinh, T. N. (2009). A scoping study of debris bed formation in the DEFOR test facility. *Nuclear Engineering and Design*, 239(9), 1653-1659.

Lemieux, M., Léonard, G., Doucet, J., Leclaire, L. A., Viens, F., Chaouki, J., & Bertrand, F. (2008). Large-scale numerical investigation of solids mixing in a V-blender using the discrete element method. *Powder Technology*, 181(2), 205-216.

Li, Y., & Asai, M. (2018). Fluid-rigid body interaction simulation based on a stabilized ISPH method incorporated with the impulse-based rigid body dynamics. *Transactions of the Japan Society for Computational Engineering and Science*, 2018(2), 20182010.

Li, Y., Wang, Z., Lin, M., Zhong, M., Zhou, Y., & Yang, Y. (2017). Experimental studies on breakup and fragmentation behavior of molten tin and coolant interaction. *Science and Technology of Nuclear Installations*, 2017.

Liu, G. R., & Liu, M. B. (2003). *Smoothed particle hydrodynamics: a meshfree particle method*. World scientific.

Liu, Gui-Rong, and Moubin B. Liu. *Smoothed particle hydrodynamics: a meshfree particle method*. World scientific, 2003.

Mahdavi, A. (2018). Pseudo-fluid particles for fluid-rigid body coupling in SPH. *KSCE Journal of Civil Engineering*, 22(11), 4194-4204.

Mao, J., Zhao, L., Di, Y., Liu, X., & Xu, W. (2020). A resolved CFD–DEM approach for the simulation of landslides and impulse waves. *Computer Methods in Applied Mechanics and Engineering*, 359, 112750.

Marrone, S., Colagrossi, A., Antuono, M., Colicchio, G., & Graziani, G. (2013). An accurate SPH modeling of viscous flows around bodies at low and moderate Reynolds numbers. *Journal of Computational Physics*, 245, 456-475.

Mindlin, R. D., & Deresiewicz, H. E. R. B. E. R. T. (1953). Elastic spheres in contact under varying oblique forces.

Monaghan, J. J. (1994). Simulating free surface flows with SPH. *Journal of computational physics*, 110(2), 399-406.

Monaghan, J. J., & Kajtar, J. B. (2009). SPH particle boundary forces for arbitrary boundaries. *Computer physics communications*, 180(10), 1811-1820.

Monaghan, J. J., Kos, A., & Issa, N. (2003). Fluid motion generated by impact. *Journal of waterway, port, coastal, and ocean engineering*, 129(6), 250-259.

Monaghan, Joe J. "Simulating free surface flows with SPH." *Journal of computational physics* 110.2 (1994): 399- 406.

Monaghan, Joe J. "Smoothed particle hydrodynamics." *Reports on progress in physics* 68.8 (2005): 1703.

Oger, G., Doring, M., Alessandrini, B., & Ferrant, P. (2006). Two-dimensional SPH simulations of wedge water entries. *Journal of computational physics*, 213(2), 803-822.

Oh, S., Kim, Y., & Roh, B. S. (2009). Impulse-based rigid body interaction in SPH. *Computer Animation and Virtual Worlds*, 20(2-3), 215-224.

Panciroli, R., Abrate, S., Minak, G., & Zucchelli, A. (2012). Hydroelasticity in water-entry problems: Comparison between experimental and SPH results. *Composite Structures*, 94(2), 532-539.

Park, S. H., Jo, Y. B., Ahn, Y., Choi, H. Y., Choi, T. S., Park, S. S., ... & Kim, E. S. (2020). Development of multi-GPU-based smoothed particle hydrodynamics code for nuclear thermal hydraulics and safety: potential and challenges. *Frontiers in Energy Research*, 8, 86.

Park, S., & Jeun, G. (2011). Coupling of rigid body dynamics and moving particle semi-implicit method for simulating isothermal multi-phase fluid interactions. *Computer methods in applied mechanics and engineering*, 200(1-4), 130-140.

Peng, B. (2014). *Discrete element method (DEM) contact models applied to pavement simulation* (Doctoral dissertation, Virginia Tech).

Qiu, L. C., Liu, Y., & Han, Y. (2017). A 3D simulation of a moving solid in

viscous free-surface flows by coupling SPH and DEM. *Mathematical Problems in Engineering*, 2017.

Raji, A. O. (1999). *Discrete element modelling of the deformation of bulk agricultural particulates* (Doctoral dissertation, Newcastle University).

Ren, B., Jin, Z., Gao, R., Wang, Y. X., & Xu, Z. L. (2014). SPH-DEM modeling of the hydraulic stability of 2D blocks on a slope. *Journal of Waterway, Port, Coastal, and Ocean Engineering*, 140(6), 04014022.

Richards, J. R., Beris, A. N., & Lenhoff, A. M. (1995). Drop formation in liquid-liquid systems before and after jetting. *Physics of fluids*, 7(11), 2617-2630.

Schwaiger, H. F. (2008). An implicit corrected SPH formulation for thermal diffusion with linear free surface boundary conditions. *International journal for numerical methods in engineering*, 75(6), 647-671.

Solutions, D. E. M. (2014). *EDEM 2.6 theory reference guide*. *Edinburgh, United Kingdom*.

Sun, P., Ming, F., & Zhang, A. (2015). Numerical simulation of interactions between free surface and rigid body using a robust SPH method. *Ocean Engineering*, 98, 32-49.

Tang, Y., Jiang, Q., & Zhou, C. (2018). A Lagrangian-based SPH-DEM model

for fluid–solid interaction with free surface flow in two dimensions. *Applied Mathematical Modelling*, 62, 436-460.

Vetsch, D. F. (2012). Numerical simulation of sediment transport with meshfree methods (Doctoral dissertation, ETH Zurich).

Wang, J., & Chan, D. (2014). Frictional contact algorithms in SPH for the simulation of soil–structure interaction. *International Journal for Numerical and Analytical Methods in Geomechanics*, 38(7), 747-770.

Wang, X., Ban, X., Zhang, Y., & Liu, X. (2017). Rigid Body Sampling and Individual Time Stepping for Rigid-Fluid Coupling of Fluid Simulation. *Scientific Programming*, 2017.

Wang, Z., Hu, F., Duan, G., Shibata, K., & Koshizuka, S. (2019). Numerical modeling of floating bodies transport for flooding analysis in nuclear reactor building. *Nuclear Engineering and Design*, 341, 390-405.

Wu, T. R., Chu, C. R., Huang, C. J., Wang, C. Y., Chien, S. Y., & Chen, M. Z. (2014). A two-way coupled simulation of moving solids in free-surface flows. *Computers & Fluids*, 100, 347-355.

Xia, X., & Liang, Q. (2016). A GPU-accelerated smoothed particle hydrodynamics (SPH) model for the shallow water equations. *Environmental modelling & software*, 75, 28-43.

Young, A. S. (2012). Integrating two-way interaction between fluids and rigid bodies in the real-time particle systems library. The Florida State University.

Zhan, L., Peng, C., Zhang, B., & Wu, W. (2020). A SPH framework for dynamic interaction between soil and rigid body system with hybrid contact method. *International Journal for Numerical and Analytical Methods in Geomechanics*, 44(10), 1446-1471.

Zhang, A., Sun, P., & Ming, F. (2015). An SPH modeling of bubble rising and coalescing in three dimensions. *Computer Methods in Applied Mechanics and Engineering*, 294, 189-209.

Zhang, S., Kuwabara, S., Suzuki, T., Kawano, Y., Morita, K., & Fukuda, K. (2009). Simulation of solid–fluid mixture flow using moving particle methods. *Journal of Computational Physics*, 228(7), 2552-2565.

Zhao, D., & Liu, Y. (2016). Improved damping constant of Hertz-Damp model for pounding between structures. *Mathematical Problems in Engineering*, 2016.

Zhao, R., Faltinsen, O., & Aarsnes, J. (1996, June). Water entry of arbitrary two-dimensional sections with and without flow separation. In *Proceedings of the 21st symposium on naval hydrodynamics* (pp. 408-423).

Zhu, H. P., et al. "Discrete particle simulation of particulate systems: theoretical developments." *Chemical Engineering Science* 62.13 (2007): 3378-3396.

국문 초록

일본의 후쿠시마 사고 이후 원자로 중대 사고에 대한 연구의 필요성과 대처 능력 확보에 대한 중요성이 점점 증가하고 있다. 사고 시 발생할 수 있는 노심 용융물 거동에 대한 평가는 용융물-콘크리트 상호작용(MCCI, Molten Core Concrete Interaction)과 증기 폭발로부터의 원자로 노심 냉각성 및 건전성에 따른 재임계 측면에서 매우 중요하다. 특히 OPR 1000의 경우, 사전 충수 조건(Wet cavity condition)을 기본적인 원자로 외벽 냉각 대응 전략으로 채택함으로써 핵연료-냉각재 상호작용(FCI, Fuel Coolant Interaction) 반응이 필연적으로 발생하는 것으로 알려져 있다. [Jin, 2014] FCI 현상은 임의 형태의 핵연료 고체 파편물과 냉각재의 상호작용뿐만 아니라, 냉각재 비등 현상 등도 포함하는 다유체, 다상 현상으로 그 현상이 매우 복잡하다. 이 과정에서 원자로 건물 하부에 고체 파편물이 퇴적되어 잔해 층이 형성되고, 그 냉각성에 따라 사고의 다음 진행 상황에 영향을 줄 수 있다. 이러한 비구형 고체 파편물 거동에 대한 이해를 위해 강체 개념을 적용한 고체 해석 체계는 좋은 접근법이 될 수 있다. 따라서 본 연구에서는 유체와 고체 간 수력학적 상호작용 해석을 위해 입자유체동역학(SPH, Smoothed Particle Hydrodynamics) 기법과 강체역학(RBD, Rigid Body Dynamics) 기법을 연계하여 라그랑지안 해석 체계를 구축하였다.

완화입자유체동역학 기법은 해석 유체를 유한개의 입자로 표현함으로써 유동을 해석하는 라그랑지안 해석 기법 중 하나이다. 개별 입자들의 움직임으로 유동을 해석하므로 비선형의 대류항에 대한 계산이 필요 없으며, 입자가 추가되거나 사라지지 않는 한 해석 계의 전체 질량은 자동으로 보존된다. 이러한 라그랑지안 기법의 특성으로 SPH 방법은 자유 표면 유동, 다유체 유동, 다상 유동, 형태 변화가 큰 유동 등에 대해 해석 장점을 갖는다. 본 연구에서는 SPH 기법을 적용한 in-house SOPHIA 코드를 사용하여 비압축 다상 유동 해석을 수행하였으며, 벤치마크 데이터와의 비교에서 좋은 검증 해석 결과를 보였다.

강체역학은 외력에 의해 형태가 변하지 않는 강체의 개념을 이용하여 고체의 병진 운동과 회전 운동을 해석하는 연구 분야이다. 본 연구에서는 이산요소법 (DEM, Discrete Element Method) 분야에서 오랜 시간 동안 널리 사용되고 검증되었던 Hertz-Mindlin 충돌 모델을 적용하여 강체 간 충돌 해석을 구현하였다. 강체는 유한개의 입자들로 표현할 수 있으며, 강체 간 충돌은 각 강체를 구성하고 있는 입자쌍의 작은 중첩을 기반으로 계산된다. 본 연구에서는 입자기반의 강체역학 해석 코드를 이용하여 단일 강체 및 다중 강체 충돌에 대해 검증 해석을 수행하였으며, 해석해 및 벤치마크 데이터 결과와 잘 일치함을 확인하였다.

원자력 분야에서 발생할 수 있는 비구형 고체와 유체간 상호작용 해석을 위해 앞서 설명한 SPH 기법과 강제역학 연계 해석 코드를 개발하였다. 본 연구에서 적용한 완전 해상 방식(Fully resolved approach)은 유체-고체의 상이 분리되어 있고, 제 1 원리를 만족하므로 고체의 형상에 따른 상관식과 표면 적분이 필요하지 않다는 장점이 있다. 또한 고체 경계면에서의 정확한 압력 계산을 위해 유체 입자 정보를 기반으로 노이만 압력 경계 조건을 적용하였다. 본 연구에서는 이러한 해상 방식의 유체-강체 연계 해석 코드를 이용하여 비구형 고체와 유체의 수력학적 상호작용에 대한 검증 해석을 수행하였으며, 선행된 실험과의 비교에서 좋은 결과를 보였다.

유동 해석을 위해 본 연구에 적용한 SPH 방법에서는 수식들이 매우 선형적이고 외연적(Explicit)으로 계산을 수행하기 때문에 각 입자에 대한 계산이 독립적으로 수행되어도 문제가 없다. 따라서 SPH 방법은 계산 병렬화에 최적화된 방법으로 잘 알려져 있으며, 대규모 고해상도 해석을 위해 이는 필수적이다. 또한 입자 기반의 강체 계산을 위해서는 효율적인 계산 알고리즘이 필요하다. 따라서 본 연구에서는 대규모 계산과 높은 연산 효율성을 위해 그래픽처리장치(GPU, Graphic Processing Unit)를 이용하여 계산 병렬화를 수행하였으며, 이를 이용한 다중 고체와 유체의 상호작용 해석에서 좋은 계산 성능을 확인하였다.

본 연구에서 수행한 비구형 고체와 유체의 수력학적 상호작용을 위한 GPU 기반의 SPH 해석 코드 개발 연구를 통해 원자로 중대사고 시 발생할 수 있는 냉각재와 핵연료 고체 파편물의 수력학적 상호작용 뿐만 아니라, 고체 파편물 간 역학적 상호작용에 대해 효율적인 해석 체계를 개발하였다. 이를 통해 습식 공동(wet cavity)에서 발생하는 핵연료 고체 파편물의 퇴적 작용, 쓰나미 사고로 인한 해안 구조물의 수력학적 상호작용, 그리고 침수 사고 시 원자로 건물 내 부유물의 거동 등 원자력 분야에서 발생할 수 있는 다양한 고체-유체의 수력학적 상호작용에 대한 해석적 연구에 적용하고 기여할 수 있을 것으로 기대한다.

주요어

완화입자유체동역학, 강제 역학, 원자로 중대사고, GPU 코드 병렬화, 비구형 고체 파편물, 퇴적 작용

학 번: 2013-23187